AD_____

Award Number: DAMD17-01-1-0064

TITLE: Endourethral MRI guidance for Prostatic RF Ablation

PRINCIPAL INVESTIGATOR: Ergin Atalar, Ph.D.

CONTRACTING ORGANIZATION: Johns Hopkins University School of Medicine
Baltimore, MD 21205

REPORT DATE: June 2005

TYPE OF REPORT: Final

PREPARED FOR: U.S. Army Medical Research and Materiel Command
Fort Detrick, Maryland 21702-5012

DISTRIBUTION STATEMENT: Approved for Public Release;
Distribution Unlimited

REPORT DOCUMENTATION PAGE

Form Approved
OMB No. 0704-0188

1. REPORT DATE *(DD-MM-YYYY)*	2. REPORT TYPE	3. DATES COVERED *(From - To)*
01-06-2005	Final	1 Jun 2001 - 31 May 2005

4. TITLE AND SUBTITLE
Endourethral MRI guidance for Prostatic RF Ablation

5a. CONTRACT NUMBER

5b. GRANT NUMBER
DAMD17-01-1-0064

5c. PROGRAM ELEMENT NUMBER

6. AUTHOR(S)
Ergin Atalar, Ph.D.

E-Mail: eatalar@mri.jhu.edu

5d. PROJECT NUMBER

5e. TASK NUMBER

5f. WORK UNIT NUMBER

7. PERFORMING ORGANIZATION NAME(S) AND ADDRESS(ES)
Johns Hopkins University School of Medicine
Baltimore, MD 21205

8. PERFORMING ORGANIZATION REPORT NUMBER

9. SPONSORING / MONITORING AGENCY NAME(S) AND ADDRESS(ES)
U.S. Army Medical Research and Materiel Command
Fort Detrick, Maryland 21702-5012

10. SPONSOR/MONITOR'S ACRONYM(S)

11. SPONSOR/MONITOR'S REPORT NUMBER(S)

12. DISTRIBUTION / AVAILABILITY STATEMENT
Approved for Public Release; Distribution Unlimited

13. SUPPLEMENTARY NOTES

14. ABSTRACT

Prostate cancer constitutes a major health problem. Although the medical techniques currently in use to diagnose prostate cancer are successful, the methods to stage the cancer and visualize the invasion and spread of the cancer are inadequate. MRI is known to be the best method for staging but it does not offer image resolution that is acceptable, especially for detecting disease in the anterior prostate. In the first year of the project, we have developed a phased array coil setup that enabled us to image the prostate with a 160-micron image resolution. The second year, we developed a mechanical setup that enabled placement of the needles in the prostate with 1mm accuracy. Results from both of these endeavors have been published in high-impact journals. We have also developed methods for imaging temperature changes in the prostate with high accuracy. Most of the goals of this project have been achieved.

15. SUBJECT TERMS
MRI, RF ablation of prostate, MRI-guided interventions

16. SECURITY CLASSIFICATION OF:			17. LIMITATION OF ABSTRACT	18. NUMBER OF PAGES	19a. NAME OF RESPONSIBLE PERSON
a. REPORT	b. ABSTRACT	c. THIS PAGE			19b. TELEPHONE NUMBER *(include area code)*
U	U	U	UU	120	

Table of Contents

Cover.....1

SF 298.....2

Introduction.....4

Body.....4

Key Research Accomplishments.....5

Reportable Outcomes.....5

Conclusions.....7

References.....7

Appendices.....7

A. Introduction

Prostate cancer constitutes a major health problem. It is reported that 50% of men over age 80 have some form of prostate cancer, and in developed countries, 30% of men develop microscopic prostate cancer in their lifetime. Another 10% of men develop clinical prostate cancer and 3% of men die from the disease. Although the medical techniques currently in use to diagnose prostate cancer are successful, the methods to stage the cancer and visualize the invasion and spread of the cancer are inadequate. MRI is known to be the best method for staging but it does not offer image resolution that is acceptable, especially for detecting disease in the anterior prostate. In this study, we developed phased array coils to image the prostate at high resolution. In addition, we have developed a system that enables prostatic interventions in a conventional MRI scanner using these high-resolution images.

B. Body

B.1. *Coil Design.*

In this study, we designed a prostate phased array system that consisted of one 3-inch surface coil (General Electric), one endourethral coil, and two endorectal coils. Two types of endourethral coils were investigated: a loopless design that fit into a 2.5 mm diameter sheath; and a loop design that fit into a 5.3 mm diameter sheath. Two 1.3 x 2 cm rectal loop coils were mounted on the same probe, with the amount of overlap set so that interloop flux was minimized to ensure isolation. All coils were matched and decoupled by the appropriate circuitry. The safety analysis of this design has been completed and tested on animals.

B.2. *Accurate Needle Placement*

A micro coil tracking method has been developed to quickly (50 msec) and accurately (mean micro coil position error < 1 mm) locate the position and orientation of an intrarectal needle guide within the MR imaging volume. Via a mechanical positioning mechanism and extended control rods, the needle guide can be rotated and translated from outside of the closed scanner bore. Once the needle guide is positioned on the proper trajectory, the RF needle can be inserted to a controlled depth via an offset stop. The needle guide was situated inside a stationary rectal sheath that served to minimize prostate motion and also housed a local imaging coil.

We placed gold seeds in a dog prostate using this technique and measured the position of the seeds in order to test the accuracy of the needle positioning mechanism. We also injected blue dye and contrast agent mixture into the prostate to develop an accurate prostate treatment technique. This method of MR-guided injection of therapeutic agents has attracted much attention in the research community.

B.3. *MR guided Biopsy*

We modified the above-mentioned system to enable MR-guided biopsy. We have tested this system on the dog prostate. We later redesigned the system to make it suitable for use in the human prostate. We completed the safety testing. We established a collaboration with investigators at the NIH/NCI to test this design. Our collaborators have obtained IRB approval at NIH to test the design. With intramural NIH funding, they applied the design to patients with known prostate cancer.

C. Key Research Accomplishments

In the original application, we proposed to develop a system for animal use only. The rapid progress in the animal prototype development resulted from the collaboration formed with a group of researchers at NIH/NCI. We took the liberty to move to the next stage for the development of a human grade prostate intervention system. This system was used on patients at NIH using intramural NIH funds. It is important to note that US Army funds were not used for these patient studies, since the Army funds were to be used only for the development of "human grade" MR-guided prostate biopsy and needle placement devices. The RF ablation component of the project was not completed; however, we have produced 22 publications.

D. Reportable Outcomes

First Year

1. A. C. Yung, Y. A. Oner, J. M. Serfaty, M. Feleney, X. Yang, E. Atalar, Phased Array Coils for High Resolution Prostate MR Imaging, IEEE EMBS, Istanbul, Turkey, 2001.
2. A. .C Yung, A. Y. Oner, J. M. Serfaty, M. Feneley, X. Yang, E. Atalar, High Resolution Imaging of Canine Prostate using Endorectal/Endourethral Phased Array Coils, ISMRM, Book of abstracts Paper#1896, Honolulu, HI, 2002.

Second Year

3. R. C. Susil, A. Krieger, J. A. Derbyshire, L. L. Whitcomb, G. Fichtinger, E. Atalar, "MRI Guided Intraprostatic Therapeutic Injections in a Closed, 1.5T Scanner", ISMRM 2003.
4. R. C. Susil, K. Camphausen, E. Atalar, E. R. McVeigh, H. Ning, R. W. Miller, C. N. Coleman, C. Menard *"MRI Guidance and Planning for High-Dose-Rate Brachytherapy (HDRT) of the Prostate"* ISMRM 2003.
5. R.C. Susil, A. Krieger, J.A. Derbyshire, A. Tanacs, E.R. McVeigh, L.L. Whitcomb, G. Fichtinger, E. Atalar, *"A System for Guidance and Monitoring of Transrectal Prostate Biopsy in a 1.5 T Closed MR Scanner"*. iMRI Meeting, Leipzig, Germany, published in Eur. Radiology vol: 12, page F3, 2002.
6. V. C. Shah, A. El-Sharkawy, X. Du, X. Yang, E. Atalar, "MR signal for one pixel Temperature in °C SSFP based MR Thermometry", ISMRM 2003.
7. **Susil RC, Krieger A, Derbyshire JA, Tanacs A, Whitcomb LL, Fichtinger G, Atalar E. System for MR image-guided prostate interventions: canine study. Radiology 2003;228(3):886-894.**
8. **Yung, Y. Oner, J. M. Serfaty, M. Feleney, X. Yang, E. Atalar, Phased array MRI of canine prostate using endorectal and endourethral coils, Magnetic Resonance in Medicine, 49(4) 710-715, 2003.**

Third Year

9. R. C. Susil, C. Ménard, A. Krieger, J. A. Coleman, K. Camphausen, P. Choyke, K. Ullman, S. Smith, G. Fichtinger, L. L. Whitcomb, C. N. Coleman, E. Atalar, Transrectal Prostate Biopsy and Fiducial Marker Placement in a Standard 1.5T MRI Scanner, ISMRM 2004 Osaka, Japan.
10. R. C. Susil, S. L. Chowning, A. Krieger, G. Fichtinger, L. L. Whitcomb, E. Atalar, MRI Guidance and Monitoring of Injected Therapeutic Agents, ISMRM 2004 Osaka, Japan.
11. A. Krieger, R. C. Susil, C. Ménard, J. A. Coleman, G. Fichtinger, L. L. Whitcomb, E. Atalar A Novel MRI Compatible Manipulator for Prostate Interventions, ISMRM 2004, Clinical Focus Session: Cancer Diagnosis and Brachytherapy, Osaka, Japan.

12. Susil, R.C., Camphausen, K., Choyke, P., Gustafson, G., Miller, R.W., Ning, H., Ullman, K., Crouse, N., Atalar, E., Coleman, C. N., Menard, C. "A System For Transperineal Prostate Biopsy And Hdr Brachytherapy Under 1.5 T MRI Guidance: Techniques And Clinical Experience" RSNA 03.
13. Susil RC, Coleman JA, Krieger A, Camphausen K, Coleman CN, Linehan WM, Fichtinger G, Whitcomb LL, Atalar E, Menard C, Technique and accuracy of a clinical system for transrectal intraprostatic needle placement in a standard 1.5T MRI scanner, Journal of Urology 171 (4): 473-474 Suppl. S, April 2004.
14. Coleman JA, Susil RC, Krieger A, Choyke PL, Wise B, Thomasson D, Gharib A, Whitcomb LL, Fitchtinger G, Linehan WM, Coleman CN, Camphausen K, Atalar E, Menard C, MRI guided prostate biopsy with biological image acquisition and targeting in a standard 1.5T scanner, Journal of Urology 171 (4): 223-223 Suppl. S, April 2004.

Forth Year (No-cost extension)

15. **Susil RC, Camphausen K, Choyke P, McVeigh ER, Gustafson GS, Ning H, Miller RW, Atalar E, Coleman CN, Menard C, A System for Prostate Brachytherapy and Biopsy in a Standard 1.5 T MRI Scanner, Magnetic Resonance in Medicine, 52:683-687, 2004.**
16. **Krieger A, Susil RC, Menard C, Coleman JA, Fichtinger G, Atalar E, Whitcomb LL. Design of A Novel MRI Compatible Manipulator for Image Guided Prostate Intervention, IEEE Trans. BME, 52(2) 306-313 2004.**
17. **Susil RC, Menard C, Krieger A, Coleman JA, Camphausen K, Choyke P, Fichtinger G, Whitcomb LL, Coleman CN, Atalar E, Transrectal Prosotate Biopsy and Fiducial Marker Placement in a Standard 1.5T MRI Scanner, Urology Submitted 2004.**
18. **Ménard, C., Susil, R.C., Choyke, P., Coleman, J., Grubb, R., Gharib, A., Krieger, A., Guion, P., Thomasson, D., Ullman, K., Gupta, S., Espina, V., Liotta, L., Petricoin, E., Whitcomb, L.L., Fitchtinger, G., Atalar, E., Coleman, N.C., Camphausen, K. An Interventional MRI Technique for the Molecular Characterization of Intra-Prostatic Dynamic Contrast Enhancement In Press, Molecular Imaging Vol. 4, No:1, 2005 (Cover).**
19. **Scott L. Chowning, Robert C. Susil, Axel Krieger, Gabor Fichtinger, Louis L. Whitcomb, Ergin Atalar,A Preliminary Analysis and Model of Prostate Injection Distributions, Accepted to The Prostate, 2005.**
20. A. El-Sharkawy, P. Sotiriadis, B. Qui, and E. Atalar, Absolute Thermal Mapping Using the MR Scanner, ISMRM 2005, Miami, FL.
21. C. Menard, R. C. Susil, J. Coleman, R. Grubb, P. Choyke, P. Guion, A. Krieger, C. Coleman, E. Atalar, K. Camphausen, Integrating Diagnotic And Interventional MRI For The Molecular Characterization Of Prostate Cancer, ASCO 2005, Orlando, Florida.
22. R. I. Grubb, R. Susil, A. Krieger, P. Guion, G. Metzger, K. Ullman, S. Smith, K. Camphausen, A. Singh, W. M. Linehen, C. N. Coleman, E. Atalar, P. Choyke, C. Menard, J. A. Coleman, Biological MRI-guided Transrectal Prostate Biopsy, American Urological Association May 2005, San Antonio, Texas.

E. Conclusions

We completed Aim 1 and most of Aim 2 of the study. We have published twenty-two publications, seven of which are peer reviewed journal articles.

F. References

None

G. Appendices

1. Susil RC, Krieger A, Derbyshire JA, Tanacs A, Whitcomb LL, Fichtinger G, Atalar E. System for MR image-guided prostate interventions: canine study. Radiology 2003;228(3):886-894.
2. Yung, Y. Oner, J. M. Serfaty, M. Feleney, X. Yang, E. Atalar, Phased array MRI of canine prostate using endorectal and endourethral coils, Magnetic Resonance in Medicine, 49(4) 710-715, 2003.
3. Susil RC, Camphausen K, Choyke P, McVeigh ER, Gustafson GS, Ning H, Miller RW, Atalar E, Coleman CN, Menard C, A System for Prostate Brachytherapy and Biopsy in a Standard 1.5 T MRI Scanner, Magnetic Resonance in Medicine, 52:683-687, 2004.
4. Krieger A, Susil RC, Menard C, Coleman JA, Fichtinger G, Atalar E, Whitcomb LL. Design of A Novel MRI Compatible Manipulator for Image Guided Prostate Intervention, IEEE Trans. BME, 52(2) 306-313 2004.
5. Susil RC, Menard C, Krieger A, Coleman JA, Camphausen K, Choyke P, Fichtinger G, Whitcomb LL, Coleman CN, Atalar E, Transrectal Prosotate Biopsy and Fiducial Marker Placement in a Standard 1.5T MRI Scanner, Urology Submitted 2004.
6. Ménard, C., Susil, R.C., Choyke, P., Coleman, J., Grubb, R., Gharib, A., Krieger, A., Guion, P., Thomasson, D., Ullman, K., Gupta, S., Espina, V., Liotta, L., Petricoin, E., Whitcomb, L.L., Fitchtinger, G., Atalar, E., Coleman, N.C., Camphausen, K. An Interventional MRI Technique for the Molecular Characterization of Intra-Prostatic Dynamic Contrast Enhancement In Press, Molecular Imaging Vol. 4, No:1, 2005 (Cover).
7. Scott L. Chowning, Robert C. Susil, Axel Krieger, Gabor Fichtinger, Louis L. Whitcomb, Ergin Atalar,A Preliminary Analysis and Model of Prostate Injection Distributions, Accepted to The Prostate, 2005.

Radiology

Robert C. Susil, BS
Axel Krieger, MS
J. Andrew Derbyshire, PhD
Attila Tanacs, BS
Louis L. Whitcomb, PhD
Gabor Fichtinger, PhD
Ergin Atalar, PhD

Index terms:
Magnetic resonance (MR), experimental studies, 844.121411, 844.121412, 844.121416, 844.12143, 844.12149
Magnetic resonance (MR), guidance, 844.121411, 844.121412, 844.121416, 844.12143, 844.12149
Prostate neoplasms
Prostate neoplasms, MR, 844.121411, 844.121412, 844.121416, 844.12143, 844.12149
Prostate neoplasms, therapeutic radiology, 844.12149

Published online
10.1148/radiol.2283020911
Radiology 2003; 228:886–894

Abbreviations:
GRE = gradient echo
SE = spin echo

[1] From the Departments of Biomedical Engineering (R.C.S., E.A.), Mechanical Engineering (A.K., L.L.W.), Computer Science (A.T., G.F.), and Radiology (E.A.), Johns Hopkins University School of Medicine, 720 Rutland Ave, Traylor Bldg 330, Baltimore, MD 21205; Laboratory of Cardiac Energetics, National Institutes of Health, Bethesda, Md (J.A.D.); and Department of Electrical Engineering, Bilkent University, Ankara, Turkey (E.A.). Received July 31, 2002; revision requested September 30; revision received October 28; accepted December 10. Supported in part by NIH grants R01 HL57483 and R01 HL61672. Additional support from NSF grant ERC 9731478 and U.S. Army grant PC 10029. R.C.S. supported by an NIH training grant. **Address correspondence to** E.A. (e-mail: *eatalar@mri.jhu.edu*).

Author contributions:
Guarantors of integrity of entire study, R.C.S., A.K., G.F., E.A.; study concepts, R.C.S., A.K., L.L.W., G.F., E.A.; study design, all authors; literature research, R.C.S.; experimental studies, R.C.S., A.K., A.T., G.F., E.A.; data acquisition, R.C.S., A.K., A.T., G.F., E.A.; data analysis/interpretation, R.C.S., A.K.; manuscript preparation, R.C.S.; manuscript definition of intellectual content, R.C.S., A.K., L.L.W., G.F., E.A.; manuscript editing, R.C.S.; manuscript revision/review, R.C.S., J.A.D., G.F., E.A.; manuscript final version approval, all authors

System for MR Image–guided Prostate Interventions: Canine Study[1]

The purpose of this study was to demonstrate the use of a transrectal system that enables precise magnetic resonance (MR) image guidance and monitoring of prostate interventions. The system used a closed-bore 1.5-T MR imaging unit and enables one to take advantage of the higher signal-to-noise ratio achieved with traditional magnet designs, which is crucial for accurate targeting and monitoring of prostate interventions. In the first of the four canine studies, reliable needle placement, with all needles placed within 2 mm of the desired target site, was achieved. In two other studies, MR imaging was used to monitor distribution of injected contrast agent solution (gadopentetate dimeglumine mixed with trypan blue dye) in and around the prostate, thereby confirming that solution had been delivered to the desired tissue and also detecting faulty injections. In the final study, accurate placement and MR imaging of brachytherapy seeds in the prostate were demonstrated. The described system provides a flexible platform for a variety of minimally invasive MR image–guided therapeutic and diagnostic prostate interventions.

Prostate carcinoma is the most commonly diagnosed life-threatening cancer in men in the United States. In 2002, the estimated incidence of this disease in male patients in the United States was 189,000 (1). As the incidence of prostate cancer is known to increase with age, this cancer will become more common as the U.S. population ages (2). Moreover, due to the widespread acceptance of prostate-specific antigen screening, routine rectal examination, and transrectal ultrasonographic (US) image–guided prostate biopsy, there has been a great increase in the early detection of prostate cancer (3).

Despite this early detection, the appropriate clinical management of prostate cancer is a very controversial subject. There is serious debate regarding the clinical relevance of low-grade prostate cancer. In some cases, prostate cancers grow very slowly and never become clinically important, whereas in other cases, these cancers are very aggressive and dangerous. Because foci of prostate cancer have been incidentally discovered at autopsy in more than 30% of men older than 50 years, it is clear that aggressive treatment is not always appropriate for this malignancy (4,5). Nevertheless, reports (6–8) have shown that overly conservative management (ie, "watchful waiting") can result in poor patient outcomes. Clinical decision making is further complicated by the fact that most prostate cancers are assessed at diagnosis as "intermediate stage" and therefore carry an uncertain prognosis (9).

Currently, the two most accepted methods for treatment of localized prostate cancer are radical prostatectomy and radiation therapy (10). Although both of these approaches are associated with a good chance of a cure, they are also associated with a substantial risk of morbidity, including incontinence, rectal toxicity, and erectile dysfunction (11). Owing to these conflicting factors, there have been increased efforts to develop focal minimally invasive treatment modalities that can be used to target cancerous tissue while reducing morbidity and treatment duration (12).

Effective image guidance of these minimally invasive therapies requires *(a)* excellent visualization of the prostate and the surrounding anatomy so that cancerous tissue can be treated while nearby neural and vascular structures are avoided and *(b)* visualization of the therapeutic agent itself for direct confirmation that the desired abnormal tissue has been treated. On

the basis of these conditions, magnetic resonance (MR) imaging is the best modality for image guidance because it yields excellent soft-tissue contrast, has multiplanar capabilities, and has the potential to yield spectral and biologic information (13). MR imaging has been shown to enable far better visualization of the prostate and surrounding structures than either US or computed tomography (14). Moreover, with MR imaging it is possible to visualize injected liquid agents (15,16), solid implanted therapeutic seeds (eg, brachytherapy seeds) (14,17), and thermal therapy (by means of both direct temperature monitoring and imaging of tissue damage) (18,19). We emphasize that the ability to visualize the therapeutic agent is very enabling in that it allows direct positive confirmation of treatment delivery.

The purpose of our study was to demonstrate the use of a transrectal system that enables precise guidance and monitoring of prostate interventions with a 1.5-T MR imaging unit.

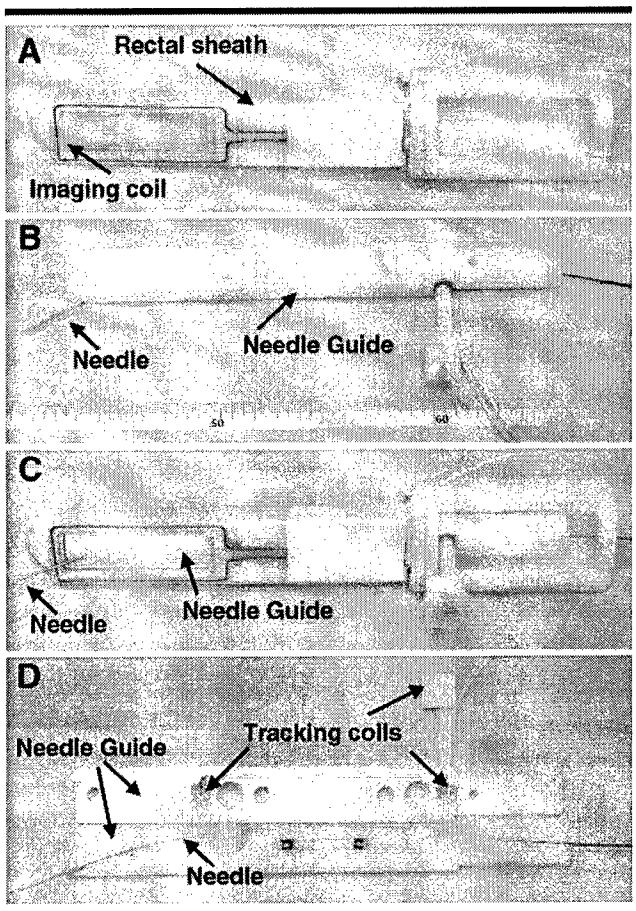

Figure 1. Rectal sheath and needle guide. *A,* A stationary rectal sheath with a radius of 1.5 cm forms a stable access route through which the prostate can be reached. A single-turn rectal imaging coil with tuning, matching, and decoupling elements is included in the sheath. A cylindrical needle guide *(B)* is placed inside the stationary rectal sheath *(C),* allowing rotational and translational degrees of freedom. *D,* The needle guide includes three tracking microcoils and a curved needle channel, which allows access to the prostate laterally through the rectal wall.

Materials and Methods

A mechanically actuated transrectal needle guide is used to perform MR image–guided needle placement in the prostate. With a microcoil tracking method, we are able to quickly (60 msec) and accurately locate the position and orientation of the needle guide in the MR imaging volume. Knowing the position of the needle enables acquisition of real-time MR images of an anatomic plane containing the needle path and determination of the needle position relative to previously acquired high-spatial-resolution images of the prostate.

Device Design

A thin-walled plastic cylindrical sheath (Delrin plastic; Du Pont, Wilmington, Del) with a radius of 1.5 cm is inserted into the rectum to create a stable and stationary entry point through which the prostate can be accessed (Fig 1, *A*). Integral to the sheath is a 2.5-cm-diameter single-turn coil for local imaging of the prostate. A window within the imaging coil in the sheath allows the needle to be advanced from inside the sheath, through the rectal wall, and into the body of the prostate.

Next, a cylindrical needle guide (Fig 1, *B*), which also is made of Delrin plastic, is placed in the rectal sheath (Fig 1, *C*). The needle guide is coaxial to the rectal sheath and thus is free to rotate and translate within the cavity formed by the sheath without causing deformation of the surrounding soft tissue. Integral to the needle guide are three fiducial microcoils and a curved channel for the needle (Fig 1, *D*). Because the needle channel is curved, the needle can be inserted along the axis of the needle guide and emerge from its lateral wall to allow access to the prostate through the window in the stationary rectal sheath.

Next, both the rectal sheath and the needle guide are affixed to a positioning stage made of nylon and Delrin plastic (Quality Transmission Components, New Hyde Park, NY) (Fig 2, *A*). This positioning stage serves to hold the rectal sheath stationary in the rectum. A linear track (ie, aluminum rail; 80/20, Columbia City, Ind) and a polyamide plastic articulated arm with six joints allow full mobility of the positioning stage so that it can be easily docked with the rectal sheath (Fig 2, *B*). After the stage is docked with the sheath, the linear track and articulated arm are locked down to prevent subsequent motion.

In addition to holding the rectal sheath stationary, the positioning stage contains a screw-drive mechanism that allows both rotation and translation of the needle guide. This device converts the rotation of two concentric control rods (Epoxy Tubing; TAP Plastics, Dublin, Calif), both of which extend outside the magnet bore, into rotation and translation of the needle guide; this process allows the operator to position the needle guide while the subject is in the closed MR magnet bore (Fig 2, *C*).

The entire device was constructed with a coaxial design, so the central axis represents an unobstructed path for insertion of the needle. The depth of needle insertion is controlled by using a variable

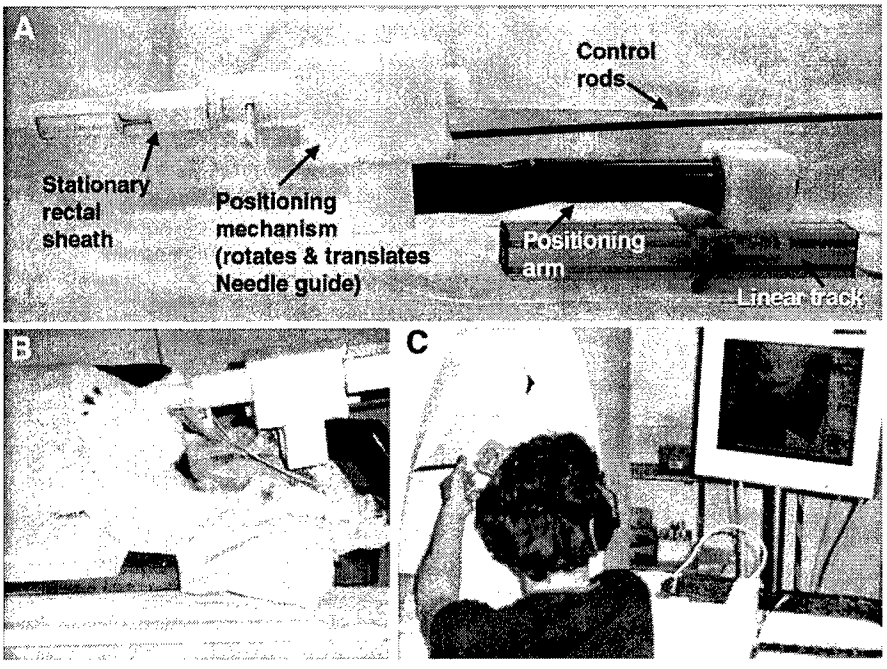

Figure 2. Assembled interventional device. *A,* The stationary rectal sheath and needle guide are affixed to the positioning stage. With use of a flexible articulated arm and a linear track, the device can be positioned freely until both the arm and the track are locked into position. The positioning mechanism converts rotation of the two concentric control rods into rotation and translation of the needle guide within the stationary rectal sheath. *B,* The sheath is positioned inside the rectum and held stationary by the positioning arm and linear track. *C,* By rotating the two control rods located outside the bore, the needle guide can be positioned within the rectum.

offset stop that is inserted at the back of the device before the needle is introduced. An 18-gauge coaxial needle (MRI Devices Daum, Schwerin, Germany) is inserted so that the needle tip will emerge from the side of the needle guide.

Device Tracking, Prostate Targeting, and Real-Time Imaging

The MR pulse sequences and hardware were designed to facilitate targeted needle placement in the prostate within a 1.5-T MR imaging unit (CV/i; GE Medical Systems, Waukesha, Wis) with four independent receiver channels. Three fiducial microcoils, each connected to a separate receiver channel, were integrated within the transrectal needle guide. To determine the position and orientation of these coils, we obtained 12 one-dimensional dodecahedrally spaced MR signal readouts (5.0/2.3 [repetition time msec/echo time msec], bandwidth of ±64 kHz, 1° flip angle, 40-cm field of view, 256 readout points), allowing for coil localization, as described previously (20,21). MR signal acquisition for coil localization took approximately 60 milliseconds. Microcoil localization errors due to gradient nonlinearity were avoided by using gradient dewarping algorithms (GE Medical Systems).

Given the positions of the three fiducial microcoils in the MR imaging coordinate system and the location of a given intraprostatic target (also in the MR imaging coordinate system), the remaining task was to determine *(a)* the degree of rotation and translation necessary to position the needle guide such that the needle trajectory would be aligned with the target and *(b)* the depth of needle insertion necessary to reach the target. These parameters can be calculated by using a set of coordinate transformations, with the assumption that all relationships among the microcoil positions, device axis, and needle trajectory are known. These relationships were established by using a device-calibration MR image set on which gadopentetate dimeglumine–enhanced (Magnevist; Berlex Laboratories, Wayne, NJ) fiducial tubes defined the device axis and the needle trajectory; this same calibration image set was used for all of the studies described herein.

Calibrating the microcoil positions with the needle trajectory not only allowed for determination of the degree of rotation and translation necessary to reach the target site, but it also allowed us to define the imaging plane that included both the needle path and the device axis. Real-time MR images were acquired on the basis of the position of the fiducial microcoils so that the needle could be visualized as it was being inserted into the prostate.

All experiments were performed by using the CV/i 1.5-T imaging unit. A fast gradient-echo (GRE) pulse sequence was modified to allow alternating acquisition of the microcoil-tracking MR signal readouts (ie, the 12 dodecahedrally spaced readouts) and real-time fast GRE images. After the location of each coil was determined, the position and orientation of the imaging plane were defined such that the real-time fast GRE image section contained the path of the needle.

Real-time data were processed and displayed on a workstation (Sun Ultra II; Sun Microsystems, Mountain View, Calif) that was connected to the imaging unit with a high-bandwidth data bus (SBS Technologies, Carlsbad, Calif). With the described transrectal device, the tracking sequence is currently performed in 60 msec; image processing, communication, and imaging plane localization, in 150 msec; and image acquisition, in 300–1,300 msec. The entire process yields frame rates of 0.7–2.0 frames per second (depending predominantly on the image acquisition time). One receiver channel was used for the endorectal imaging coil, used to acquire images of the prostate, whereas the other three receiver channels were connected to each of the three fiducial microcoils.

Animal Study Protocol

All animal study protocols were reviewed and approved by the Johns Hopkins University animal care and use committee. A technician anesthetized four mongrel dogs that weighed approximately 25 kg by means of a bolus injection of thiopental; anesthesia was maintained with 1% isoflurane throughout the experiment. An intravenous catheter was placed in the right jugular vein for fluid administration, and a Foley catheter was inserted to help stabilize the prostate and define the position of the prostatic urethra. The animals were placed in a prone position on the MR imaging table with the pelvis slightly elevated (approximately 10 cm), and a 5-inch surface coil was placed on the anterior surface of the abdomen at the level of the prostate. The rectal sheath was inserted into the rectum and docked with the positioning stage, which was then locked in place. All

experiments were performed by four authors (R.C.S., A.K., G.F., E.A.).

Needle Placement

In the first animal study, the accuracy of needle placement was tested in vivo. One canine was positioned in the MR imaging unit, and then T1-weighted fast spin-echo (SE) images (700/9.2, bandwidth of ±31.25 kHz, echo train length of four, 16-cm field of view, 3-mm section thickness, 0.5-mm intersection spacing, 256 × 256 matrix, four signals acquired, imaging time of 3 minutes) of the prostate and surrounding anatomy were acquired. Two receiver channels were used to acquire these images: one for the 5-inch surface coil and one for the rectal coil. A target in the body of the prostate was selected on these images and entered into the real-time control program. We then changed to the real-time fast GRE (5.1/2.3, bandwidth of ±64 kHz, 10° flip angle, 32-cm field of view, 1-cm section thickness, 256 × 128 matrix, imaging time of 0.65 second) imaging and tracking sequence.

While performing the real-time fast GRE MR imaging and tracking sequence, the operator is able to rotate and translate the needle guide from outside of the magnet bore by rotating the two coaxial control rods. On a flat-panel display screen in the room with the MR imaging unit, the operator views both the real-time image section that depicts the trajectory of the needle and the numeric values that indicate the current degree of rotation and translation necessary to set the correct needle trajectory. As the needle guide is moved closer to the target area, these numbers move toward zero, which indicates that no more rotation or translation is necessary.

Once the needle guide is on the proper trajectory, the insertion stop is set to the proper depth (also indicated on the flat-panel display screen), and the needle is pushed until its handle is flush with the stop (Fig 3, *A*). The insertion of the needle is visualized on the imaging room display screen, and once the needle is in place, the needle tip is at the desired target location.

To confirm the location of the needle tip, we acquired a second set of T1-weighted fast SE MR images. These SE MR images were used to minimize needle susceptibility artifacts (by minimizing T2* effects) and therefore maximize the accuracy in locating the needle tip. The location of the needle tip artifact relative to the selected target point was compared by two authors (R.C.S., E.A.). This protocol was repeated for four separate needle insertions.

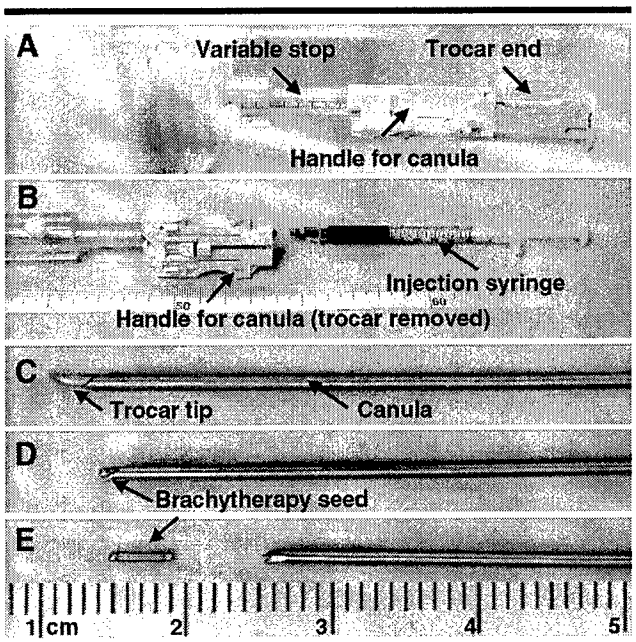

Figure 3. Needle insertion and therapy delivery. *A,* A variable stop is used to control the depth of needle insertion. *B,* After the trocar (ie, inner stylus) is removed, the cannula remains as a hollow conduit through which fluid can be injected into the prostate. *C,* To place brachytherapy seeds, the trocar and cannula are first advanced together. *D,* Then, after the trocar is withdrawn, a brachytherapy seed is pushed to the end of the cannula with a second trocar. *E,* With the trocar held stationary, the cannula is withdrawn, ejecting the seed into the tissue. The trocar and cannula are then withdrawn together.

Intraprostatic Injection

To demonstrate MR image–based monitoring of injected therapies, intraprostatic injections were performed in two canines. Similar to targets in the needle placement study, targets for intraprostatic injection were selected on transverse T1-weighted fast SE MR images, and the needle tip was placed at these locations by using the real-time fast GRE MR imaging and tracking sequence. After the coaxial needle was placed, the trocar (ie, an inner stylus) was withdrawn, leaving only the 18-gauge cannula (ie, a hollow metal tube) in place. This process created a conduit through which injections into the body of the prostate could be performed (Fig 3, *B*).

In this experiment, 0.3 mL of a mixture of 0.4% trypan blue dye (Sigma-Aldrich, St Louis, Mo) and 30 mmol/L gadopentetate dimeglumine was injected into the prostate. During the injection, the flow of the mixture was monitored by using a high-flip-angle radiofrequency-spoiled fast GRE MR imaging sequence (6/1.5, 90° flip angle, bandwidth of ±62.5 kHz, 16-cm field of view, 10-mm section thickness, 256 × 160 matrix, acquisition time of 0.96 second per image). The location of the injected solution was determined by comparing the transverse fast spoiled GRE MR images (80/2.0, 60° flip angle, bandwidth of ±31.25 kHz, 16-cm field of view, 3-mm section thickness, 0.5-mm intersection spacing, 256 × 256 matrix, four signals acquired, imaging time of 1 minute 20 seconds) acquired before with those acquired after the injection. Immediately following the injection procedures and the sacrificing of the animals, the canine prostates were removed, fixed in formalin for 24 hours, sliced into 3-mm axial sections, and then photographed and paired with the corresponding MR image sections by two authors (R.C.S., E.A.).

Brachytherapy Seed Placement

In a fourth canine, the use of the transrectal device for MR image–guided brachytherapy seed placement was demonstrated. Targets were selected, and the trocar and cannula were placed (Fig 3, *C*), as previously described herein. Then, to insert the titanium brachytherapy seeds (OncoSeed Blanks; Medi-Physics, Arling-

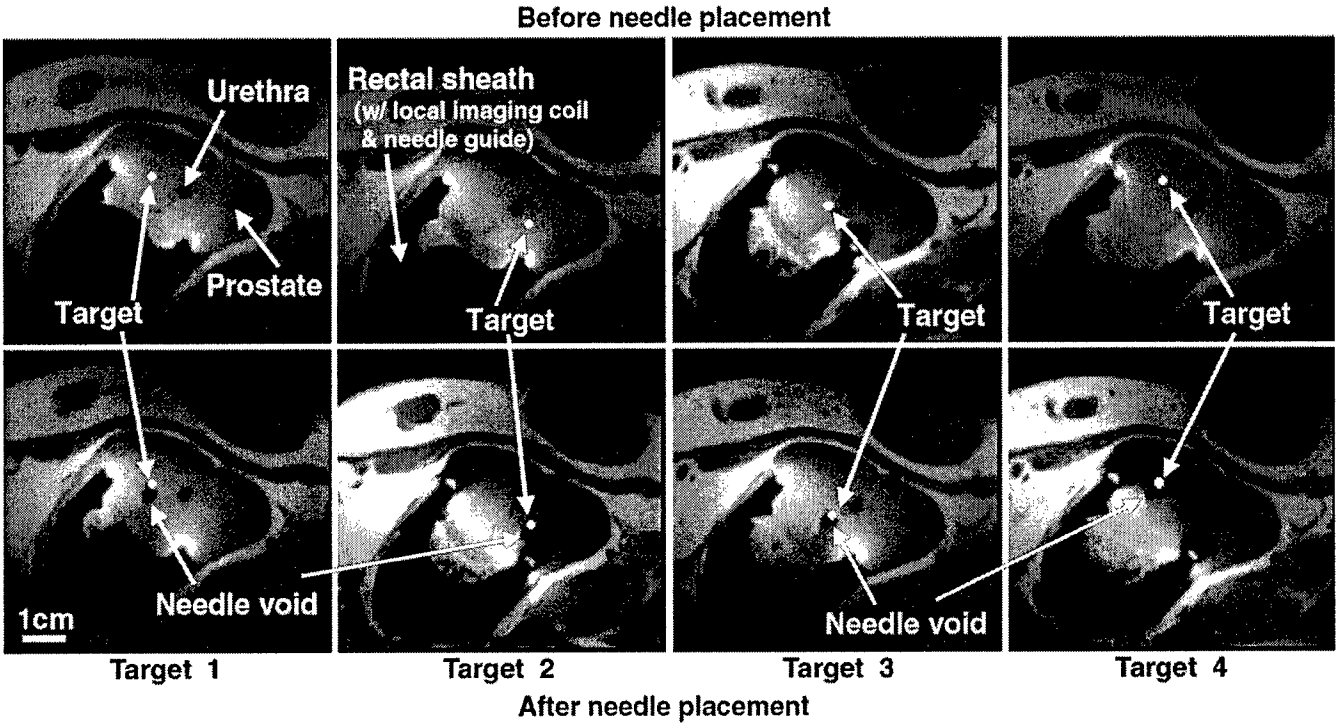

Figure 4. Accurate placement of needles in the canine prostate with use of the transrectal needle guide and microcoil tracking. Top: Four target points in an anesthetized canine were selected on transverse T1-weighted fast SE MR images (700/9.2, bandwidth of ±31.25 kHz, echo train length of four, 16-cm field of view, 3-mm section thickness, 0.5-mm intersection spacing, 256 × 256 matrix, four signals acquired, imaging time of 3 mimutes). Bottom: Transverse T1-weighted fast SE MR images were obtained again after needle placement. The needle tip artifact and the target were found on the same image section, with an in-plane separation of less than 2 mm. Also note that there was minimal motion of the prostate upon needle insertion.

ton Heights, Ill), the trocar was withdrawn, leaving the hollow cannula in place in the prostate. We inserted a brachytherapy seed into the cannula and then advanced it to the end, but not out, of the cannula by pushing it with another trocar (Fig 3, *D*). With the seed at the end of the cannula, we withdrew the cannula slightly while holding the trocar stationary and thus caused the brachytherapy seed to be ejected into the prostate tissue. Subsequently, the trocar and cannula were both withdrawn together (Fig 3, *E*). Three seeds were placed by using this technique. The locations of the needle and the seeds were confirmed by using the same T1-weighted fast SE MR imaging sequence that was used in the needle placement experiments. The MR images were evaluated by two authors (R.C.S., E.A.).

Results

Needle Placement

In the first canine, accurate needle placement in the body of the prostate was achieved. The results of this experiment are summarized in Figure 4. In sequential order, four targets were selected on T1-weighted fast SE images (Fig 4, top row). Having placed the needle by using the fast GRE real-time MR imaging and tracking sequence, we performed fast SE MR imaging again to confirm the placement of the needle by visualizing the needle void (Fig 4, bottom row). In all cases, both the end of the needle artifact and the target were visualized on the same image section (section thickness, 3 mm). Moreover, the center of the needle tip void was found within 2 mm (in-plane) of the selected target. Note also that there was minimal motion of the prostate due to insertion of the needle.

To interpret the results of the needle placement study, it is necessary to examine the artifact created by the 18-gauge MR imaging–compatible needle. Figure 5 shows the artifacts created by the needle and a brachytherapy seed. We aligned the artifacts by placing the physical objects (ie, needle and brachytherapy seed) at the interface of gadopentetate dimeglumine–doped and gadolinium-free gel blocks. Note that the tip void is a circular bloom centered at the end of the actual needle, as has been previously described when the needle is aligned approximately parallel to the static magnetic field, or B_0, with the tip toward the positive magnet pole (22). In all cases, because of the design of the needle placement system, the needle was approximately parallel to the static magnetic field; therefore, the artifact position is a good estimate of the needle tip position.

Because visual confirmation is not possible in vivo, it was difficult to precisely quantify the accuracy of in vivo needle placement. However, in all in vivo experiments, the needle tip was seen on the same MR imaging section as the target (section, 3 mm) and in-plane needle position errors were less than 2 mm.

Intraprostatic Injection

In two canines, the usefulness of this system for MR image–monitored intraprostatic injections was demonstrated. The box on the sagittal scout MR image (left image) in Figure 6 indicates the location of the time-series MR images acquired during the injection of the gadopentetate dimeglumine–trypan blue dye solution. Note that all of the injected solution remained in the prostate. Therefore, it was confirmed—during the injec-

tion procedure—that the full desired dose was delivered to the prostatic tissue.

In Figure 7, the distribution of the contrast agent–dye solution in the prostate of one canine, as depicted on MR images, is compared with the distribution of the solution seen in the gross tissue slices. There is good agreement between the gadolinium-enhanced tissue depicted on the MR images (Fig 7, second column) and the gross tissue slices stained with trypan blue dye (Fig 7, third column).

The intraprostatic injection experiment was repeated in another canine. In this case, however, the MR images showed the injected contrast agent–dye solution leaking out of the prostate and into the surrounding connective tissue (Fig 8). Therefore, it was known—during the injection procedure—that the desired dose was not delivered to the prostate. In Figure 9, the presence of trypan blue dye in the connective tissue at the superior margin of the prostate is confirmed in the gross tissue slices.

Brachytherapy Seed Placement

In the last canine, the application of this system for brachytherapy seed placement in the prostate was demonstrated. Figure 10, *A* shows the selected targets on coronal MR images of the prostate. Figure 10, *B* shows MR images obtained in the same plane after needle placement. Unlike in the needle placement study, in this experiment, the tip of the needle artifact was seen extending beyond the target point. This is because the brachytherapy seeds were placed at the end of the cannula rather than at the end of the trocar, which extended 2 mm past the end of the cannula. Therefore, for proper seed deposition, the trocar must extend 2 mm past the target point.

Figure 10, *C* shows the seeds placed in the prostate after the coaxial needle had been removed. To interpret these findings, it is helpful to refer to Figure 5, which shows the artifact pattern created by the brachytherapy seeds. In Figure 5, the main signal void is seen at the end of the 4-mm seed that lies nearest to the positive pole of the static magnetic field. This signal void corresponds to the signal void seen in Figure 10, *C*. The bodies of the brachytherapy seeds extend 4 mm from this void in the inferior direction (ie, in the direction of the target location). The seeds lie within 3 mm of the selected target location. Also note that intraprostatic bleeding (ie, the dark banding radiating toward the edge of the prostate) resulting from seed placement can be seen near seeds 2 and 3.

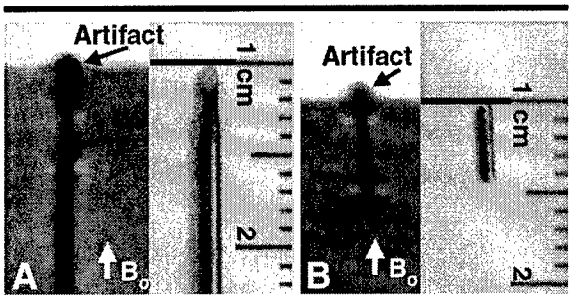

Figure 5. Coronal fast SE MR images (700/9.2, bandwidth of ±31.25 kHz, echo train length of four, 8-cm field of view, 1.5-mm section thickness, 256 × 256 matrix, four signals acquired, imaging time of 3 minutes) obtained in a gel phantom show artifacts created by *A*, the prostate needle and *B*, the brachytherapy seed. Both objects created a uniform signal void along their lengths and a circular bloom, centered on the object tip, at the end facing the positive pole of the static magnetic field. The labeled arrow (B_0) denotes the positive direction of the static magnetic field. The artifacts were aligned by placing the physical objects (ie, needle and seed) at the interface of gadopentetate dimeglumine–doped and gadolinium-free gel blocks.

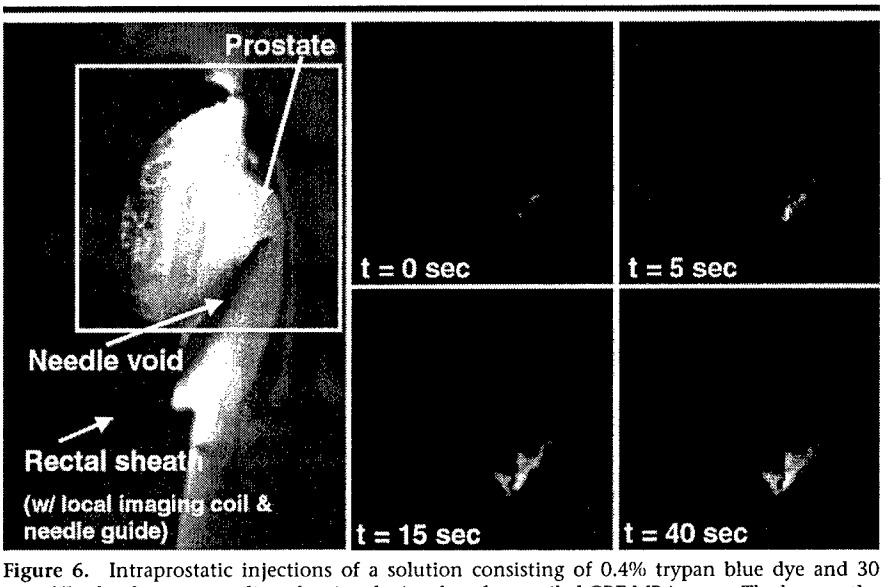

Figure 6. Intraprostatic injections of a solution consisting of 0.4% trypan blue dye and 30 mmol/L of gadopentetate dimeglumine depicted on fast spoiled GRE MR images. The box on the sagittal scout MR image (left) indicates the location of the time-series images (6/1.5, 90° flip angle, bandwidth of ±62.5 kHz, 16-cm field of view, 10-mm section thickness, 256 × 160 matrix, acquisition time of 0.96 second per image). Note that all of the injected contrast agent–dye solution remained in the canine prostate. Therefore, it was confirmed that the full desired dose was delivered to the tissue. *t* = elapsed time between the beginning of contrast agent administration and the image acquisition.

Discussion

Our study results show that needles can be accurately placed in the body of the prostate gland while the subject is in a closed-bore 1.5-T MR imaging unit. Although diagnostic biopsy was not a focus of the current study, it is an obvious subsequent application. Currently, transrectal US–guided needle biopsy is the reference standard for the diagnosis of prostate cancer (23). Although this method has excellent specificity, it is not very sensitive. Transrectal US–guided biopsy does not detect the presence of prostate cancer in approximately 20% of cases (24). MR imaging, in contrast, has high sensitivity for detection of prostate tumors (25). MR imaging alone without concurrent biopsy, however, has low diagnostic specificity.

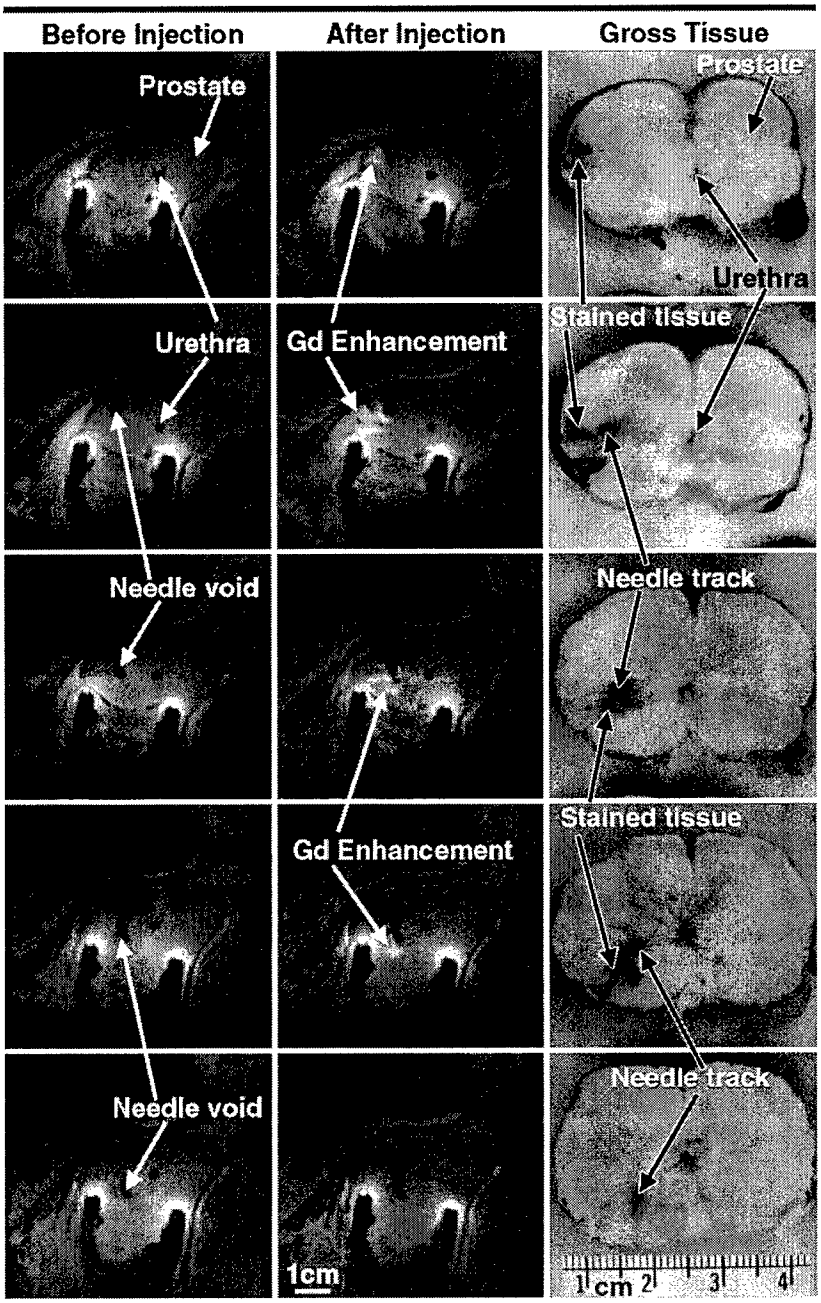

Figure 7. Distribution of injected contrast agent–dye solution depicted on transverse fast spoiled GRE MR images (80/2.0, 60° flip angle, bandwidth of ±31.25 kHz, 16-cm field of view, 3-mm section thickness, 0.5-mm intersection spacing, 256 × 256 matrix, four signals acquired, imaging time of 1 minute 20 seconds) and confirmed in gross tissue slices. The distribution of the gadolinium–blue dye solution as visualized with MR imaging (enhancement seen in postinjection but not preinjection MR images) matches with the distribution of blue-stained tissue seen in the gross tissue slices.

To take advantage of the high diagnostic sensitivity of MR imaging while maintaining the specificity of biopsy, the described transrectal system may be useful for performing MR image–guided prostate biopsy. Although it would not be practical to perform all prostate biopsies with MR image guidance, the excellent tissue contrast achieved with MR imaging is very useful for targeted tissue biopsy. In men who have consistently increasing prostate-specific antigen levels (indicating a high likelihood of cancer) but repeatedly negative US-guided biopsy findings, MR image–guided biopsy may yield a definitive diagnosis. The usefulness of MR imaging in this application area has been demonstrated in a low-field, open-bore magnet by using a transperineal approach to the prostate (26). The system described here is well suited for image-guided biopsy because it uses a standard transrectal approach to the prostate and a closed-bore MR unit; thus, the higher signal-to-noise ratio that is vital for tumor visualization can be achieved. Moreover, higher field strength creates the potential for targeted biopsy of MR spectroscopically defined prostate lesions and thus improved diagnostic accuracy (13).

Second, MR image–targeted prostate biopsy may have the anatomic accuracy that is necessary for long-term monitoring of prostate lesions. With current US-guided biopsy procedures, it is very difficult to repeatedly collect tissue from the same location in the prostate because of poor anatomic visualization. Given the current increase in the early detection of prostate cancers and the prevalence of intermediate-stage prostate tumors, which are associated with an uncertain prognosis (9), it would be very useful to be able to repeatedly "sample" a tumor over a several-year period. This would allow better clinical decision making—for example, definitive prostatectomy or radiation therapy could be delayed until it was absolutely necessary or possibly indefinitely.

With MR imaging, the distribution of therapeutic agents injected into the prostate can be directly verified. MR imaging enables visualization of not only the tissue itself but also the therapeutic agent. It is therefore possible to verify when the tissue has been treated and, most important, when an injection has been unsuccessful—that is, the injected substance has been delivered into surrounding tissue rather than to the desired target area. With the advent of local targeted treatments for prostate cancer (12,27), it is important to confirm that therapy delivery has been successful. Otherwise, a potentially valuable agent could be labeled as ineffective because it never reached the target site.

In the final study of this work, the usefulness of MR imaging for guiding brachytherapy seed placement was demonstrated. Brachytherapy seeds are commonly placed by using transrectal US guidance while the seeds are inserted through the perineal surface (28). Given the poor soft-tissue contrast achieved with US, however, it is common for the seeds to be misplaced in nearby tissue (29). In a recent study (30), radiation

seeds were found in the lungs of 36% of patients after they had undergone US-guided prostate brachytherapy: Seeds may be inadvertently placed in the venous plexus surrounding the prostate, where they then may travel to the lungs. MR image–guided seed placement would be useful in such cases because it yields good anatomic definition. An MR image–guided seed placement system would be suitable for the placement of a few therapy seeds near a small lesion in the prostate.

Two important aspects of the described system design need to be emphasized. First, the stationary rectal sheath is essential for high-spatial-resolution imaging and the stability of the prostate. The thin-walled sheath maintains access to the prostate and thus enables easy rotation and translation of the needle guide while minimizing motion of the surrounding tissue. Because the rectum is very sensitive to pain caused by pressure but relatively insensitive to sharp pain, the system can help minimize patient discomfort during the positioning of the needle guide. In addition, the prostate, which is highly deformable, stays relatively fixed throughout the entire procedure. Without the stationary sheath, motion of the needle guide would result in substantial deformation of the prostate, which would complicate the targeting procedure.

Second, we wish to emphasize the importance of using the described transrectal system with a closed-bore 1.5-T MR imaging unit. The main advantages of MR imaging are high spatial resolution and excellent soft-tissue contrast. Although a low-field-strength, open-bore unit would simplify the design of the needle guide system, low field strength marginalizes the usefulness of MR imaging. Therefore, a system that can be used with a conventional closed-bore magnet was designed so that high-quality MR imaging of the prostate could be maintained.

In conclusion, we have described a transrectal system that allows for image-based monitoring of prostate therapy in a closed-bore 1.5-T MR imaging unit. Applications include MR image–based monitoring of intraprostatic injections and brachytherapy seed placement. Because the described transrectal system is used with closed-bore MR imaging units, it enables one to take advantage of the higher signal-to-noise ratio achieved with conventional magnet designs. At present, we are investigating injected therapies such as those involving the use of alcohol, chemotherapeutic agents, and genetic agents.

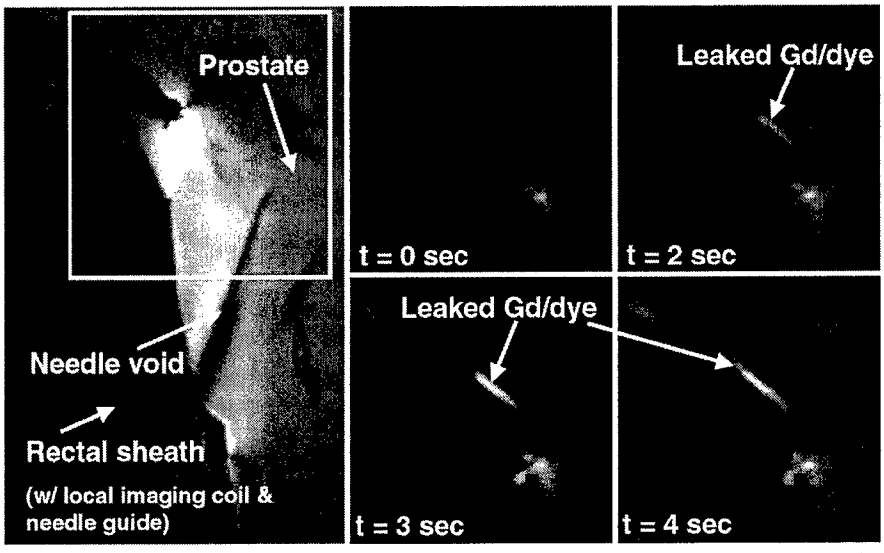

Figure 8. MR image–based monitoring enables detection of faulty injections. The box on the sagittal scout MR image (left) indicates the location of the time-series MR images (6/1.5, 90° flip angle, bandwidth of ±62.5 kHz, 16-cm field of view, 10-mm section thickness, 256 × 160 matrix, acquisition time of 0.96 second per image). In this canine, the injected contrast agent–dye solution leaked out of the prostate and into the surrounding connective tissue. Therefore, it was known—during the procedure—that the desired dose had not been delivered to the prostate. *t* = elapsed time between the beginning of contrast agent administration and the image acquisition.

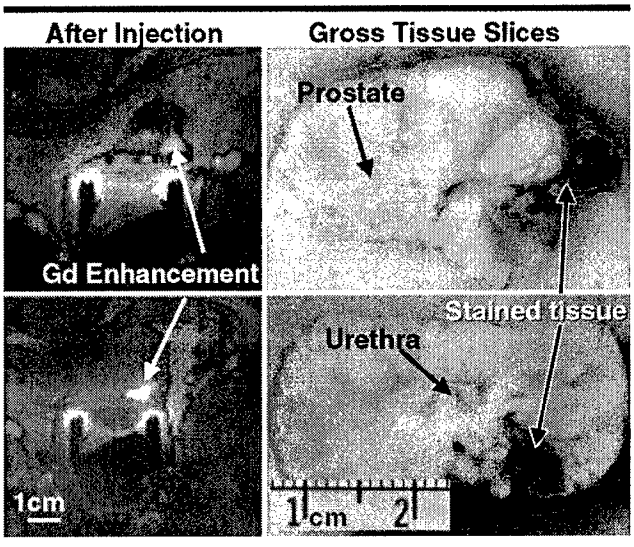

Figure 9. Leakage of injected contrast agent–dye solution into surrounding tissue is confirmed on transverse fast spoiled GRE MR images (80/2.0, 60° flip angle, bandwidth of ±31.25 kHz, 16-cm field of view, 3-mm section thickness, 0.5-mm intersection spacing, 256 × 256 matrix, four signals acquired, imaging time of 1 minute 20 seconds) and in the corresponding gross tissue slices. The distribution of the gadolinium-based solution, seen as an area of high signal intensity (arrows) on the MR images, correlates with the distribution of the solution seen in the stained canine prostate tissue sections. Although some solution remained in the prostate, some solution also passed into the connective tissue at the superior left margin of the posterior region of the prostate.

Acknowledgments: The authors thank Andrew C. H. Yung, MS, for help with the experiments and the endorectal imaging coil design; Jason A. Polzin, PhD, for assistance with the gradient dewarping algorithms; Theodore L. Deweese, MD, for advice regarding clinical applications; and Elliot R. McVeigh, PhD, for providing additional laboratory and imaging resources.

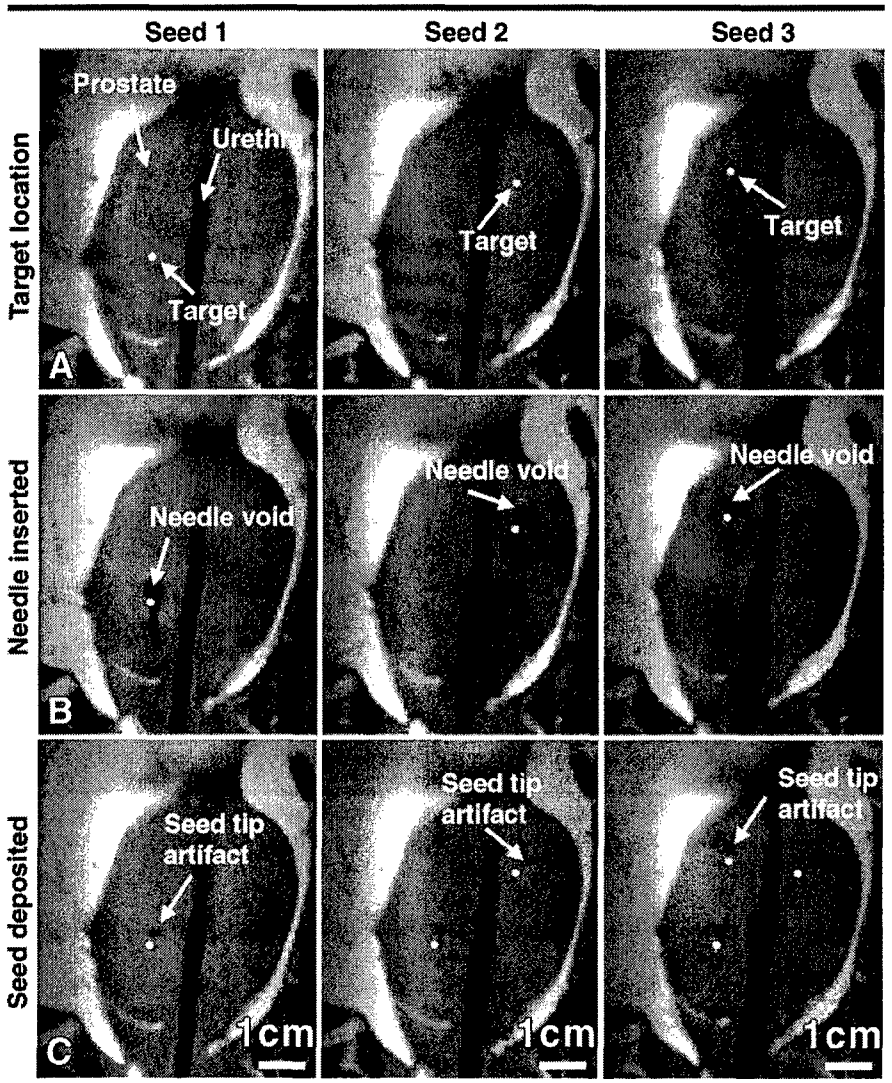

Figure 10. MR image guidance enables accurate placement of brachytherapy seeds in a canine prostate. *A*, Three target areas in one plane of the prostate were selected on coronal fast SE MR images (700/9.2, bandwidth of ±31.25 kHz, echo train length of four, 16-cm field of view, 3-mm section thickness, 0.5-mm intersection spacing, 256 × 256 matrix, four signals acquired, imaging time of 3 minutes). *B*, The needle was placed at these locations as described previously. Because the brachytherapy seeds were placed at the end of the cannula (2 mm back from the end of the trocar tip), the needle artifact extended beyond the target site by approximately 2 mm. In *C*, the seeds have been placed in the prostate. The black bloom artifact at the superior end of the 4-mm brachytherapy seeds is visible. The seeds extended 4 mm from this artifact in the inferior direction.

References

1. Jemal A, Thomas A, Murray T, Thun M. Cancer statistics, 2002. CA Cancer J Clin 2002; 52:23–47.
2. Carter HB, Piantadosi S, Isaacs JT. Clinical evidence for and implications of the multistep development of prostate cancer. J Urol 1990; 143: 742–746.
3. Slawin KM, Ohori M, Dillioglugil O, Scardino PT. Screening for prostate cancer: an analysis of the early experience. CA Cancer J Clin 1995; 45:134–147.
4. Franks LM. Latent carcinoma of the prostate. J Pathol Bact 1954; 68:603–616.
5. Dhom G. Epidemiologic aspects of latent and clinically manifest carcinoma of the prostate. J Cancer Res Clin Oncol 1983; 106:210–218.
6. Brasso K, Friis S, Juel K, Jorgensen T, Iversen P. The need for hospital care of patients with clinically localized prostate cancer managed by noncurative intent: a population based registry study. J Urol 2000; 163:1150–1154.
7. Adolfsson J, Steineck G, Hedlund PO. Deferred treatment of clinically localized low-grade prostate cancer: actual 10-year and projected 15-year follow-up of the Karolinska series. Urology 1997; 50:722–726.
8. Chodak GW, Thisted RA, Gerber GS, et al. Results of conservative management of clinically localized prostate cancer. N Engl J Med 1994; 330: 242–248.
9. Ohori M, Wheeler TM, Scardino PT. The New American Joint Committee on Cancer and International Union Against Cancer TNM classification of prostate cancer: clinicopathologic correlations. Cancer 1994; 74:104–114.
10. Pirtskhalaishvili G, Hrebinko RL, Nelson JB. The treatment of prostate cancer: an overview of current options. Cancer Pract 2001; 9:295–306.
11. Potosky AL, Legler J, Albertsen PC, et al. Health outcomes after prostatectomy or radiotherapy for prostate cancer: results from the Prostate Cancer Outcomes Study. J Natl Cancer Inst 2000; 92:1582–1592.
12. Carroll PR, Presti JC Jr, Small E, Roach M III. Focal therapy for prostate cancer 1996: maximizing outcome. Urology 1997; 49:84–94.
13. Koutcher JA, Zakian K, Hricak H. Magnetic resonance spectroscopic studies of the prostate. Mol Urol 2000; 4:143–152.
14. Yu KK, Hricak H. Imaging prostate cancer. Radiol Clin North Am 2000; 38:59–85.
15. Lederman RJ, Guttman MA, Peters DC, et al. Catheter-based endomyocardial injection with real-time magnetic resonance imaging. Circulation 2002; 105:1282–1284.
16. Yang X, Atalar E, Li D, et al. Magnetic resonance imaging permits in vivo monitoring of catheter-based vascular gene delivery. Circulation 2001; 104:1588–1590.
17. D'Amico AV, Cormack R, Tempany CM, et al. Real-time magnetic resonance image-guided interstitial brachytherapy in the treatment of select patients with clinically localized prostate cancer. Int J Radiat Oncol Biol Phys 1998; 42:507–515.
18. Chen JC, Moriarty JA, Derbyshire JA, et al. Prostate cancer: MR imaging and thermometry during microwave thermal ablation—initial experience. Radiology 2000; 214:290–297.
19. Graham SJ, Stanisz GJ, Kecojevic A, Bronskill MJ, Henkelman RM. Analysis of changes in MR properties of tissues after heat treatment. Magn Reson Med 1999; 42:1061–1071.
20. Dumoulin CL, Souza SP, Darrow RD. Real-time position monitoring of invasive devices using magnetic resonance. Magn Reson Med 1993; 29:411–415.
21. Derbyshire JA, Wright GA, Henkelman RM, Hinks RS. Dynamic scan-plane tracking using MR position monitoring. J Magn Reson Imaging 1998; 8:924–932.
22. Liu H, Martin AJ, Truwit CL. Interventional MRI at high-field (1.5 T): needle artifacts. J Magn Reson Imaging 1998; 8:214–219.
23. Presti JC Jr. Prostate cancer: assessment of risk using digital rectal examination, tumor grade, prostate-specific antigen, and systematic biopsy. Radiol Clin North Am 2000; 38:49–58.
24. Keetch DW, Catalona WJ, Smith DS. Serial prostatic biopsies in men with persistently elevated serum prostate specific antigen values. J Urol 1994; 151:1571–1574.
25. Wefer AE, Hricak H, Vigneron DB, et al. Sextant localization of prostate cancer: comparison of sextant biopsy, magnetic resonance imaging and magnetic resonance spectroscopic imaging with step section histology. J Urol 2000; 164:400–404.
26. Hata N, Jinzaki M, Kacher D, et al. MR imaging-guided prostate biopsy with surgical navigation software: device validation and feasibility. Radiology 2001; 220:263–268.
27. DeWeese TL, van der Poel H, Li S, et al. A phase I trial of CV706, a replication-competent, PSA selective oncolytic adenovirus, for the treatment of locally recurrent prostate cancer following radiation therapy. Cancer Res 2001; 61: 7464–7472.
28. Ragde H, Grado GL, Nadir B, Elgamal AA. Modern prostate brachytherapy. CA Cancer J Clin 2000; 50:380–393.
29. Coakley FV, Hricak H. Radiologic anatomy of the prostate gland: a clinical approach. Radiol Clin North Am 2000; 38:15–30.
30. Ankem MK, DeCarvalho VS, Harangozo AM, et al. Implications of radioactive seed migration to the lungs after prostate brachytherapy. Urology 2002; 59:555–559.

Phased-Array MRI of Canine Prostate Using Endorectal and Endourethral Coils

Andrew C. Yung,[1] Ali Y. Oner,[1] Jean-Michel Serfaty,[1] Mark Feneley,[1] Xiaoming Yang,[1] and Ergin Atalar[1,2*]

A four-channel phased array consisting of one surface coil, two endorectal coils, and one flexible endourethral loop coil was designed for MRI of the canine prostate. The endorectal coils provide high signal in the posterior region of the prostate, while the endourethral and surface coils are sensitive to the central and anterior regions of the prostate. Gel phantom experiments indicate that the proposed phased-array configuration generates 15 times more signal-to-noise ratio (SNR) than a combination of two surface coils and one endorectal coil within the posterior region of the prostate; the performance of the two configurations is comparable near the anterior prostate surface. Ultimate intrinsic SNR (UISNR) analysis was used to compare the proposed phased array's performance to the best possible SNR for external coils. This analysis showed that the proposed phased array outperforms the best-case external coil within the posterior and central regions of the prostate by up to 20 times. In canine experiments in vivo, high-resolution fast spin-echo (FSE) images of the prostate were obtained with a pixel size of 230 μm obtained in 3 min 12 s. The proposed phased-array design potentially can be used to increase the accuracy of prostate cancer staging and the feasibility of MR-guided prostate interventions. Magn Reson Med 49:710–715, 2003. © 2003 Wiley-Liss, Inc.

Key words: prostate MRI; phased array; flexible endourethral loop coil; endorectal coil; ultimate intrinsic SNR

MRI techniques have received much attention for their application to the visualization and treatment of prostate cancer, which is the second largest cause of cancer-related deaths in American men (1). The excellent soft-tissue contrast provided by MRI allows improved visualization of the prostate anatomy, surrounding critical structures (such as the neurovascular bundles and periurethral zone), and the extent of tumor spread. This improved contrast resolution presents a distinct advantage over other prostate imaging modalities such as transrectal ultrasound (TRUS) or CT. For example, prostate cancer does not have a uniform appearance in grayscale ultrasound images; some authors report that up to 56% of prostate carcinomas are in areas that appeared normal under TRUS (2). Consequently, MRI has been used in the management of prostate cancer as a tool for preoperative evaluation (3), cancer staging (4), and image guidance of prostate interventions (5–7). The current state-of-the-art techniques for prostate MRI use an endorectal coil (8), surface coils, or a combination of both (9).

However, current prostate MRI techniques do not provide sufficient image resolution to clearly visualize all features of interest. For example, lesions that are <5 mm in size are difficult to detect when endorectal imaging is used, with a sensitivity of only 10% (10). Endorectal MRI staging gives excellent specificity of extracapsular extension (95%) but suffers from low sensitivity (38%), in part because current methods cannot identify capsular penetrations of <1 mm (11). MR-guided prostate interventions may also suffer from limited image quality, especially during real-time procedures (when imaging time is short) and when the magnetic field strength of the scanner is low (which is often the case for interventional MR suites).

We believe that a higher signal-to-noise ratio (SNR) would improve the ability of MRI to stage prostate cancer, as well as increase the feasibility of MR-guided interventions of the prostate. To achieve this improvement in SNR, we developed a new four-channel phased-array design consisting of two endorectal coils, one endourethral coil, and one surface coil. The use of endourethral coils for prostate imaging is rather novel, and may be an important improvement over current methods because they offer enhanced signal sensitivity in the central region of the prostate. We also attempted to extend the state-of-the-art techniques for prostate MRI by using two rectal coils instead of one, in order to increase signal in the posterior portion of the gland.

To test our ideas, custom endourethral coils and endorectal coils were designed and constructed. In vivo canine experiments and phantom experiments were performed to test the proposed phased-array system, and to compare its performance with other coil configurations that are currently being used for prostate MRI.

METHODS

We constructed a flexible endourethral loop coil and a dual-coil endorectal probe for prostate imaging. Figure 1 shows how the coils are placed in a dog: The dual-coil endorectal probe is placed in the rectum and positioned along the posterior base of the prostate, while the endourethral coil is inserted into the prostatic urethra that runs through the central portion of the gland. An external surface coil is placed on the anterior pelvic surface of the dog.

Flexible Endourethral Loop Coil Design

The flexible endourethral loop coil (shown in Fig. 2a) is implemented as a flexible copper circuit mounted on a

[1]Department of Radiology, NMR Research Division, Johns Hopkins University School of Medicine, Baltimore, Maryland.

[2]Department of Electrical and Electronics Engineering, Bilkent University, Ankara, Turkey.

Grant sponsor: NIH; Grant number: R01 HL 57483; Grant sponsor: United States Army; Grant number: PC 001229.

*Correspondence to: Ergin Atalar, Ph.D., Department of Radiology, NMR Research Division, Johns Hopkins University School of Medicine, 720 Rutland Ave., Traylor Bldg., Rm. 330, Baltimore, MD 21205.
E-mail: eatalar@mri.jhu.edu

Received 16 August 2002; revised 25 October 2002; accepted 1 December 2002.

DOI 10.1002/mrm.10432
Published online in Wiley InterScience (www.interscience.wiley.com).

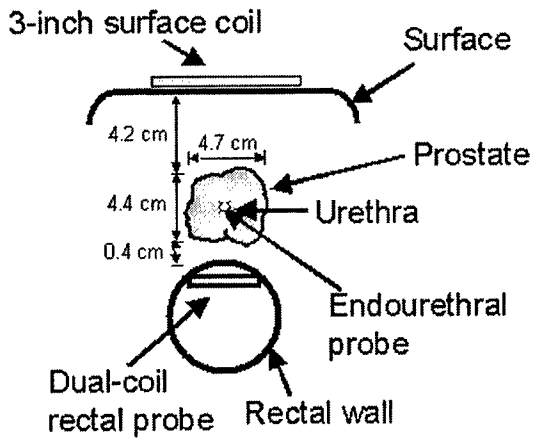

FIG. 1. Coil placement in a canine prostate, and approximate anatomical dimensions.

piece of polyimide film. The sensitive portion of the coil consists of an elongated loop measuring 5 cm in length, with a trace separation of 0.5 cm. Matching capacitors are mounted directly onto the flex circuit itself, in order to transform the coil impedance to the 50 ohms that the scanner preamplifiers expect. The series capacitance in the matching network is distributed over the loop. A decoupling PIN diode mounted on the flex circuit detunes the coil during RF transmission, thereby preventing the coil from interfering with the excitation flip angle. This is achieved by positioning the PIN diode at a certain distance away from the parallel capacitor, so that the line inductance will form a blocking resonance with the parallel capacitor when the PIN diode is switched on during transmit. To choke the ground currents, a quarter-wavelength "bazooka balun" constructed from copper tape was mounted on the coaxial cable that connects the antenna to the scanner. The entire assembly was placed inside a 16-Fr Foley catheter (5.3 mm outer diameter). A previous study of urethral imaging (12) used a similar design.

Dual-Coil Endorectal Probe Design

The endorectal imaging probe (Fig. 2b) consists of two etched loop coils mounted side by side on a printed circuit board. Each loop coil, along with its associated matching/detuning circuitry, is exactly analogous in design to the flexible endourethral loop coil described above. Each loop is rectangular in shape (24 mm × 14 mm), and the coils overlap each other in the lateral direction (jumper wires at the crossover points were used to bridge one coil trace over the other). The coils were mounted on a tapered silicone probe head (3 cm wide) attached to a 24-cm plastic handle, and then covered with a coat of protective plastic. In addition, bazooka baluns made out of copper tape were built on the coaxial cables connecting the coils to the scanner.

The need to reduce crosstalk between the two endorectal loop coils was an important consideration in the probe design. The coils were overlapped to reduce the amount of inductive crosstalk, and a strip of copper tape in the overlap region was used to block the remaining interloop net flux. The elimination of crosstalk was verified by measurements using a network analyzer.

Phantom Experiments

Phantom experiments were undertaken to measure the SNR performance of the coils, and to study electromagnetic interactions between elements of the phased array. The phantom was made from a cylindrical acrylic shell (20.4 cm inner diameter, 24 cm long) filled with polyacrylamide gel, with table salt added to approximate the electrical properties of living tissue (σ = 0.6 S/m, ϵ = 77.7). The coils were situated in such a way as to mimic their placement in a dog, as approximated by previous in vivo canine imaging experiments. Our proposed phased-array configuration (i.e., two endorectal coils, one flexible endourethral loop coil, and one surface coil) was used to acquire images of the gel phantom in a 1.5 T GE Signa scanner. Axial images were obtained using a spin-echo sequence that minimized T_1 and T_2 effects (TE/TR = 9/6000 ms, matrix = 256 × 128, NEX = 1, FOV = 22 cm, slice thickness = 1.5 mm). An alternative phased-array design was also investigated by replacing the flexible endourethral loop coil with an endourethral loopless antenna (2.5 mm in diameter). This design was originally used for transesophageal imaging of the aorta (13). For further comparisons, SNR tests were also performed on a phased array consisting of a Medrad Innervu 1.5T endo-

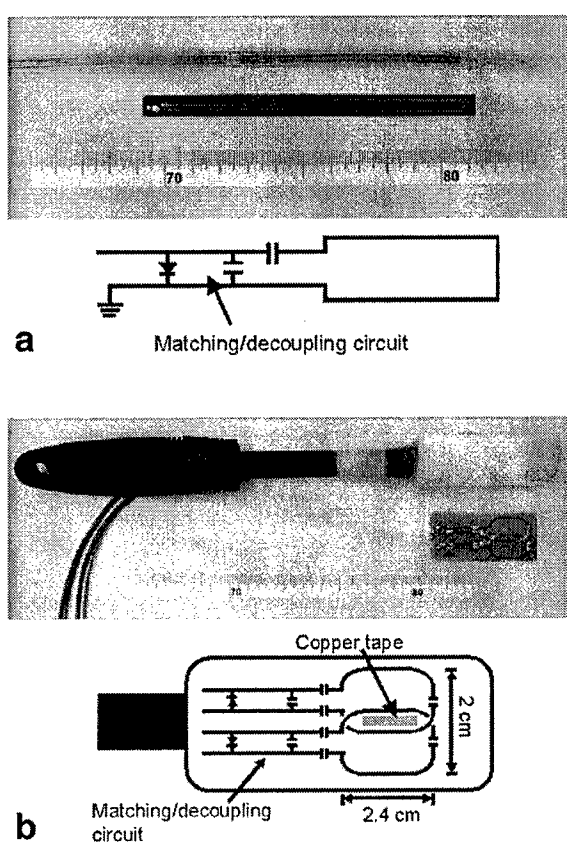

FIG. 2. Photographs and circuit schematics for (**a**) a flexible endourethral loop coil and (**b**) a dual-coil endorectal probe.

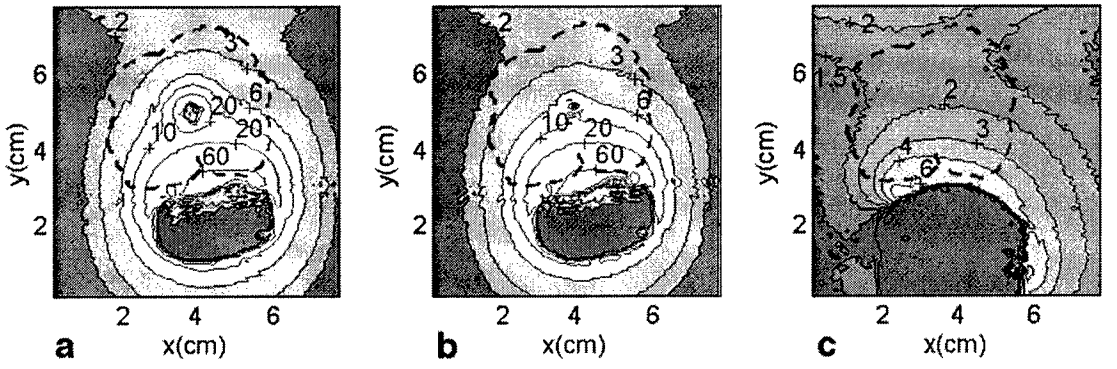

FIG. 3. SNR contour maps in a polyacrylamide phantom for (a) a flexible endourethral loop coil, dual-coil endorectal probe, 3-inch surface coil; (b) a loopless endourethral antenna, dual-coil endorectal probe, 3-inch surface coil; and (c) a Medrad endorectal coil, 3-inch surface coil (anterior), 5-inch surface coil (posterior). The dashed outline denotes the boundaries of the dog prostate.

rectal coil (with the balloon inflated), a 3-inch surface coil on the anterior surface, and a 5-inch surface coil on the posterior surface. This arrangement was used to mimic the endorectal-pelvic phased-array coil combination that is described in the literature (9). SNR maps of the resultant composite images were generated using the optimum reconstruction method, as described in Ref. 14. The amount of isolation between phased-array coil elements was also tested in the polyacrylamide phantom using a network analyzer.

As an additional measure of system performance, ultimate intrinsic SNR (UISNR) analysis (originally proposed by Ocali and Atalar (15)) was performed to determine the best possible SNR that can be produced by external surface coils. Assuming that only external coils are used, the UISNR method determines the best possible SNR for a particular sample geometry (in this case, the cylindrical phantom) by solving for the electromagnetic field that minimizes noise resistance in each voxel. The UISNR formulation originally proposed by Ocali and Atalar (15) used plane wave basis functions to determine the electromagnetic fields. For our purposes, we used cylindrical wave basis functions to construct the field equations. This was done to make the computation of the UISNR more numerically stable, given the phantom's cylindrical symmetry. The number of electromagnetic modes included in the computation was chosen so that any further addition of modes resulted in negligible change (1%) in the final result (13 angular modes and nine longitudinal modes). The UISNR for external surface coils was then compared to the experimentally obtained intrinsic SNR (ISNR) of the proposed phased array.

In Vivo Canine Studies

A series of canine studies ($N = 5$) was performed in a 1.5 T GE scanner. These experiments were conducted in accordance with all regulations set forth by the relevant institutional and governmental agencies. The dogs (weighing approximately 50 kg) were anesthetized throughout the procedure and positioned supine on the scanner bed, caudal end first. Large FOV scout images were acquired to help guide coil placement (as illustrated in Fig. 1) for maximum coverage of the prostate. The flexible endourethral loop coil was surgically inserted into the urethra through a percutaneous cut in the perineum, advanced into the prostatic urethra, and fixated in the prostate by inflating the balloon at the end of its Foley catheter. Once the coils were placed, the prostate was imaged with a series of T_1-weighted and T_2-weighted fast spin-echo (FSE) scans. The in vivo experiment images were reconstructed using the standard sum-of-squares reconstruction technique.

RESULTS

All of the coils matched well, as indicated by measured reflection coefficients ranging from 0.05 to 0.16 in magnitude.

Figure 3 shows phantom SNR measurements for our proposed phased-array system (with the loopless antenna replacing the endourethral loop coil in Fig. 3b), as well as for the combination of the Medrad endorectal coil and two surface coils. An outline of the prostate is shown on the figure to highlight the region of interest (ROI), and the contour values are percentages of the highest SNR value found in all three SNR maps. It is apparent that the loopless endourethral antenna (Fig. 3b) contributes only a small amount of additional SNR, whereas the flexible endourethral loop coil has a greater contribution to the overall signal profile within a diameter of approximately 2 cm around the urethra (Fig. 3a). A comparison of Fig. 3a and c shows that our new phased-array system produces an SNR gain of up to 15 times compared to the Medrad/surface coil combination, within the region of the canine prostate.

Figure 4 shows a coil performance map (CPM) that depicts the ratio between the ISNR produced by our proposed phased-array system and the UISNR for external coils. It is important to note that only internal coils can achieve CPM values of >1, while the CPM values of physically realizable external coils are always <1 (for example, the literature shows cases of external surface coils that produce CPM values of up to 0.8 at certain locations (15)). Within the posterior and central regions of the prostate, the proposed phased-array system performs up to 20 times better than the best-case external surface coil.

Isolation between the two rectal coils was measured to be 23 dB, indicating that good decoupling was achieved.

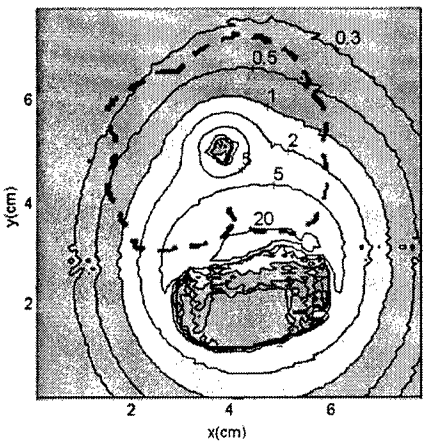

FIG. 4. CPM in a polyacrylamide phantom comparing the prostate phased array SNR with the UISNR for external coils.

Isolation between the flexible endourethral loop coil and other elements in the phased array was dependent on the endourethral coil orientation, and values ranged from 18 to 25 dB. Overall, isolation between coil elements (when tested in the polyacrylamide phantom) was at least 18 dB. In addition, the B_1 distortions in the individual channels were evaluated by two radiologists (J.M.S. and A.Y.O.) and deemed acceptable. The most significant distortion was found in the loop endourethral coil component image, where a "shadow" near the rectal coils was observed. However, the level of this artifact was at least 8–10 times smaller than the actual rectal coil signal.

Figure 5 shows a T_2-weighted axial image of a dog prostate that was generated by the flexible endourethral loop coil and the dual-coil rectal probe (pixel size = 230 μm, acquired in 3 min 12 s). The prostatic capsule and the walls of the urethra (i.e., the periurethral zone) can be seen clearly. A small circular feature that appears to be one of the neurovascular bundles can also be seen in the lower right corner of the image. The bright dot in the urethra

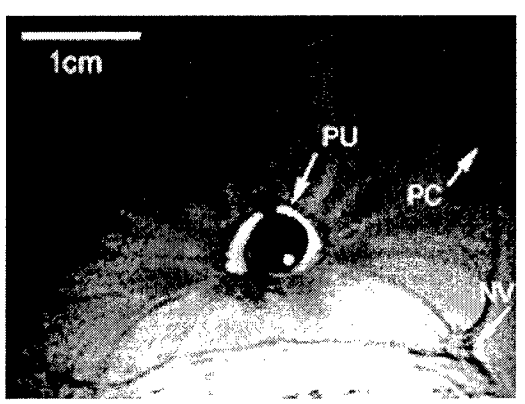

FIG. 5. Axial image of a dog prostate using the flexible endourethral loop coil and dual-coil endorectal probe. Sequence parameters: FSE; TR/TE = 3000/108 ms; FOV = 6 cm; slice thickness = 2 mm; NEX = 4; ETL = 16; matrix = 256 × 256. Arrows points to the periurethral zone (PU), the prostatic capsule (PC), and the possible location of the neurovascular bundle (NV).

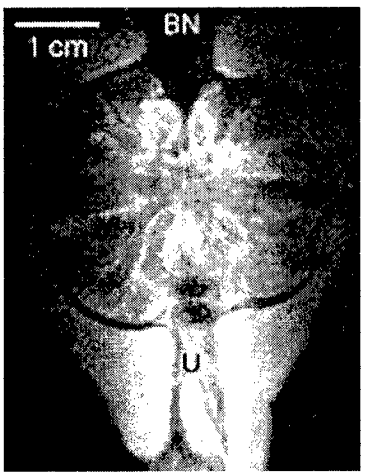

FIG. 6. Coronal image of a dog prostate using the flexible endourethral loop coil. Sequence parameters: FSE; TR/TE = 3500/102 ms; FOV = 8 cm; slice thickness = 2 mm; NEX = 8; ETL = 32; matrix = 256 × 256. The bladder neck (BN) and urethra (U) are visualized.

originated from water inside the Foley catheter's balloon inflation channel, which helped to indicate the orientation of the flexible endourethral loop coil. Figure 6 shows a coronal image of a different dog prostate that was acquired with the flexible endourethral loop coil alone. A pixel size of 310 μm was achieved in 3 min 44 s, with the bladder neck and urethra clearly depicted in the image.

DISCUSSION AND CONCLUSIONS

Increasing the sensitivity of the coil system is an effective way to achieve better MR images of the prostate. Better coil sensitivity may allow an increase in image resolution (without a concomitant increase in imaging time), which in turn allows the visualization of smaller anatomical features. This is especially important in detecting small tumors near the prostatic capsule, due to the increased probability of extraglandular diffusion in these tumors (16). A sensitive coil configuration is also important for increasing the SNR for MR-guided interventions of the prostate, since the field strength is often limited by the need for open magnets to allow for patient access. Again, precise localization of the tumor and the surrounding anatomy is necessary to ensure proper treatment of cancerous tissue while avoiding unwanted morbidity in surrounding critical structures. The desire to improve the performance of such interventional procedures was a direct motivation for our development of an optimized phased-array coil system for the prostate.

In our phased-array system design, the choice of coils was influenced by the geometry of the prostate and the surrounding anatomy. Specifically, each element in the array performs optimally in distinctly different regions of the prostate. The size and placement of the coils on the endorectal probe were chosen to optimize sensitivity in the posterior region of the prostate, while ensuring adequate coverage of the prostate along its entire lateral dimension. The endourethal coil provided high signal in the central part of the prostate along the entire length of the

prostatic urethra. In addition, the 3-inch surface coil was selected to contribute to the SNR in the anterior region of the prostate.

Phantom experiments indicate that the best SNR performance for a dog prostate geometry is produced when the phased array consists of two endorectal coils, one flexible endourethral loop coil, and one surface coil. The endorectal coils provide most of the signal, while the endourethral loop coil further adds to the signal over a diameter of approximately 2 cm around the urethra, as shown in Fig. 3a. Increasing the SNR around the urethra may be clinically important for imaging the central zone found in human prostates, where approximately 20% of the tumors occur (17). In cases in which imaging around the urethra is unimportant (e.g., during examinations of extracapsular extension), the endourethral coil may be omitted from the array. We used the Medrad endorectal/surface coil combination to represent the current state-of-the-art technique for prostate MRI (8). Our proposed phased-array system performed better by a factor of up to 15 times within the ROI. UISNR analysis predicted that the proposed phased-array system outperforms the best-case external surface coil in the posterior and central regions of the prostate, with an up to 20-fold improvement. However, the proposed phased-array system generates lower SNR in the anterior region of the prostate, which indicates that the SNR performance can still be improved. This improvement can be achieved by using multiple coils at the surface.

It is important to note that the choice of coils may change for a different prostate geometry or subject size. For example, the rectal coils are the most significant contributors of signal in the current system. However, if the patient or the prostate is of a larger size (which is often the case for human patients with benign prostatic hyperplasia), the endourethral coil may become more important in providing signal coverage within the prostate. A larger prostate may also make the loopless endourethral antenna a more attractive option, because the signal from a loopless antenna drops off more slowly with distance compared to the signal from the flexible loop version. A larger endorectal coil may also be necessary for a larger prostate.

The in vivo experimental images reveal a high level of anatomic detail, as shown in Figs. 5 and 6. The prostatic capsule, periurethral zone, and bladder neck were visualized in the experimental images, which may be clinically important in determining the extracapsular spread of the disease and preventing harm to such critical structures during interventions. A structure that appears to be the neurovascular bundle can also be identified in Fig. 5. It is especially important to visualize this structure during interventions, because impotence may result if the neurovascular bundle is damaged. Figure 6 shows that high-quality in vivo images can be obtained when only the endourethral loop coil is used. This offers an alternative to the current phased-array system if placement of coils inside the rectum is not possible, as a result of patient refusal, previous surgical resection of the rectum, or other complications in the rectum. Overall, high-quality in vivo images of the canine prostate were obtained with a pixel size as small as 230 μm, and an acquisition time of 3 min 12 s.

The results gleaned from the canine prostate model, while instructive, do not entirely mimic the situation in the human prostate. The canine prostate has none of the zonal anatomy that the human prostate possesses, and the distinction of these zones is important because cancer nodes are more likely to form in certain zones than in others (the peripheral zone in particular). There were also no cancer nodes in the canine prostates that we examined, and therefore the phased array's ability to identify cancerous tissue could not be tested in these experiments. Nevertheless, the current phased-array design may be valuable for animal studies that are performed in support of the development of new prostate imaging techniques and MR-guided prostate interventions (18).

Clearly, human studies must be performed to examine the phased array's utility in staging prostate cancer and guiding prostate interventions. As stated above, the coil geometries may need to be modified in order to account for the larger human prostate geometry. In terms of patient tolerance, the loopless endourethral antenna is attractive because of its small diameter. The flexible endourethral loop coil size also seems acceptable, since 16-Fr Foley catheters are often used in clinical practice. The larger size of the human urethra obviates the need for surgical insertion of the flexible endourethral loop coil into the prostate. The mechanical compliance of the rectal probe may need to be improved before this probe is used in humans.

We believe that the array coils for a human would be comparable in size to the coils used in the current design. In our canine subjects, the separation between the anterior pelvic surface and the prostate was comparable to dimensions found in average human males. For example, this separation distance in the male dataset of the Visible Human Project (19) measured as little as 5.4 cm (as compared to 4.2 cm in the canines). The examined canine prostates were also similar in size to normal adult human prostates (roughly 3 cm $\times$ 4.5 cm $\times$ 4 cm (17)). In more clinically relevant cases, prostates are larger as a result of benign prostatic hyperplasia. However, the design philosophy of a phased-array system for clinical human use would be the same as the design presented in this work, i.e., the use of multiple small endorectal coils to image the posterior region of the prostate, and surface coils and a loop endourethral coil to add signal in the central and anterior regions of the prostate.

ACKNOWLEDGMENTS

The authors thank Mary McAllister for assistance with manuscript preparation. The authors are also grateful to Ken Rent for preparation of the animals, and to Robert C. Susil for technical advice.

REFERENCES

1. Jemal A, Thomas A, Murray T, Thun M. Cancer statistics, 2002. CA Cancer J Clin 2002;52:23–47.
2. Ellis WJ, Brawer MK. The significance of isoechoic prostatic carcinoma. J Urol 1994;152(6 Pt 2):2304–2307.
3. Sanchez-Chapado M, Angulo JC, Ibarburen C, Aguado F, Ruiz A, Viano J, Garcia-Segura JM, Gonzalez-Esteban J, Rodriquez-Vallejo JM. Comparison of digital rectal examination, transrectal ultrasonography, and multicoil magnetic resonance imaging for preoperative evaluation of prostate cancer. Eur Urol 1997;32:140–149.

4. Smith Jr JA, Scardino PT, Resnick MI, Hernandez AD, Rose SC, Egger MJ. Transrectal ultrasound versus digital rectal examination for the staging of carcinoma of the prostate: results of a prospective, multi-institutional trial. J Urol 1997;157:902–906.
5. Porter AT, Blasko JC, Grimm PD, Reddy SM, Ragde H. Brachytherapy for prostate cancer. CA Cancer J Clin 1995;45:165–178.
6. Yerushalmi A. Localized, non-invasive deep microwave hyperthermia for the treatment of prostatic tumors: the first 5 years. Recent Results Cancer Res 1988;107:141–146.
7. Pisters LL, von Eschenbach AC, Scott SM, Swanson DA, Dinney CP, Pettaway CA, Babaian RJ. The efficacy and complications of salvage cryotherapy of the prostate. J Urol 1997;157:921–925.
8. Schnall MD, Imai Y, Tomaszewski J, Pollack HM, Lenkinski RE, Kressel HY. Prostate cancer: local staging with endorectal surface coil MR imaging. Radiology 1991;178:797–802.
9. Hricak H, White S, Vigneron D, Kurhanewicz J, Kosco A, Levin D, Weiss J, Narayan P, Carroll PR. Carcinoma of the prostate gland: MR imaging with pelvic phased-array coils versus integrated endorectal—pelvic phased-array coils. Radiology 1994;193:703–709.
10. Ikonen S, Karkkainen P, Kivisaari L, Salo JO, Taari K, Vehmas T, Tervahartiala P, Rannikko S. Magnetic resonance imaging of clinically localized prostatic cancer. J Urol 1998;159:915–919.
11. Jager GJ, Ruijter ET, van de Kaa CA, de la Rosette JJ, Oosterhof GO, Thornbury JR, Barentsz JO. Local staging of prostate cancer with endorectal MR imaging: correlation with histopathology. Am J Roentgenol 1996;166:845–852.
12. Quick HH, Serfaty JM, Pannu HK, Genadry R, Yeung CJ, Atalar E. Endourethral MRI. Magn Reson Med 2001;45:138–146.
13. Shunk KA, Lima JA, Heldman AW, Atalar E. Transesophageal magnetic resonance imaging. Magn Reson Med 1999;41:722–726.
14. Roemer PB, Edelstein WA, Hayes CE, Souza SP, Mueller OM. The NMR phased array. Magn Reson Med 1990;16:192–225.
15. Ocali O, Atalar E. Ultimate intrinsic signal-to-noise ratio in MRI. Magn Reson Med 1998;39:462–473.
16. Bartolozzi C, Crocetti L, Menchi I, Ortori S, Lencioni R. Endorectal magnetic resonance imaging in local staging of prostate carcinoma. Abdom Imaging 2001;26:111–122.
17. Wong-You-Cheong JJ, Krebs TL. MR imaging of prostate cancer. Magn Reson Imaging Clin N Am 2000;8:869–886.
18. Susil RC, Derbyshire JA, Krieger A, Tanacs A, Solaiyappan M, Whitcomb LL, McVeigh E, Fichtinger G, Atalar E. A realtime MRI system for guidance and monitoring of prostate biopsy. In: Proceedings of the 10th Annual Meeting of ISMRM, Honolulu, 2002. p 2237.
19. Ackerman MJ, Yoo T, Jenkins D. From data to knowledge—the Visible Human Project continues. Medinfo 2001;10(Pt 2):887–890.

Magnetic Resonance in Medicine 52:683–687 (2004)

System for Prostate Brachytherapy and Biopsy in a Standard 1.5 T MRI Scanner

Robert C. Susil,[1] Kevin Camphausen,[2] Peter Choyke,[3] Elliot R. McVeigh,[1,4] Gary S. Gustafson,[5] Holly Ning,[2] Robert W. Miller,[2] Ergin Atalar,[1,6,7] C. Norman Coleman,[2] and Cynthia Ménard[2*]

A technique for transperineal high-dose-rate (HDR) prostate brachytherapy and needle biopsy in a standard 1.5 T MRI scanner is demonstrated. In each of eight procedures (in four patients with intermediate to high risk localized prostate cancer), four MRI-guided transperineal prostate biopsies were obtained followed by placement of 14–15 hollow transperineal catheters for HDR brachytherapy. Mean needle-placement accuracy was 2.1 mm, 95% of needle-placement errors were less than 4.0 mm, and the maximum needle-placement error was 4.4 mm. In addition to guiding the placement of biopsy needles and brachytherapy catheters, MR images were also used for brachytherapy treatment planning and optimization. Because 1.5 T MR images are directly acquired during the interventional procedure, dependence on deformable registration is reduced and online image quality is maximized. Magn Reson Med 52: 683–687, 2004. Published 2004 Wiley-Liss, Inc.†

Key words: MRI; brachytherapy; prostate; prostatic neoplasms; biopsy; interventional MRI

Prostate cancer, with a projected incidence of 220,900 new cases in 2003, is the most commonly diagnosed nonskin cancer in men in the United States (1). Currently, the three most common treatment alternatives for the management of localized prostate cancer are watchful waiting, radical prostatectomy, and radiation therapy. While the first method minimizes treatment-related morbidity, overly conservative management has been associated with poor outcomes (2). While the latter two options offer a good chance of cure, they can cause significant morbidity, including proctitis, incontinence, and erectile dysfunction (3). Therefore, new techniques that can improve the prognostic accuracy of our current diagnostic methods and reduce the morbidity of treatment are warranted.

Both of these goals can be addressed using MRI. Because of its excellent soft-tissue contrast, MRI has great potential to provide accurate image guidance for low-morbidity percutaneous procedures (4). Compared with ultrasound, the most commonly used modality to guide needle placement in the prostate, MRI provides far better visualization of the prostate and surrounding anatomy (4). More important, the advent of molecular imaging promises to improve the diagnostic and prognostic accuracy of imaging by yielding information based on the molecular and metabolic profiles of the tissue (5).

Prior work on MRI-guided prostate interventions has been performed using low-field-strength (e.g., 0.2 or 0.5 T) open-scanner architectures (6,7). While "open" scanners offer improved patient accessibility, they do not provide the highest quality MR images. In an effort to improve image quality while maintaining patient accessibility, some groups have investigated hybrid approaches in which previously acquired 1.5 T MR images were registered with images acquired in the low-field-strength interventional scanner (8–10). Other groups have registered intraoperative ultrasound images with previously acquired 1.5 T MR images (11,12). While both of these approaches simplify the interventional procedure itself, deformable registration between image sets can introduce inaccuracies, particularly in highly deformable tissues such as the prostate.

Here, we present a technique for performing MRI-guided high-dose-rate (HDR) prostate brachytherapy and tissue biopsy within a "closed" 1.5 T scanner architecture. In a series of eight treatments in four patients with prostate cancer, this technique served two purposes. First, it allowed for the acquisition of tissue—for molecular and histological analysis—from specific sites within the prostate that were accurately registered with the MR image data. Second, it provided accurate MR image-guided placement of brachytherapy treatment catheters. In contrast to previous work, we performed these interventions in a standard 1.5 T cylindrical-scanner platform in order to maximize image quality (through higher field strength, improved B_0 homogeneity, and higher gradient performance).

MATERIALS AND METHODS

Percutaneous Needle Guidance

An MRI-compatible system for planning and execution of transperineal needle insertion consisting of a lockable po-

[1]Department of Biomedical Engineering, Johns Hopkins University School of Medicine, Baltimore, Maryland.

[2]Radiation Oncology Branch – NCI, National Institutes of Health, DHHS, Bethesda, Maryland.

[3]Department of Radiology – Clinical Center, National Institutes of Health, DHHS, Bethesda, Maryland.

[4]Laboratory of Cardiac Energetics – NHLBI, National Institutes of Health, DHHS, Bethesda, Maryland.

[5]Department of Radiation Oncology, William Beaumont Hospital, Royal Oak, Michigan.

[6]Department of Radiology, Johns Hopkins University School of Medicine, Baltimore, Maryland.

[7]Department of Electrical and Electronics Engineering, Bilkent University, Ankara, Turkey.

Grant sponsor: US Army; Grant number: PC 10029 Grant sponsors: NSF (Engineering Research Center PER grant), NIH training grant (to R.S.), ASTRO fellowship (to C.M.).

*Correspondence to: Cynthia Ménard, M.D., Radiation Oncology Branch, National Cancer Institute, National Institutes of Health, Building 10, Rm B3B69, 9000 Rockville Pike, Bethesda, MD 20892. E-mail: menardc@mail.nih.gov

Received 12 November 2003; revised 2 February 2004; accepted 17 February 2004.

DOI 10.1002/mrm.20138
Published online in Wiley InterScience (www.interscience.wiley.com).

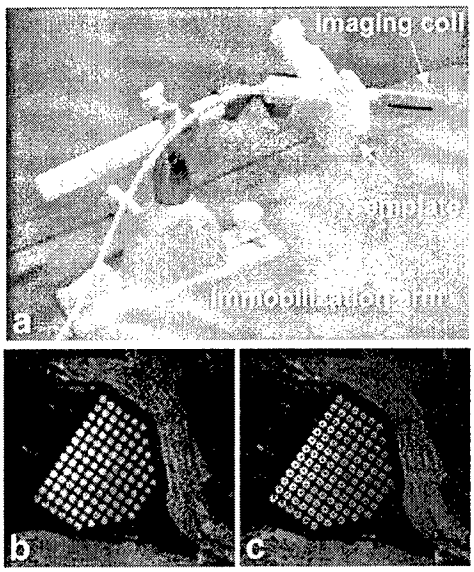

FIG. 1. Needle placement and imaging device. **a:** The needle-guiding template is fixed at a right angle to the endorectal imaging coil. After positioning, both are fixed in place with an immobilization arm. **b:** The template holes, filled with surgical lubricant, are easily visualized in MR images. **c:** After registration of the position and orientation of the needle-guiding template, colored dots (representing the path of each needle hole) are projected through the image volume. Visualization of the template allows for easy verification of this registration.

sitioning arm (Siemens Medical Systems, Erlangen, Germany), an endorectal imaging coil (USA Instruments, Aurora, OH), and a custom-built perineal template was developed for this application (Fig. 1a). The patient was placed in the left lateral decubitus position to maximize perineal exposure in the 1.5 T MR scanner bore (Siemens Sonata, Siemens Medical Systems).

A 3D-SSFP image volume was acquired (with slices approximately coplanar with the needle template face) to register the 3D position of the needle-guiding template relative to the MR image volume (TR = 4.4 ms, TE = 2.2 ms, FA = 56°, pixel BW = 560 Hz, FOV = 25 cm, slice thickness (ST) = 3 mm, 256 × 256, 60 slices, NEX = 1, scan time = 1:20). Prior to positioning, the holes in the needle template were filled with a water-soluble surgical lubricant (Surgilube, Fougera, Melville NY) that both eases catheter insertion and produces strong MR signal (T_1 = 1850 msec and T_2 = 240 msec, measured using FSE and SE pulse sequences, respectively). The regular pattern and spacing of the grid holes were easily recognized in the MR images (Fig. 1b). Using a custom-written image visualization and targeting program (running on a PC networked to the MR scanner), two points are selected to define an x-axis direction, two points to define a y-axis direction, and one point to define the origin of the needle template coordinate system (the middle hole at the exposed face of the template). While defining an origin, an x-axis direction, and a y-axis direction is sufficient to fully constrain the grid coordinate system, significant inaccuracies can be introduced because of angulation errors in the slice-select direction. Therefore, a 0.125" diameter 6 cm long plastic tube was fixed to the anterior surface of the endorectal coil and filled with Surgilube such that it was MR-visible. Because the grid was rigidly fixed at a 90° angle relative to the endorectal coil, the path of the endorectal coil accurately defined the insertion axis of the template coordinate system (the x- and y-axis definitions were automatically updated such that they were normal to the insertion axis).

After the grid was fully registered, the trajectory of each needle hole was extended through the MR image space and superimposed on the image as a colored dot (i.e., each grid hole is projected along the insertion-axis of the template coordinate system). During the procedure, both the MR scanner and the PC running the image display and targeting program were controlled from within the scanner room, the former via an in-room display and mouse (Siemens Medical Systems) and the latter via a cordless mouse and keyboard (Cordless Elite Duo, Logitech, Fremont, CA). The targeting display was projected (LP340b LCD Projector, Infocus, Wilsonville, OR) onto a wall-mounted screen (Da-Mat, Da-Lite, Warsaw, IN) in the scanner room.

Clinical Procedures

After providing informed consent, patients were enrolled in an investigational protocol reviewed and approved by the NIH Clinical Center Institutional Review Board. All patients were being treated for intermediate to high risk localized prostate cancer at the Radiation Oncology Branch of the NCI, NIH Clinical Center. Each of the four patients underwent MRI-guided biopsy and conformal HDR brachytherapy boosts at the beginning and end of a 5-week course of conformal external beam radiation therapy.

HDR prostate brachytherapy uses an Iridium-192 source that is temporarily placed inside the prostate via hollow closed-tip catheters that are inserted through the perineum and into the prostate gland, commonly under ultrasound guidance (13). After parallel and equidistant placement of ~14–18 catheters, a set of axial images is loaded into a brachytherapy dosimetry planning system and the location of the prostate, rectum, bladder, and urethra are defined. The system then optimizes the radiation dose to the prostate while minimizing the exposure of nearby normal tissues and produces a treatment prescription that defines the duration for which the radiation source should dwell at each axial position in each catheter (total radiation time is <20 min). This treatment, as performed under MRI guidance, is similar, with the exception that all planning and placement of catheters were performed within the MRI scanner.

All procedures were performed under general anesthesia. After registration of the perineal grid (as described previously), biopsy sites were selected, a grid hole and insertion depth for each site were read from the targeting application, the patient table was withdrawn from the scanner, and MR-compatible 14-gauge single-action beveled biopsy needles were inserted (MRI Devices, Waukesha WI). The patient was then advanced back into the scanner and, prior to tissue collection, FSE images were acquired to verify placement of the needles (TR = 741 ms, TE = 60 ms, ETL = 7, pixel BW = 125 Hz/pixel, FOV = 25 cm, ST = 4 mm, 256 × 256, 12 slices, NEX = 1, scan time = 0:28).

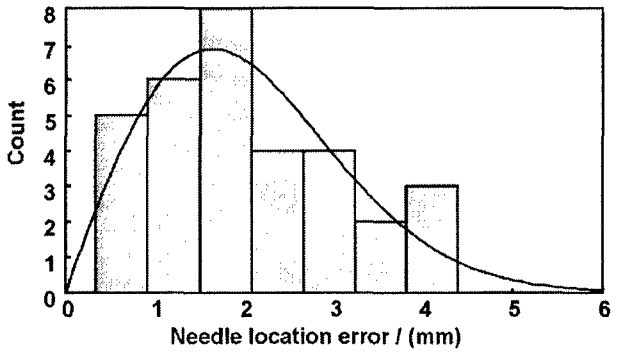

FIG. 2. Needle placement accuracy histogram and maximum-likelihood Rayleigh distribution. Needle location errors (distance, measured in the axial plane, between the needle void and the intended target site) for the 32 biopsy needle placements. The mean placement error was 2.1 mm (error distribution is modeled by a Rayleigh distribution with a sigma value of 1.6 mm).

Following biopsy collection, needle insertion for HDR brachytherapy was performed. Generally, two to four 14-gauge, MR-compatible beveled or straight-tipped guiding needles (MRI Devices) were inserted at a time, after which FSE image volumes were acquired to confirm needle placement. Plastic brachytherapy catheters (5 Fr; Proguide, Nucletron, Columbia, MD) were then inserted through each guiding needle, which was subsequently removed. Catheter depths were chosen such that the entire superior–inferior dimension of the prostate was traversed without puncturing the bladder wall (which lies immediately superior to the prostate).

After placement of all brachytherapy catheters, a final set of T_2-weighted images (in the axial, sagittal, and coronal image planes) were acquired (TR = 3500 ms, TE = 121 ms, ETL = 9, pixel BW = 130 Hz/pixel, FOV = 20 cm, ST = 3 mm, 256 × 256, 26 slices, NEX = 2, scan time = 3:38). The images were forwarded to a brachytherapy dosimetry planning system (PLATO, Nucletron) while the patient was transferred—without moving the needle template or the catheters—to a shielded room for radiation delivery. Currently, the procedure requires ~2 hr for MR scanning and 5 hr for the entire treatment (from patient induction to the end of radiation treatment).

RESULTS

Needle Placement Accuracy

In a series of eight procedures in four patients, this system was used to perform a total of 32 targeted biopsy needle placements within the prostate. The mean biopsy needle placement error was 2.1 mm, 95% of the needle placement errors were less than 4.0 mm, and the maximum error measured was 4.4 mm (Fig. 2). Needle placement error is measured as the distance between the intended target site (i.e., the projection of the needle template hole) and the middle of the signal void created by the biopsy needle. As axial images were acquired and control of insertion depth is very accurate, only errors in the transverse plane were measured. Moreover, because biopsy cores are 1.0 cm long but only 1.5 mm in diameter, a transverse error in needle placement is much more significant than insertion depth error.

High-Dose-Rate Brachytherapy Catheter Placement

Following acquisition of four tissue samples in each patient, 14–15 HDR brachytherapy catheters were placed within the prostate. Total MR-time for placement of the catheters in the first two treatments was 2 hr; catheter placement required 1.5 hr in the subsequent six treatments. Figure 3 shows catheter placements for HDR brachytherapy treatments delivered before (Fig. 3a) and after (Fig. 3b) a 5-week course of external beam radiation therapy. Characteristic changes induced by radiation treatment (namely, atrophy of the normally bright peripheral zone of the prostate) are clearly visible in the second treatment. Figure 3c,d shows radiation isodose contours for each radiation treatment along with contours outlining the prostate, urethra, and the rectum. While the contour maps in Fig. 3 only show dose distribution in 2D, the treatment plan is generated and optimized in 3D using a full volume of MR data. A 3D measure of dose delivery to the prostate, V100 (percent of the target receiving ≥100% of the prescribed dose), was consistently greater than 90%, while a 3D measure of urethral overdose, urethral V125

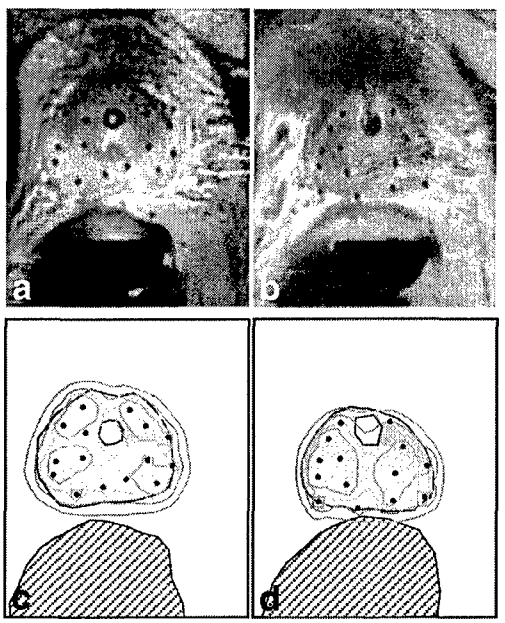

FIG. 3. High-dose-rate (HDR) brachytherapy catheter placement and isodose maps. At the beginning (**a**) and end (**b**) of a 5-week course of external beam radiation therapy, HDR brachytherapy was performed using catheters placed under MRI guidance (both images are from the same patient). **c,d:** Radiation isodose maps, corresponding to **a,b**, indicate 150% (red contour), 125% (orange contour), 100% (green contour), and 75% (blue contour) of the prescribed radiation dose (1050 cGy). The prostate (gray filled region), urethra (white region inside the prostate), and rectum (hatched region) are also shown. Note that the green, 100% dose contour conforms well to the prostate margin, while overdose of the urethra and rectum is avoided.

(percent of the urethra receiving ≥125% of the dose) was <5%.

DISCUSSION

Conventional MR imaging, MR spectroscopic imaging, dynamic contrast-enhanced MRI, and diffusion-weighted MRI have all shown great potential for the diagnosis and assessment of prostate cancer. However, there has been a significant barrier between the collection of these data and its application for targeted tissue acquisition and therapy. It has been widely assumed that the standard architecture of high-field MRI scanners precludes percutaneous access to the prostate. Therefore, most work has focused on the deformable registration of images acquired in high-field scanners (which contain valuable anatomical and functional data) with images acquired via ultrasound, CT, or low-field open MRI (which are more amenable to image-guided interventions). This deformable registration step from MRI to CT or ultrasound has been considered the sine qua non for these procedures (14). Here, we have shown that transperineal needle placement for brachytherapy and tissue biopsy can be effectively performed inside a standard 1.5 T MRI scanner with a 60-cm bore.

As this is a clinical procedure in which the patient is under general anesthesia, we placed great emphasis on choosing a very robust and simple registration technique. While point-based registration techniques have greater precedence in the literature and allow for assessment of registration accuracy (15), we found that unambiguous and rapid localization of single points (i.e., 3 mm diameter glass spheres filled with gadolinium solution) using MRI to be problematic and subject to frequent failure. Therefore, we chose a registration method that relies on more easily recognized patterns (e.g., the gel-filled perineal grid and the long gel-filled tube on the endorectal coil) to increase reliability. With this registration technique, the dominant source of needle placement error appears to be needle deflection within the tissue. In development studies using soft homogeneous gel phantoms (which do not cause appreciable needle deflection), needle placement errors were consistently under 2 mm. In addition, the distribution of needle placement errors (Fig. 2) is accurately modeled using a Rayleigh distribution, which assumes that error has an independent and identical normal distribution in the x- and y-dimensions with no directional bias. This is the expected error distribution if needle deflection, and not some systematic error source, was responsible for the observed errors.

The ability to perform needle placement in a standard MR scanner architecture has several important applications. Primarily, it will allow for the acquisition of tissue biopsies that are accurately colocalized with 1.5 T MR data. Thus, this method provides an ideal platform for the histologic validation of various MR imaging techniques. Prior methods have relied on correlations with tissue biopsy obtained under ultrasound guidance or with deformed whole gland specimens (16), both of which introduce significant localization errors. Second, because MRI provides excellent visualization of both the intra- and periprostatic anatomy, this technique will allow for serial acquisition of tissue from a specified site within the prostate. With techniques such as transrectal ultrasound guidance, it is much more difficult to obtain tissue consistently from the same site within the gland. Serial tissue acquisition will be crucial for the development of prostate cancer therapeutics (i.e., a tumor can be serially biopsied during the course of treatment to study the therapeutic agent's effect on the molecular and histological profile of the tissue) (17). Finally, this technique provides for direct planning and execution of a minimally invasive therapeutic procedure based on high-quality MR images. In previous work in animal models (in a standard 1.5 T scanner), we have demonstrated MRI guidance and monitoring while delivering solid and liquid therapeutic agents to the prostate (18).

In conclusion, a system for percutaneous needle access to the prostate inside a standard 1.5 T MRI scanner has been developed and applied in eight clinical procedures. Despite the relatively small bore size (60 cm) of the scanner, access to the perineum is possible by placing the patient in the left lateral decubitus position. Subsequent work will explore applications of this technique using dynamic contrast enhancement, MR spectroscopic imaging, and diffusion-weighted imaging.

ACKNOWLEDGMENTS

The authors thank Nucletron Inc., USA Instruments, and Siemens Medical for equipment and technical support; Dr. Robert J. Lederman for scanner resources; Frank Harrington for hardware development; Karen Ullman, Nancy Crouse, and Sharon Smith for nursing and therapy support; Victor Wright for imaging technical support; Dr. W. Kammerer for anesthesia; and Dr. Jean Pouliot (UCSF) for assistance with dosimetry software.

REFERENCES

1. Cancer facts & figures. 2003. Atlanta: American Cancer Society; 2003.
2. Chodak GW, Thisted RA, Gerber GS, Johansson JE, Adolfsson J, Jones GW, Chisholm GD, Moskovitz B, Livne PM, Warner J. Results of conservative management of clinically localized prostate cancer. N Engl J Med 1994;330:242–248.
3. Potosky AL, Legler J, Albertsen PC, Stanford JL, Gilliland FD, Hamilton AS, Eley JW, Stephenson RA, Harlan LC. Health outcomes after prostatectomy or radiotherapy for prostate cancer: results from the Prostate Cancer Outcomes Study. J Natl Cancer Inst 2000;92:1582–1592.
4. Yu KK, Hricak H. Imaging prostate cancer. Radiol Clin North Am 2000;38:59–85.
5. Kurhanewicz J, Swanson MG, Nelson SJ, Vigneron DB. Combined magnetic resonance imaging and spectroscopic imaging approach to molecular imaging of prostate cancer. J Magn Reson Imag 2002;16:451–463.
6. D'Amico AV, Cormack R, Tempany CM, Kumar S, Topulos G, Kooy HM, Coleman CN. Real-time magnetic resonance image-guided interstitial brachytherapy in the treatment of select patients with clinically localized prostate cancer. Int J Radiat Oncol Biol Phys 1998;42:507–515.
7. D'Amico AV, Tempany CM, Cormack R, Hata N, Jinzaki M, Tuncali K, Weinstein M, Richie JP. Transperineal magnetic resonance image guided prostate biopsy. J Urol 2000;164:385–387.
8. Cormack RA, D'Amico AV, Hata N, Silverman S, Weinstein M, Tempany CM. Feasibility of transperineal prostate biopsy under interventional magnetic resonance guidance. Urology 2000;56:663–664.
9. Fei B, Duerk JL, Boll DT, Lewin JS, Wilson DL. Slice-to-volume registration and its potential application to interventional MRI-guided radio-frequency thermal ablation of prostate cancer. IEEE Trans Med Imag 2003:22:515–525.

10. Hata N, Jinzaki M, Kacher D, Cormak R, Gering D, Nabavi A, Silverman SG, D'Amico AV, Kikinis R, Jolesz FA et al. MR imaging-guided prostate biopsy with surgical navigation software: device validation and feasibility. Radiology 2001;220:263–268.
11. Kaplan I, Oldenburg NE, Meskell P, Blake M, Church P, Holupka EJ. Real time MRI-ultrasound image guided stereotactic prostate biopsy. Magn Reson Imag 2002;20:295–299.
12. DiBiase SJ, Hosseinzadeh K, Gullapalli RP, Jacobs SC, Naslund MJ, Sklar GN, Alexander RB, Yu C. Magnetic resonance spectroscopic imaging-guided brachytherapy for localized prostate cancer. Int J Radiat Oncol Biol Phys 2002;52:429–438.
13. Martinez AA, Gustafson G, Gonzalez J, Armour E, Mitchell C, Edmundson G, Spencer W, Stromberg J, Huang R, Vicini F. Dose escalation using conformal high-dose-rate brachytherapy improves outcome in unfavorable prostate cancer. Int J Radiat Oncol Biol Phys 2002;53:316–327.
14. Mizowaki T, Cohen GN, Fung AY, Zaider M. Towards integrating functional imaging in the treatment of prostate cancer with radiation: the registration of the MR spectroscopy imaging to ultrasound/CT images and its implementation in treatment planning. Int J Radiat Oncol Biol Phys 2002;54:1558–1564.
15. Fitzpatrick JM, West JB, Maurer CR Jr. Predicting error in rigid-body point-based registration. IEEE Trans Med Imag 1998;17:694–702.
16. Wefer AE, Hricak H, Vigneron DB, Coakley FV, Lu Y, Wefer J, Mueller-Lisse U, Carroll PR, Kurhanewicz J. Sextant localization of prostate cancer: comparison of sextant biopsy, magnetic resonance imaging and magnetic resonance spectroscopic imaging with step section histology. J Urol 2000;164:400–404.
17. Crawford ED, Fair WR, Kelloff GJ, Lieber MM, Miller GJ, Scardino PT, DeAntoni EP. Chemoprevention of prostate cancer: guidelines for possible intervention strategies. J Cell Biochem Suppl 1992;16H:140–145.
18. Susil RC, Krieger A, Derbyshire JA, Tanacs A, Whitcomb LL, Fichtinger G, Atalar E. A system for MRI guided prostate interventions — a canine study. Radiology 2003;228:886–894.

Design of a Novel MRI Compatible Manipulator for Image Guided Prostate Interventions

Axel Krieger, Robert C. Susil, Cynthia Ménard, Jonathan A. Coleman, Gabor Fichtinger, *Member, IEEE*, Ergin Atalar, and Louis L. Whitcomb*, *Senior Member, IEEE*

***Abstract*—This paper reports a novel remotely actuated manipulator for access to prostate tissue under magnetic resonance imaging guidance (APT-MRI) device, designed for use in a standard high-field MRI scanner. The device provides three-dimensional MRI guided needle placement with millimeter accuracy under physician control. Procedures enabled by this device include MRI guided needle biopsy, fiducial marker placements, and therapy delivery. Its compact size allows for use in both standard cylindrical and open configuration MRI scanners. Preliminary *in vivo* canine experiments and first clinical trials are reported.**

***Index Terms*—Biomedical imaging, cancer, magnetic resonance imaging, medical diagnosis, medical treatment.**

I. Introduction

THIS PAPER reports the development of a novel access to prostate tissue under magnetic resonance imaging guidance (APT-MRI) manipulator for MR prostate imaging and precision MRI guided needle placements and reports the results of *in vivo* canine experiments and clinical trials. The manipulator operates inside the spatial confines and high magnetic field of a standard "closed" MR scanner. The principal objective for the manipulator is to provide precise image guided targeting of a needle for therapeutic procedures and biopsy of the prostate. The manipulator is equipped with active fiducial tracking to encode the position of the needle path and is remotely actuated by the physician from outside the bore of the MR scanner. A targeting system displays MR images, including the needle path, and provides a graphical user interface for the physician. We have recently reported the use of a first generation prototype of this manipulator [4], [8], [13]. This paper focuses on the design, materials and construction of a second generation device for clinical trials. The results of these clinical trials, mentioned briefly herein, are reported in [14].

This paper is organized as follows: The remainder of this section reviews background information about prostate diseases and treatments, compares imaging modalities for the prostate, and reviews previous work in this area. Section II reports the design of the manipulator. Section III reports the performance of the manipulator in *in vivo* canine studies and clinical trials.

A. Background and Motivation

Prostate cancer is the most common noncutaneous cancer in American men. In 2003, there will be an estimated 220 900 new cases of prostate cancer in the United States and 28 900 men will die of this disease [6]. There are two common screening methods for prostate cancer: the prostate-specific antigen test (PSA) and the digital rectal exam (DRE) [10]. The PSA concentration in the blood estimates the likelihood of prostate cancer, but is not conclusive. For the DRE, the physician determines whether the prostate gland is enlarged or whether abnormal nodules are present.

When a PSA level is higher than normal or a DRE shows abnormal results, needle biopsy will normally be recommended to determine if a tumor exists and whether the tumor is benign or malignant. The current standard of care for verifying the existence of prostate cancer is transrectal ultrasound (TRUS) guided biopsy. Under ultrasound guidance, the physician places a biopsy needle through the wall of the rectum into the prostate gland. The needle removes a small cylinder of tissue, which is examined under the microscope to determine if cancer is present. Several biopsy samples are normally taken from different areas of the prostate. Usually, 6–18 cores are removed (from upper, mid, and lower areas of the left and right sides) to obtain a representative sample of the gland and to determine how much of the gland is affected by the cancer.

TRUS provides limited diagnostic accuracy and image resolution. In [17], the authors conclude that TRUS is not accurate for tumor localization and therefore precludes the precise identification and sampling of individual cancerous tumor sites. As a result, the sensitivity of TRUS biopsy is only between 60% and 85% [11], [16]. Magnetic Resonance Imaging (MRI) with an endorectal coil affords images with higher anatomical resolution and contrast than can be obtained using TRUS [17]. Although computed tomography (CT) X-Ray imaging is capable of high spatial resolution, MRI's superior soft-tissue

Manuscript received December 22, 2003; revised June 6, 2004. This work was supported in part by the National Science Foundation (NSF) under Grant NSF ERC 9 731 478, in part by the US Army under Grant PC 10029, in part by the National Institutes of Health (NIH) under Grant RO1 HL57483, Grant RO1 HL61672, and Grant RO1 EB02963. *Asterisk indicates corresponding author.*

A. Krieger is with the Department of Radiology and the Department of Mechanical Engineering, The Johns Hopkins University, Baltimore, MD 21218 USA.

R. C. Susil is with the Department of Biomedical Engineering, The Johns Hopkins University, Baltimore, MD 21218 USA.

C. Ménard was with the Radiation Oncology Branch, NCI, NIH-DHHS, Frederick, MD 30325 USA. She is now with the Department of Radiation Oncology, Princess Margaret Hospital, Toronto, ON M5G 2M9, Canada.

J. A. Coleman is with the Urologic Oncology Branch, NCI, NIH-DHHS, Frederick, MD 30325 USA.

G. Fichtinger is with the Department of Radiology, The Johns Hopkins University, Baltimore, MD 21218 USA.

E. Atalar is with the Department of Radiology, The Johns Hopkins University Baltimore, MD 21218 USA, and also with the Department of Electrical and Electronics Engineering, Bilkent University, Ankara, 06533, Turkey.

*L. L. Whitcomb is with the Department of Mechanical Engineering, 123 Latrobe Hall, 3400 N. Charles Street, The Johns Hopkins University, Baltimore, MD 21218 USA (e-mail: llw@jhu.edu).

Digital Object Identifier 10.1109/TBME.2004.840497

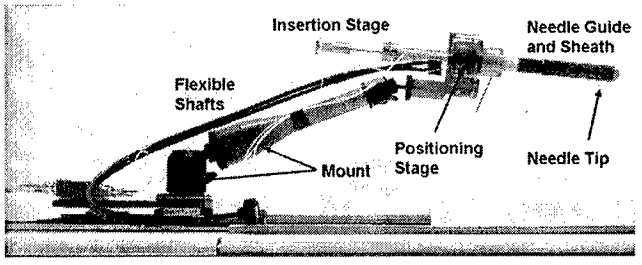

Fig. 1. Picture of the manipulator showing the different components and the needle tip, showing needle guide and sheath, positioning stage, insertion stage, flexible actuation shafts, and mount.

discrimination enables the identification of individual cancerous lesions. MRI guided transperineal prostate biopsy has been demonstrated inside an open MRI scanner [5]. While the transrectal approach is generally well tolerated by patients, the transperineal approach dictates a longer needle path, which may increase patient discomfort.

B. Previous Work in MRI Compatible Interventional Devices

Masamune and colleagues [9] report an in-MRI robot for stereotactic brain surgery for use with open MRI. In [7], Kaiser and colleagues report a 6 degrees of freedom (DOF) robotic system for breast biopsy for the use inside of a "closed" MR scanner. In [2], Chinzei and colleagues report a surgical assist robot for use inside an open MRI scanner. This robot can be used for transperineal access to the prostate. In [1], Beyersdorff and colleagues report a device for prostate biopsy inside a "closed" MR scanner utilizing passive fiducial tracking. In [15], Tajima and colleagues report an MR compatible surgical manipulator for heart intervention designed for vertical magnetic field open-configuration MR imagers. In contrast to these approaches, we have developed a remotely actuated manipulator that operates inside a conventional high-field MRI scanner, which has higher signal-to-noise ratio (SNR) than most open configuration scanners and employs transrectal access to the prostate. This paper reports the first successful device combining MR imaging and tracking coils with a needle for the purpose of image guided prostate intervention.

II. Manipulator Design

This section reports on the design of the manipulator. Placement schematic and the components of the manipulator are described. In addition, design, needles, encoding system and materials for the manipulator are reported. Fig. 1 shows a photo of the manipulator. The manipulator consists of needle guide and rectal sheath, positioning stage, insertion stage, flexible shafts, and mount.

A. Device Operation

Fig. 2 shows a computer-aided design (CAD) drawing of the placement and operation of the robotic device. The device is comprised of a rectal sheath, which is placed adjacent to the prostate in the rectum of the patient and a needle guide, containing a curved needle channel. The sheath is held stationary during the procedure while the needle guide rotates and translates within the sheath. The needle exits the needle guide

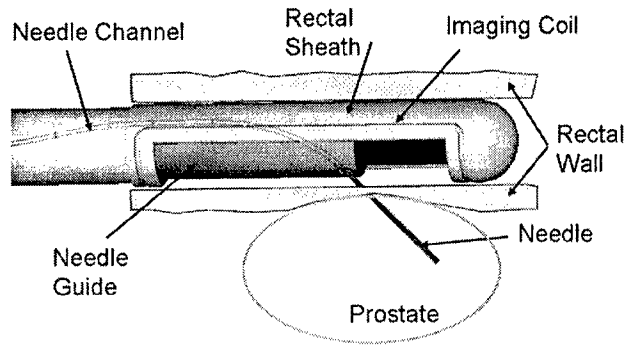

Fig. 2. CAD drawing of needle guide and sheath with curved needle channel. The needle is guided inside the curved needle channel of the needle guide and advanced through a window in the rectal sheath into the prostate.

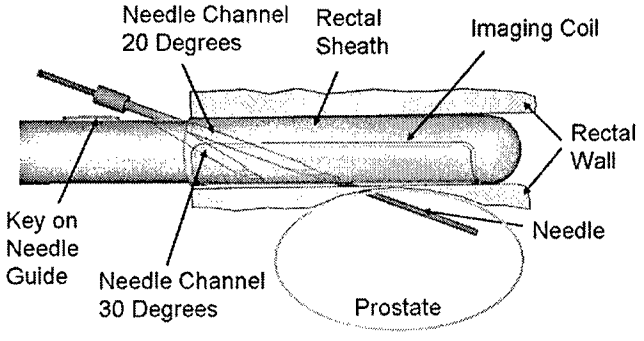

Fig. 3. CAD drawing of needle guide and sheath with straight needle channel. A 20° needle channel for distal parts of the prostate and a 30° channel for proximal parts of the prostate.

through a window in the sheath at a 45° angle between axis of the guide and the needle for optimal coverage of the prostate. Rotation and translation of the needle guide and insertion of the needle are the three DOF necessary for the manipulator to place the needle at a target within the prostate.

Some applications require a straight needle path (Fig. 3). Biopsy, for example, requires fast actuation of the biopsy needle to reliably harvest good biopsy samples. Fast needle actuation is difficult to achieve with a curved channel due to friction induced by the bending of the needle. A straight needle path is therefore preferred for biopsies.

While the curved needle channel allows for unobstructed coverage of the prostate, even with high exit angles, the straight approach is complicated by the constraint of avoiding obstruction by tissue surrounding the proximal end of the needle guide. Therefore, the curved approach is preferable for most applications. Two different needle guides with different needle channels were designed to accommodate for various applications: 1) a needle guide with curved needle channel for injections and fiducial marker placements, and 2) a needle guide with a straight needle channel for biopsies. The sheath for the straight approach contains two slots as windows: one on top for the entry of the needle and one on the bottom for the exit. In straight needle version, the sheath rotates together with the needle guide. A key inside the needle guide riding in the top slot provides the rotation of the sheath. For better coverage of the prostate, the needle guide for the straight approach contains two needle channels: A channel with 30° exit angle for proximal parts of the prostate and a channel with 20° exit angle for the distal parts.

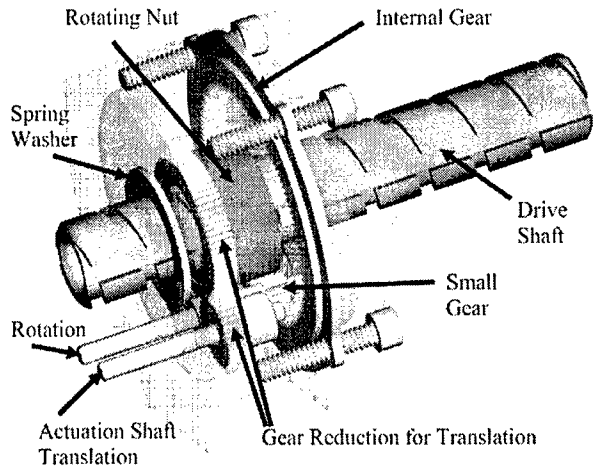

Fig. 4. Transparent CAD drawing of the positioning stage. Rotation of the actuation shaft for translation is converted into pure translation of the drive shaft. Rotation of the actuation shaft for rotation is converted into pure rotation of the drive shaft.

B. Principal Mechanical Components

The positioning stage provides translation and rotation of the needle guide. Fig. 4 shows a semi-transparent view of the positioning stage. It consists of a drive shaft, which is concentrically connected to the needle guide. It contains a through-hole for the needle to pass through the manipulator. Translation is provided through an actuation shaft rotating a nut over a gear reduction, as shown in Fig. 4. The threaded nut drives the shaft. A second actuation shaft rotates a small gear, which engages an internal gear. The internal gear is held stationary by the housing. Upon rotation of the small gear, the entire inner assembly including the actuation shafts rotates. Two keys riding in two horizontal grooves on the drive shaft and which are held by the inner assembly rotate the drive shaft. A spring washer provides enough axial load to prevent unintentional rotation of the drive shaft. The actuation shafts exit the housing via a radial slot on the left side of the housing allowing for 140 degrees of rotation, without compromising structural stability.

Two bidirectional, nonmagnetic phosphor bronze flexible shafts (SS White Technologies, Piscataway, NJ) are attached to the actuation shafts to provide remote actuation from outside the scanner bore. For protection the flex shafts are encased in nylon tubing. The rectal sheath for the curved approach attaches to the positioning stage with a click-in mechanism, comprised of a nylon ball and a flat spring mating with a spherical dent on the right housing of the positioning stage. A similar click-in mechanism is used for attaching the sheath for the straight approach. However, a circular groove is used instead of the spherical dent, to allow for rotation of the sheath. A medical grade heat shrink (Tyco Electronics Corporation, Menlo Park, CA) is fitted around the sheath and covers the window to prevent tissue from being trapped between window and needle guide.

The insertion depth is set by the insertion stage by increasing and decreasing the length of a tubular stop for the needle with a set screw mechanism. A scale is attached to the stop to manually set the length and thus the insertion depth of the needle. The insertion stage docks to the drive shaft of the positioning stage with a click in mechanism, similar to the one of the sheath. A tube is fitted inside the drive shaft to protect the drive shaft and the positioning mechanism from getting in contact with the needle. This limits the number of parts requiring sterilization to the sheath, the needle guide, and the insertion mechanism. The mount consists of a Drylin® T-slide and rail assembly (Igus Inc., E. Providence, RI) for motion along the main axis of the scanner bore and an arm with two integrated ball joints (Manfrotto Trading, Milano, Italy) for adjusting horizontal and vertical position and orientation of the device.

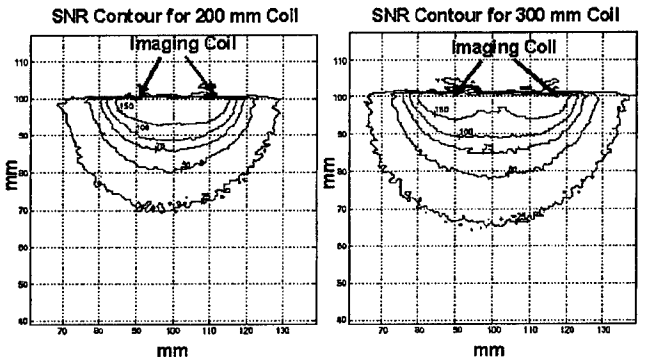

Fig. 5. Signal to noise contours for 200- and 300-mm-wide imaging coil. The graphs show contours of measured SNR level of a cross section of the imaging coil. XY units are in millimeters. The position of the coil is indicated by the arrows.

C. MR Coils

The manipulator contains two types of MR coils: an imaging coil and tracking coils for position encoding.

The imaging coil is looped around the window of the sheath, resting in a groove machined into the sheath. Two design ideas were explored for the sheath containing the imaging coil: with cylindrical cross section and a sheath with elliptical cross section. An elliptical sheath would increase the width of the imaging coil, yielding higher SNR levels. The cylindrical sheath has the advantage of easier machinability and better patient comfort. To make a design choice, we compared the SNR level for an imaging coil on a flexible endorectal coil (MedRad Inc., Indianola, PA) with auto tuning capability of a width of 300 mm, which is achievable with the elliptical design to the SNR level for the cylindrical design with an imaging width of 200 mm. Fig. 5 shows both SNR maps. The increase in SNR of the elliptical design was considered too small to justify higher machining costs and potential increase of patient discomfort, leading to the decision to favor the cylindrical design.

Three tracking micro coils are placed into the manipulator to encode the position of the needle channel. The method is explained in Section II-E.

D. Nitinol Needles

For accurate targeting with the curved approach, the needle needs to exit the channel of the needle guide along a straight trajectory tangential to the arc at the point of exit. A higher exit angle allows for better coverage of the prostate. Higher exit

angle for a given needle guide diameter requires higher curvature of the needle channel. Increasing the curvature of the needle channel beyond a certain point, however, induces plastic deformation (i.e., permanent bending) of the needle, resulting in arching of the needle and missing of the target. Our tests showed that for 18 mm needle guide diameter an adequate exit angle could not be achieved using a standard 18 G (1.3 mm) or larger MRI compatible needle. 18 G Nitinol tube and wire (NDC Nitinol Devices & Components) with its super-elastic ability was determined to provide enough yield strength to prevent it from plastically deforming at an exit angle of up to 45° for an 18-mm-diameter needle guide. MRI Devices Daum provided the grinding of the needle tips and assembly of the connectors and needles to our specifications for use with this new design.

E. 3-D Spatial Position Sensing

We explored three methods for encoding the device position in the MR scanner: Electro optic encoders, passive fiducial tracking and active fiducial tracking.

Electro-optical encoders reliably and accurately encode the position of a robotic joint and were successfully implemented in the MRI environment by using optical connection for the development of a surgical assist robot [2]. However, they require accurate calibration between device coordinate system and MRI coordinate system and suffer from inaccuracies caused by material deflection.

For passive fiducial tracking, fiducial markers composed of water doped with gadolinium-DTPA or other contrast agents are rigidly attached to the end-effector of the device. Gadolinium-DTPA is a commonly used contrast agent that produces large MR signal. Volumetric MR images are taken and after segmenting the marker position in the images the device position can be determined. This method provides position of the end-effector in MRI coordinates, but in order to achieve good accuracy the images have to be of high quality which takes a lot of time, preventing any real time tracking. Additionally, segmentation of the marker position from the rest of the image is very time consuming.

Active fiducial tracking proved to be a fast and accurate encoding method [3]. This method utilizes three tracking micro coils rigidly embedded in the end-effector of the device, which pick up their spatial position in the MRI scanner. A micro coil consists of a wire coil wrapped around a tube filled with a gadolinium-DTPA water solution. A cable connects the antenna coils to the imaging channels of the MRI scanner. The position of the center points of the gadolinium-DTPA tubes is determined by performing a series of twelve 1D projections along different directions, using a frequency encoding gradient. A special MR pulse sequence to produce a series of projections was written. This yields an over-determined linear system for the position of the points, which can be solved using a least square algorithm. The registration sequence takes approximately 50 ms allowing for real time tracking. Two tracking coils are positioned along the axis of the needle guide, while the third coil is placed off axis in the rotating part of the positioning stage, encoding the rotation of the needle guide, Fig. 6.

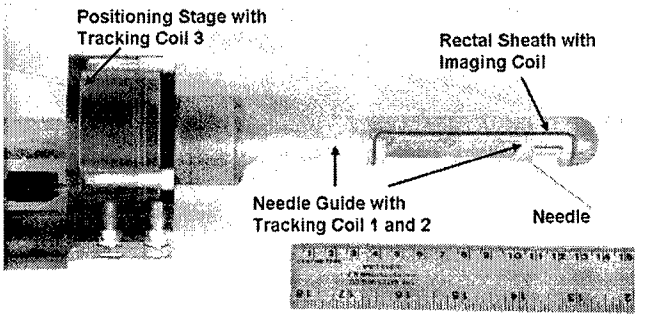

Fig. 6. Detailed picture of sheath, needle guide and positioning stage. The picture shows: the imaging coil, embedded in the rectal sheath, tracking coil 1 and 2 built into the needle guide along the axis, and tracking coil 3, which is attached to the rotating part of the positioning stage.

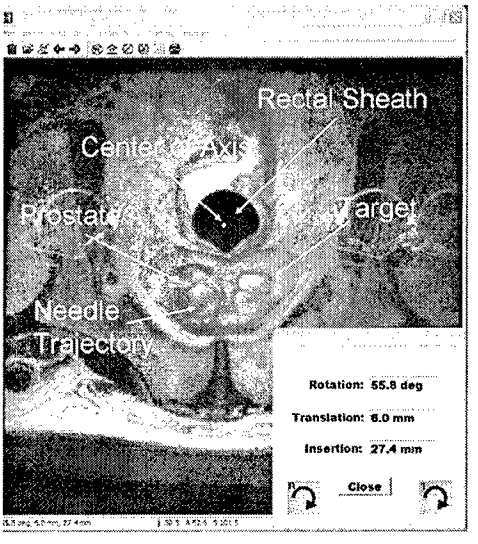

Fig. 7. Screen shot of the visualization and targeting program. An axial T2 weighted MR image containing prostate and rectal sheath is displayed. Intersection points of the device axis and the needle trajectory with the MRI image are visualized as well as the selected target point. The necessary rotation, translation, and insertion values to reach the target are displayed in the lower right corner.

F. MR Image Guidance Software

We developed a custom visualization and targeting program which displays MR images and reads the tracking coil positions. Fig. 7 shows a screen shot of the visualization and targeting program. An axial T2 weighted MR image containing prostate and rectal sheath is displayed. The program overlays a schematic view of the device represented by the intersection points of the device axis and the needle trajectory with the MRI image. After selecting a target position, the program calculates the inverse kinematics and displays necessary rotation, translation and insertion to reach the target. The program is displayed on a screen next to the scanner and the translation, rotation and insertion values are updated every second while the physician uses the actuation shafts of the positioning stage to move the needle guide to the target. The tracking sequence is stopped once the needle trajectory is aligned with the target. The insertion depth is set using the insertion stage and the needle is advanced.

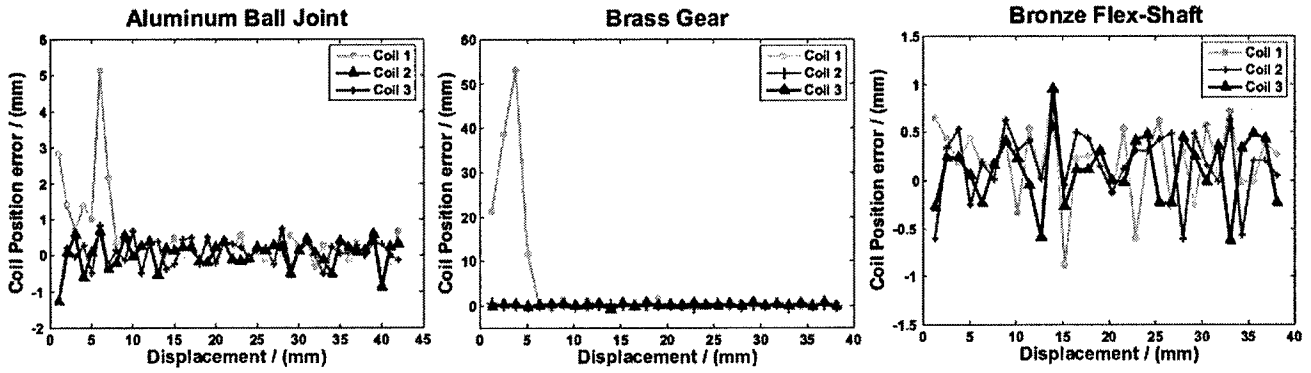

Fig. 8. Graph of tracking coil errors with aluminum ball joint, brass gear and phosphor bronze flex-shaft. The errors in mm are displayed over the displacement from the tracking coil in mm. The three lines indicate the position errors for coil 1, coil 2, and coil 3, respectively. Coil 1 is initially placed adjacent to the metal component. Coil 2 and 3 are not influenced by the metal object.

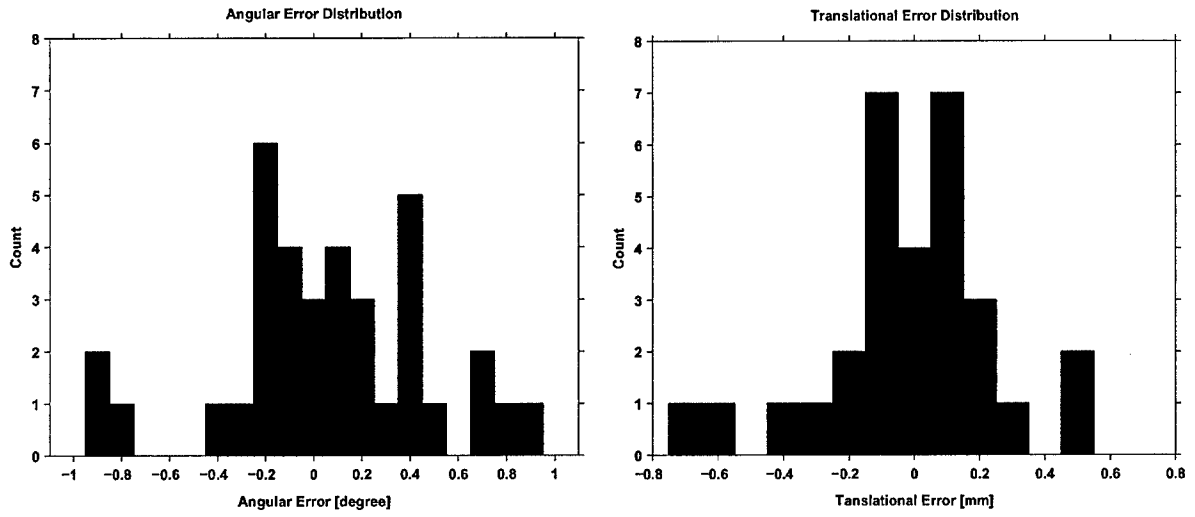

Fig. 9. Angular and translational error distribution for active fiducial tracking. The graphs show histograms of angular and translational encoding error in millimeters and degrees.

G. Materials

Due to the presence of a strong magnetic field inside of an MRI scanner, the use of any ferromagnetic materials is prohibited. Additionally, even nonmagnetic metals can create imaging artifact. These artifacts are caused by a disturbance of the magnetic field due to difference in susceptibility of the metal and surrounding objects. This disturbance also affects the readings of the tracking coils in the vicinity of metals. The magnitude of the disturbance is dependant on the size and on the material of the metal. Very small nonmetallic metals create only a small localized susceptibility artifact and can be neglected on MR images and for tracking coil readings.

To avoid obstruction in anatomical images and introduction of errors in the coil readings, plastic materials are used to build needle guide and sheath, which are in closest vicinity to the field of view (FOV) of the anatomical MR images. Only very small metallic components are used to build these parts: Brass screws for fastening the needle guide to the drive shaft, the flat spring for the click in mechanism of the sheath, which is comprised of phosphor bronze and a thin walled brass tubular liner (Special Shapes Inc.) for the needle channel to protect the plastic from being marred with the needle. Functionality of the manipulator could improve, if parts further away from the FOV may contain more metallic parts.

We developed a test methodology to determine the influence of metallic components on tracking coil readings, which also indicates artifacts on MR images to determine the minimal distance of installation of the components to the FOV and to the tracking coils. The position stage was used for stepped translation of a needle guide containing three tracking coils. The position stage was set up to place one coil (coil 1) initially adjacent to the metal component and the other 2 coils (coil 2 and 3) out of the influenced region to provide undisturbed readings. The needle guide was translated away from the metal component and coil errors over the distance to the component were recorded.

Fig. 8 shows the results of testing a phosphor bronze flexible shaft, a brass gear and an aluminum ball joint. The position error for a tracking coil placed in direct vicinity of the phosphor bronze flexible shaft did not measurably increase compared to the tracking error distribution obtained without any metal parts in the vicinity shown in Fig. 9. This allows us in our design to place the flexible shafts right next to the positioning stage, which contains one of the tracking coils. The error introduced by placing a coil close to the aluminum ball joint significantly

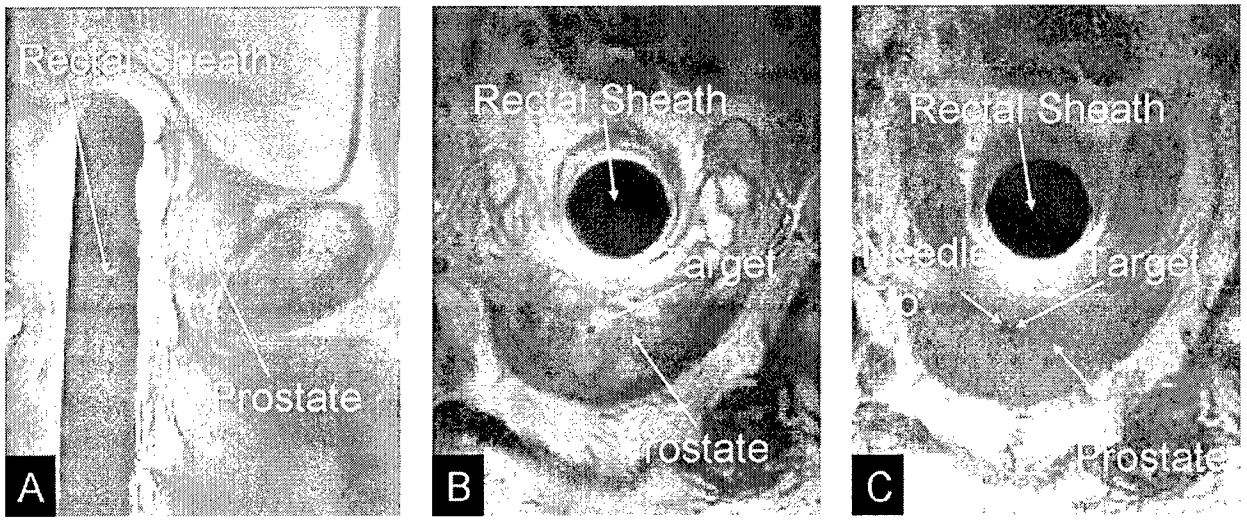

Fig. 10. MR images of the prostate. Panel A: Sagital T2 weighted MR image containing rectal sheath and prostate. Panel B: Axial T2 weighted MR image containing prostate and rectal sheath with selected target. Panel C: Axial T1 weighted image after insertion of the needle, verifying accurate targeting, thus small displacement between target point and the void created by the needle tip.

increased. However the error falls of rapidly to the level of the tracking error distribution without metal when the coil is further than 10 mm away from the ball joint. Adding a safety margin of 20 mm we placed the aluminum ball joint 30 mm away from the positioning stage. The brass gears produced unacceptable errors in the tracking coils and were replaced by plastic gears.

III. Performance Evaluation

All interventions were performed on a GE Signa Excite 1.5 T MR scanner (GE Medical Systems). A protocol was developed for MRI-guided gold fiducial marker placements on patients with prostate cancer prior to treatment with external radiation beam therapy. Fiducial markers are used to adjust for daily set-up changes to optimize targeting of external beam radiation therapy [12]. The two primary goals of this study were to validate the needle targeting accuracy of the manipulator system in clinical practice and to assess the effects of fiducial markers on the outcome of radiation therapy. Four markers were placed into the prostate of each patient using the manipulator system. The target positions for the markers were selected to achieve a diamond like pattern, with two markers placed to the left and right in the middle of the prostate (mid-gland), one marker in the lower part of the prostate (apex), and one marker in the upper part of the prostate (base). After the markers were placed in the prostate, MRI images of the prostate were taken in the radiation treatment position without the transrectal device. These images are co-registered to CT scans using the fiducial markers as common landmarks to aid in target delineation, and digitally reconstructed radiographs (DRRs) are compared to the treatment portal x-rays taken prior to every radiation dose, to achieve optimal beam coverage of the prostate gland. As of today, five patients received implantation of markers. All 20 markers were implanted without complications. For each marker the physician selected the desired marker position on T2 weighted axial and sagital MR images (Fig. 10). The manipulator was actuated to the target location and the physician inserted the needle. After the needle was inserted, MR images were taken to confirm that the location of needle tip was acceptable. The marker was dropped and another MR image was taken after the needle was extracted to visualize the marker position. Target location, needle tip location and center of marker location were recorded for each marker placement to assess the targeting accuracy of our system. The displacement errors for the needle and for the marker were determined on the MRI images as the distance of the needle tip and the center of the marker respectively to the planned target location. The average in-plane displacement error for the needle tip of 20 needle placements was 1.3 mm with a maximum of 2.3 mm. In none of the 20 cases was the needle tip more than one slice (3 mm) away from the slice containing the target position. The average marker displacement error was 4.8 mm with a maximum of 8.3 mm. The increased displacement errors for the marker compared to the needle tip were considered to be caused by deformation of the prostate tissue during insertion of the needle. After the marker is dropped and the needle is extracted, the tissue around the marker relaxes and increases the displacement error.

This section reports on the performance evaluation of the manipulator. First, the accuracy of the tracking method was tested. Subsequently, the manipulator was tested in *in vivo* canine studies and clinical trials.

A. In Vitro Tracking Accuracy Studies

An accuracy test with the proposed tracking method was performed, Fig. 9, using the positioning stage. Precise, stepped translations and rotations were performed and coil positions were recorded after each step to calculate encoding errors. Step size was 1.27 mm for translation and 2° for rotation. The average absolute error for translation was 0.19 mm with a standard deviation of 0.25 mm. For rotation the average absolute error was 0.33° with a standard deviation of 0.42°. For a target that is 30 mm away from the axis of rotation, a rotational error of 0.33° yields a rotational displacement of 0.17 mm. The combined mean displacement due to translational and rotational tracking

error is 0.26 mm. The measured bias for translation is −0.02 mm and for rotation +0.05 mm, yielding a distribution that is close to zero mean. This data indicates that the desired millimeter accuracy for positioning of the manipulator can be achieved using this encoding method.

B. In Vivo Canine Accuracy Studies

A first-generation prototype of this manipulator was used to demonstrate feasibility for different applications of prostate intervention and to assess the accuracy of needle placements. Needle placements, intraprostatic injections, and fiducial markers placements were performed in anesthetized canines, as reported in [13]. The usefulness of the manipulator for accurate needle placements, intraprostatic injections and fiducial markers placements was demonstrated. The maximum in-plane needle displacement error for 4 needles was 2 mm. Because of a slice thickness of 3 mm for the MRI images it is more difficult to exactly determine the error of the insertion depth. In all cases, however, the needle tip was visible in the target slice.

C. In Vivo Clinical Accuracy Studies

In addition to the fiducial marker placements, four biopsy procedures were performed with no adverse patient outcome. The average in-plane displacement error for 20 biopsy needles was 1.8 mm. Further clinical trials are in progress.

IV. Conclusion and Discussion

This paper reported the development of a novel APT-MRI manipulator for MR prostate imaging and precision MRI guided needle placements and reported the preliminary results of *in vivo* canine experiments and clinical trials. Precise image guided targeting of a needle for intraprostatic marker placement and biopsy was achieved.

Tissue deformation was considered to be the main reason for displacement errors. Reducing the tissue deformation, for example by increasing the insertion speed of the needle or fixating the prostate during insertion will be an objective for future work. Another objective will be to enable the use of the manipulator in a 3 T system. The increased SNR of the 3 T system could improve the MR image quality and facilitate the use of functional MRI, such as MR spectroscopy for better target selection.

Acknowledgment

The authors thank J. A. Derbyshire, Ph.D. and E. McVeigh, Ph.D. for help with the tracking coils; J. Polzin for assistance with gradient dewarping; Y. Oner, A. El-Sharkawy, and A. Yung for help with experiments and intrarectal imaging coil design; P. Karmarkar for help with the nitinol needles; W. Krug, M. Franckowiak, and T. Shelly for machining; K. Ullman, P. Choyke, M.D. and P. Guion for help with clinical trials.

References

[1] D. Beyersdorff, A. Winkel, P. Bretschneider, B. Hamm, S. Loening, and M. Taupitz, "Initial results of MRI-guided prostate biopsy using a biopsy device in a closed MR imager at 1.5 T," in *Proc 88th Scientific Assembly and Annu. Meeting Radiological Society of North America*, Chicago, IL, 2002, p. 629.

[2] K. Chinzei, N. Hata, F. Jolez, and R. Kikinis, "MR compatible surgical robot: System integration and preliminary feasibility study," in *Medical Image Computing and Computer-Assisted Intervention 2000.* Berlin, Germany: Springer Verlag, 2000, vol. 1935, pp. 921–930.

[3] C. L. Dumoulin, S. P. Souza, and R. D. Darrow, "Real-time position monitoring of invasive devices using magnetic resonance," *Magn. Reson. Med.*, vol. 29, no. 3, pp. 411–415, Mar. 1993.

[4] G. Fichtinger, A. Krieger, R. C. Susil, A. Tanacs, L. L. Whitcomb, and E. Atalar, "Transrectal prostate biopsy inside closed MRI scanner with remote actuation, under real-time image guidance," in *Lecture Notes in Computer Science*, vol. 2488, Proceedings of the Fifth International Conference on Medical Image Computing and Computer-Assisted Intervention, 2002, pp. 91–98.

[5] N. Hata, M. Jinzaki, D. Kacher, R. Cormak, D. Gering, A. Nabavi, S. G. Silverman, A. V. D'Amico, R. Kikinis, F. A. Jolesz, and C. M. C. Tempany, "MR imaging-guided prostate biopsy with surgical navigation software: Device validation and feasibility," *Radiology*, vol. 220, no. 1, pp. 263–268, Jul. 2001.

[6] A. Jemal, T. Murray, A. Samuels, A. Ghafoor, E. Ward, and M. J. Thun, "Cancer statistics, 2003," *CA Cancer J. Clin.*, vol. 53, no. 1, pp. 5–26, 2003.

[7] W. Kaiser, H. Fischer, J. Vagner, and M. Selig, "Robotic system for biopsy and therapy of breast lesions in a high-field whole-body magnetic resonance tomography unit," *Investigat. Radiol.*, vol. 35, no. 8, pp. 513–519, Aug. 2000.

[8] A. Krieger, R. C. Susil, A. Tanacs, G. Fichtinger, L. L. Whitcomb, and E. Atalar, "A MRI compatible device for MRI guided transrectal prostate biopsy," presented at the 10th Scientific Meeting Society of Magnetic Resonance Imaging in Medicine, Honolulu, HI, 2002, p. 338.

[9] K. Masamune, E. Kobayashi, Y. Masutani, M. Suzuki, T. Dohi, H. Iseki, and K. Takakura, "Development of an MRI-compatible needle insertion manipulator for stereotactic neurosurgery," *J. Image-Guided Surg.*, vol. 1, no. 4, pp. 242–248, Dec. 1995.

[10] J. Naitoh, R. L. Zeiner, and J. B. Dekernion, "Diagnosis and treatment of prostate cancer," *Am. Fam. Physician*, vol. 57, no. 7, pp. 1531–1539, 1541–1512, 1545–1547, Apr. 1998.

[11] M. Norberg, L. Egevad, L. Holmberg, P. Sparen, B. Norlen, and C. Busch, "The sextant protocol for ultrasound-guided core biopsies of the prostate underestimates the presence of cancer," *Urology*, vol. 50, no. 4, pp. 562–566, Oct. 1997.

[12] G. Pang, D. J. Beachey, P. F. O'Brian, and J. A. Rowlands, "Imaging of 1.0-mm-diameter radiopaque markers with megavoltage x-rays: An improved online imaging system," *Int. J. Radiat. Oncol. Biol. Phys.*, vol. 52, no. 2, pp. 532–537, Feb. 2002.

[13] R. C. Susil, A. Krieger, J. A. Derbyshire, A. Tanacs, L. L. Whitcomb, G. Fichtinger, and E. Atalar, "System for MR image-guided prostate interventions: Canine study," *Radiology*, vol. 228, no. 3, pp. 886–894, Sep. 2003.

[14] R. C. Susil, C. Menard, A. Krieger, J. Coleman, K. Camphausen, P. Choyke, G. Fichtinger, L. L. Whitcomb, C. N. Coleman, and E. Atalar, Transrectal prostate biopsy and fiducial marker placement in a standard 1.5 T MRI scanner, 2004, submitted for publication.

[15] F. Tajima, K. Kishi, K. Nishizawa, K. Kan, H. Ishii, M. G. Fujie, T. Dohi, K.-I. Sudo, and S.-I. Takamoto, "A magnetic resonance compatible surgical manipulator: Part of a unified support system for the diagnosis and treatment of heart disease," *Adv. Robot.*, vol. 17, no. 6, pp. 561–575, Sep. 2003.

[16] M. K. Terris, "Sensitivity and specificity of sextant biopsies in the detection of prostate cancer: Preliminary report," *Urology*, vol. 54, no. 3, pp. 486–489, Sep. 1999.

[17] K. K. Yu and H. Hricak, "Imaging prostate cancer," *Radiol. Clin. North Am.*, vol. 38, no. 1, pp. 59–85, Jan. 2000.

Axel Krieger received his B.S. and M.Sc. degrees in mechanical engineering from the University of Karlsruhe, Karlsruhe, Germany, in 2001. He worked as a Research Associate at the Department of Radiology, The Johns Hopkins University, Baltimore, MD, from 2001–2003. Currently he is working towards the Ph.D. degree in the Mechanical Engineering Department at The Johns Hopkins University.

His research interest focuses on the development of MRI compatible devices for MRI-guided interventions.

Robert C. Susil received the B.S. and Ph.D. degrees at The Johns Hopkins University in 1997 and 2003, respectively. He is currently working towards the M.D. degree at The Johns Hopkins University as part of the NIH Medical Scientist Training Program.

His research has focused on developing techniques and devices for performing MRI-guided minimally invasive procedures.

Cynthia Ménard received the M.D. degree from the University of Calgary, Calgary, AB, Canada, in 1996 and completed her residency in radiation oncology at the University of Alberta, Edmonton, AB, Canada, in 2001.

Until 2003 she was an ASTRO Translational Research Fellow in the Radiation Oncology Branch of the National Cancer Institute, NIH. She then held a Staff Clinician appointment and headed the Radiation Oncology Molecular Imaging Section in the Radiation Oncology Branch, NCI, where she pursued research in the development, validation, and clinical application of novel MR imaging techniques to cancer radiotherapy. She is now appointed as a Clinician Scientist in the Radiation Medicine Program at Princess Margaret Hospital in Toronto, ON, Canada.

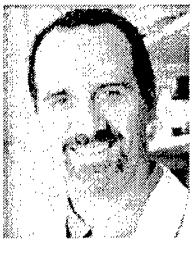

Jonathan A. Coleman received the B.A. degree from Bard College, Annandale-on-Hudson, NY, in 1989 and the M.D. degree (1996) and Residency training in urology (2002) at Cornell University Medical College and Memorial Sloan Kettering Cancer Center,New York.

He then entered the National Cancer Institute (NCI) as an A.F.U.D. sponsored fellow in Urologic Oncology from 2002–2004. He currently holds an appointment as a senior clinical investigator and surgeon at the NCI where he is active in ongoing research and the surgical treatment of genitourinary malignancies including prostate, bladder and kidney cancer. He has published in the field of radiographic imaging and tissue characterization using ultrasound as well as contributing to chapters on urologic oncology in several texts. His current research interests are in imaging and detection strategies for prostate cancer, developing molecular targeting therapies for bladder cancer and the use of laparoscopic surgical approaches in the treatment of prostate and kidney cancer.

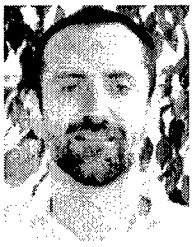

Gabor Fichtinger (M'04) received the B.S. and M.S. degrees in electrical engineering, and Ph.D. degree computer science from the Technical University of Budapest, Budapest, Hungary, in 1986, 1988, and 1990, respectively.

He has balanced academic, industrial, and clinical experience in the development and clinical inauguration of image-guided surgical interventional systems. His specialty is robot-assisted image-guided needle-placement procedures, primarily for cancer therapy. He is an Associate Research Professor of Computer Science, Mechanical Engineering, and Radiology at The Johns Hopkins University, Baltimore, MD. He is trained in therapeutic medical physics.

Mr. Fichtinger is a member of both AAPM and ASTRO.

Ergin Atalar received the B.S. degree from Bogazici University, Istanbul, Turkey, in 1985; the M.S. degree from the the Middle East Technical University, Ankara, Turkey, in 1987; and the Ph.D. degree from Bilkent University, Ankara, Turkey in 1991, respectively.

Immediately after graduation, he joined The Johns Hopkins University, Baltimore, MD, as a Postdoctoral Fellow where he is currently the Director of the Center for Image Guided Intervetions and Professor of Radiology with joint appointments in the Departments of Electrical and Computer Engineering and Biomedical Engineering. He is also a Visiting Professor of Electrical and Electronics Engineering of the Bilkent University. His main research areas are Magnetic Resonance Imaging (MRI)-guided vascular interventions and MRI-guided prostate interventions.

Louis L. Whitcomb (S'86–M'95–SM'02)received the B.S. and Ph.D. degrees from Yale University, New Haven, CT, in 1984 and 1992, respectively.

From 1984 to 1986, he was an R&D Engineer with the GMFanuc Robotics Corporation. From 1992 to 1994, he was a Postdoctoral Fellow at the Woods Hole Oceanographic Institution and at the University of Tokyo. He holds numerous patents in the field of robotics. His research focuses on the design, dynamics, and control of nonlinear dynamical systems. He is a Professor in the Department of Mechanical Engineering, with joint appointment in the Department of Computer Science, at The Johns Hopkins University.

The Prostate

A Preliminary Analysis and Model of Prostate Injection Distributions

Journal:	*The Prostate*
Manuscript ID:	PROS-05-026
Manuscript Type:	Original Article
Date Submitted by the Author:	27-Jan-2005
Complete List of Authors:	Chowning, Scott; Johns Hopkins University School of Medicine, Biomedical Engineering Susil, Robert; Johns Hopkins University School of Medicine, Biomedical Engineering Krieger, Axel; Johns Hopkins University, Mechanical Engineering Whitcomb, Louis; Johns Hopkins University, Mechanical Engineering Atalar, Ergin; Johns Hopkins University School of Medicine, Radiology; Johns Hopkins University School of Medicine, Biomedical Engineering; Bilkent University, Electronics and Electrical Engineering
Key Words:	screening, surveillance, FGF

A Preliminary Analysis and Model of Prostate Injection Distributions

Scott L. Chowning[1], Robert C. Susil[1], Axel Krieger[2,3], Louis L. Whitcomb[3], Ergin Atalar[1,2,4]

Departments of Biomedical Engineering[1] and Radiology[2]
Johns Hopkins University School of Medicine
Baltimore, MD 21205

Department of Mechanical Engineering[3]
Johns Hopkins University
Baltimore, MD 21218

Department of Electrical and Electronics Engineering[4]
Bilkent University
Ankara, Turkey 06533

Correspondence:

Scott Chowning
Johns Hopkins University School of Medicine
Department of Biomedical Engineering
334 Traylor Building
720 Rutland Ave
Baltimore, MD 21205

410-287-6727
schowning@mri.jhu.edu

ABSTRACT

Purpose: Understanding the internal dynamics of prostate injections, particularly injection pattern distribution is a key step to developing new therapies for prostate disease that may be best served with a direct injection approach. Due to excellent properties involving liquid contrast agents, MRI can be used for targeting and monitoring of injections into organs and tissues.

Materials and Methods: Eleven intraprostatic injections were performed in-vivo with canines using a custom transrectal guiding and imaging system for use in a standard 1.5T MR scanner. In addition, fifteen injections were performed on excised cadaveric human prostates, using a MedRad Spectris™ injector system. MRI was used to guide the injections and monitor intraparenchymal injection distribution.

Results: T1 and T2 weighted MR images were correlated with histology to produce three-dimensional data sets that can be used to analyze trends in injection patterns. This analysis was used to develop strategies for injection prediction such as gadolinium preinjections and diffusion weighted imaging guidance. In addition, a rough model of prostate injections is described, and a preliminary injection guide is developed that takes into account the individual clinician's goals for therapy.

Conclusions: MR visualization of injected therapeutic agents allows for prediction and monitoring of drug distributions, possibly improving efficacy and reducing side effects. Injection analysis and modeling may be used to assist in optimizing clinical treatments that require or would benefit from focal parenchymal injections into the prostate.

KEY WORDS: MRI, prostate, injections

INTRODUCTION

There are a number of clinical treatments that involve direct intraparenchymal injection into various organs and tissues [1-4]. New treatments are being studied for prostate interventions, including injections for benign prostate hypertrophy and prostate cancer [5]. Recently, such approaches have been studied using endorectal and transperineal routes, usually under ultrasound guidance although MR is beginning to see use as a possible imaging method for prostatic injections [6]. In the case of BPH, ethanol ablation has been studied as a possible therapy [7]. For prostate cancer applications, new treatment techniques are being developed which include immune system stimulation [8], viral [9, 10], genetic [11], and radiosensitizing techniques [12]. While some treatment agents can be applied via a systemic route, others require a maximum local concentration for effectiveness and therefore focal injection is desirable [13].

Despite the promise of local prostate injections, there are several complicating factors that so far have hindered widespread clinical usage. One problem in particular that has plagued local tissue injections is the faulty assumption that the chemical agent will be delivered to the same site at which it is injected. In addition, leakage is found to be a major problem with intraprostatic injections [6]. It is conceivable that many of these problems may be minimized through a better understanding of prostate injection distribution and probability of failure modes.

With this goal in mind, several imaging modalities have been used to guide and monitor injections, including ultrasound and magnetic resonance imaging. Although

there are several other imaging methods for visualizing injected drug agents ([14-16]), MR is superior in terms of soft tissue contrast [(17)]. Contrast agents have been used previously for prostate imaging under TRUS (trans-rectal ultrasound) imaging guidance [(18)], and contrast-enhanced MR is used here as a tool to predict liquid bulk flow inside the prostate. The goals of this paper are: 1) Use a previously designed and described [(6)] transrectal prostate injection and imaging system to model/analyze in-vivo canine prostate injections; 2) compare/contrast prostate canine injection patterns with human prostate; 3) demonstrate accurate agent distribution confirmation via MR methods; 4) analyze leakage modes in the prostate; 5) show that tissue structure is a strong predictor of bulk flow inside the prostate; 6) develop a model for guiding prostate injection strategies.

METHODS

TRANSRECTAL NEEDLE PLACEMENT SYSTEM

A system that allows for precise needle placement based upon MR image data was employed for this study and described elsewhere in detail [(6)]. For the sake of completeness, the operation of the system is summarized in this section.

Central to the system is a stationary endorectal sheath which includes an integrated single-turn imaging coil and a 'window' that allows for access to the prostate through the anterior wall of the rectum (Figure 1A). Because this sheath remains stationary throughout the procedure, deformation of the soft tissue in and around the prostate is minimized. A cylindrical needle guide, which includes a curved needle channel and three microcoil fiducials, is placed within the endorectal sheath (Figure 1B).

The needle guide has rotational and translational degrees of freedom and therefore, the needle can be directed to any region of the prostate. A microcoil tracking method [~~(19,20)~~19,20] was used to quickly (50 msec) and accurately (mean microcoil position error < 1 mm) locate the position and orientation of an intrarectal needle guide within the MR imaging volume. Using a mechanical positioning mechanism and extended control rods (Figure 1C), the needle guide can be rotated and translated from outside of the scanner bore while the subject is being imaged. A custom-written image visualization and targeting program is used to calculate and display the amount of rotation and translation necessary to align the needle guide with the target. Once the needle guide is positioned on the proper trajectory, an injection needle can be inserted to a controlled depth via an offset stop. In a prior study, consistent needle placement accuracy within 2 mm was demonstrated with this system [6~~(6)~~]. All studies were performed using a GE Signa CV/i 1.5T MR scanner.

CANINE INJECTION PROCEDURES

All animal protocols were reviewed and approved by the Johns Hopkins Animal Care and Use Committee. The canines, each weighing approximately 25 kg, were anesthetized with a bolus injection of thiopental and maintained on 1% isoflurane throughout the experiment. An IV catheter was placed in the right jugular vein for fluid administration and a Foley catheter was utilized to aid in stabilizing the prostate and to define the position of the prostatic urethra. The animals were placed prone on the scanner table with the pelvis slightly elevated (~ 10 cm) with a 5-inch surface coil on the anterior surface of the abdomen at the level of the prostate.

In the first canine, a 30mM solution of Gd-DTPA in normal saline was injected at eight sites within the prostate gland. Different volumes of contrast solution (0.15, 0.3, or 0.6 ml) as well as different injection rates (0.6 to 6 ml/min) were utilized. In all cases except for one, injections were performed directly through the hollow, 18G canula. In one case, injections were performed though an 0.018 inch diameter needle manufacturer from nitinol hypotubing. Because these small-diameter hypotubing needles are so compliant, they were inserted into the tissue through the hollow 18G canula (which was left in place) such that they emerged 3mm past the canula tip. During injection, the flow of the contrast solution was monitored using a high flip-angle, RF-spoiled, gradient echo imaging sequence (FSPGR, TE 1.5 msec, TR 6 msec, FA 90°, BW +/-62.5KHz, FOV 16cm, no slice-selection, 256x160, 0.96 sec/image). The location of the injected solution was determined by comparing gradient echo axial images acquired both before and after the injection (FSPGR, TE 2.0 msec, TR 80 msec, FA 60°, BW +/-31.25KHz, FOV 16cm, slice thickness 3mm, interslice spacing 0.5mm, 256x256, NEX 4, scan time 1:20).

In the second canine, an iterative method for predicting the distribution of an injected therapeutic agent (here, ethanol) was considered. To detect potentially dangerous injections before the ethanol was introduced (i.e., those injections that could damage the urethra), test injections at each targeted site were performed using 0.1 ml of 30 mM gadolinium-DTPA in normal saline. All injections were performed through 0.018 inch diameter nitinol needles. The distribution of this injected solution was visualized on T1-weighted images (TE 9.2 msec, TR 700 msec, BW +/-31.25 KHz, ETL 4, FOV 16cm, slice thickness 3mm, interslice spacing 0.5mm, 256x256, NEX=4, scan time 3:00). Then, if the injection pattern was localized and did not involve the urethra, 0.2 ml of dehydrated

ethanol was injected for tissue ablation. Following the study and animal sacrifice, the prostate was removed, fixed in formalin, and sectioned axially such that tissue lesions could be correlated with the MR images.

HUMAN INJECTION PROCEDURES

A total of 13 fresh excised cadaveric human prostates were removed surgically from the anatomy lab at the Maryland State Anatomy Board with approval from the Johns Hopkins University School of Medicine Biosafety Officer and the director of the anatomy board. Twelve of the prostates were kept in 0.9% isosaline solution and refrigerated for a maximum of 24 hours before the imaging experiments. 0.5 mL of Gd-DPTA was added with 9.5 mL of each of four dyes—black, blue, green, and red—to produce a 5% Gd-DPTA-dye solution.

For each prostate, up to four injection sites were chosen, at different superior/inferior positions within the prostate and targeting different anatomical boundaries within it (central gland, peripheral zone). Since the human prostates were ex-vivo, the injection needle was placed by hand, and position confirmed by T2 weighted MR. Each of the human prostates were positioned with the urethra colinear with the longitudinal axis of the MR bore, with the posterior portion of the gland facing upwards. This setup is close to the anatomical position of a patient laying prone in the MR scanner, which is the typical patient position for endorectal coil experiments in-vivo.

Using fixed prostates is very common in imaging experiments, so to test the effect of chemical fixation on prostate injections, we put one freshly removed prostate immediately into a 10% formalin solution and kept it refrigerated for 2 days prior to the

imaging experiment. Three total injections were done in this prostate in different anatomical regions.

To get a better understanding of how injection parameters such as flow rate and total volume affect injectant dispersion, we devised a series of three experiments. In the first set of experiments, we kept constant the flow rate and total volume injected at 0.1 ml/sec and 1 mL, respectively, and then injected 8 prostates. In the second set of experiments, we increased the total volume injected by 100%, held the flow rate constant, and injected 4 prostates. In a third set of experiments, we kept the total volume injected constant and changed the flow rate from 0.1 mL/sec (N = 8) to 0.2 mL/sec (N = 4).

Before each injection, the following image sequences were acquired in all 3 planes: 1) T1 weighted GRE (TE = 2.8, TR = 85, 60° flip angle, BW = 31.25 kHz, 16 cm FOV, NEX = 4, 3 mm slice thickness, 0.5 mm slice gap); 2) T2 weighted fast spin echo (TE = 60, TR = 5500, BW = 15.6 kHz, ETL = 4, 16 cm FOV, 3 mm slice thickness, 0.5 mm slice gap); and 3) Diffusion weighted images using the GE-developed DWI propeller sequence (TE = 100, TR = 5000, b = 1000, 256 x 256, ETL = 16, 3 mm slice thickness, 0 mm slice gap). The diffusion weighted images were postprocessed using the GE Signa LX console computer into 3 image sets including a baseline unweighted set, an apparent diffusion coefficient map (ADC) and an exponentially weighted ADC map. All DW images were for the axial plane only. A standard GE head coil was used in all human prostate injection experiments. Each injection (except the formalin fixed prostate experiments, see Results section for reasoning/details) was performed by a MedRad Spectris MR Injection System™. During the injection, a high flip angle RF-spoiled fast gradient echo sequence (6/1.5, 90° flip angle, BW = 62.5 kHz, 16 cm FOV, 256 x 160

matrix, 1 second per image) was used to monitor the realtime distribution of the injected contrast agent. Afterwards, the same T1 and T2 image sets described above were re-acquired to show pre and post-contrast images. After each imaging experiment, the prostate was stored in 10% formalin solution for fixation for 3 days, after which it was removed and sliced into 3 mm axial sections for histology analysis.

RESULTS

SINGLE CANINE INJECTION DISTRIBUTION PATTERNS

In the first canine, a series of eight transrectal intraprostatic needle placements and injections were performed. During each injection, a high-flip-angle, RF-spoiled, gradient-echo acquisition was run to visualize the agent's distribution. Dynamic images acquired during five of the injections are shown in Figures 2 through 5. Each figure shows a sagittal scout along with individual frames from the time-series images. In the majority of cases, much of the solution does not stay within the tissue but rather, leaks into surrounding structures. In Figure 2, the solution tracks superiorly along the interface between the rectum and the prostate. Figure 3 shows a case where the solution gathered along the needle path, which is brightly enhanced by the end of the injection. In two cases, the injected solution stayed very concentrated within the tissue (as seen in Figure 4). In Figure 5, the solution penetrated to the middle of the prostate and then tracked up the urethra towards the bladder.

MULTIPLE CANINE INTRAPROSTATIC INJECTIONS

As prostate cancer is often considered to be a multifocal disease, it may be desirable to deliver a therapeutic agent to the entire gland. Therefore, we examined the feasibility of covering large regions of tissue in the prostate by performing multiple injections. The eight injections performed in the first canine were all targeted within two axial planes; the first 5 injections were performed in one plane and the last 3 in another. The results of the first six injections are shown in Figure 6. Note that despite the large number of injections performed within this image slice, there are sizable regions of tissue that show no contrast enhancement. However, the results of the last three injections, shown in Figure 7, are significantly different. Despite the low number of injections, almost all of the tissue within the image slice shows enhancement.

GADOLINIUM PREINJECTIONS

In the second canine, the utility of performing gadolinium solution preinjections, before the therapeutic agent is injected, was examined. Injections at two sites within the canine prostate are demonstrated. Following accurate placement of the needle at the first target site (Figure 8A), the gadolinium solution was injected. At this site, gadolinium tracks to the urethra, showing that subsequent ethanol injection may injure this tissue (Figure 8B). No ethanol was injected and the tissue was spared. Therefore, no tissue damage, only minor bleeding at the needle track, was seen on gross pathology (Figure 8C). At the second injection site, the needle was accurately placed (Figure 8D) and gadolinium injected. The gadolinium stayed more localized within the prostate tissue and away from the urethra (Figure 8E). This injection site was deemed safe and subsequently, 0.2 ml of ethanol was injected. The region of tissue damage, as seen on

gross pathology (Figure 8F), correlates well with the distribution of gadolinium on the T1-weighted images.

MR VS HISTOLOGY CORRELATION FOR HUMAN PROSTATE INJECTIONS

A 0.018 inch diameter needle made from nitinol hypotubing was placed in the right posterior lobe of an excised human cadaveric prostate and a volume of T1-weighted gradient echo images were collected (Figure 9, first column). Following injection of 0.3 ml of Trypan blue tissue dye mixed with 30 mM Gd-DTPA, a second set of axial T1-weighted images was acquired, allowing for clear visualization of the injected solution (Figure 9, second column). Tissue sections corresponding to the imaged planes are shown in Figure 9, third column. Note that there is good agreement between the injectant dispersion patterns as seen on MR images with the histology pictures taken afterwards. This is evidence that MR guided injections can in fact be used as an accurate method of visualizing injectant dispersions.

LEAKAGE IN THE HUMAN PROSTATE

There was a correlation found between the injection site and the probability of leakage. Leakage is defined as contrast enhancement seen on MR in the urethra or beyond the prostatic capsule (see Fig. 5). Figure 10 shows a breakdown of the injections that leaked. A couple of observations arose from this data: 1) peripheral zone injections are more likely to leak via the urethra than central gland injections; and 2) central gland injections are more likely to show leakage through the prostatic capsule. Overall, 100% of peripheral zone injections showed some form of leakage, whereas only 50% of the central gland targets showed leakage. Note that the distance between peripheral zone

(PZ) and central gland (CG) and leakage points (urethra or capsule) shows somewhat surprising results. The PZ-urethral distance was statistically higher than the PZ-capsule distance, yet in spite of this PZ-urethral leaks were much more common. On the other hand, CG-capsule distances averaged less than CG-urethral distances, and capsular leaks were found to be more common. This suggests that bulk flow in the PZ tends to be of a vector type nature that dominates in one direction along the ducts. One possible explanation for this phenomenon is based on the anatomical structure of the duct coverage in the PZ. As the ducts converge at the urethra, they become larger, and thus can facilitate higher bulk flow in that direction. This may create a tissue/fluid pressure gradient that encourages flow in the direction of the urethra and away from the capsule and central gland.

HUMAN VS CANINE PROSTATE

Although the canine prostate is a widely used model of the human prostate, injection experiments reveal differences in tissue structure that affect liquid distribution within the prostate.

From an axial perspective, the canine prostate has a wedge shaped pattern of glandular units separated by connective tissue, similar in structure to an orange. The human prostate has a more complex structure, comprised of a central gland and peripheral zone. There are major ducts running posteriorly and medially to the urethra from the central gland, but the wedge shape found in the canine prostate instead assumes a more curved boundary in the human gland. In general, the canine prostate is symmetric with respect to the anterior/posterior axis, whereas, the human prostate is not. Therefore, injecting at the anterior part of a given axial plane can be expected to show a different

drug distribution from the posterior part of the same axial plane in human prostates, but in canine prostates the distribution will be similar. Fig. 11A shows an anterior injection pattern, and Fig. 11B/C show posterior injection patterns in human prostates. Note that Fig. 11D shows several almost identical looking wedge shaped patterns from multiple injections in the canine prostate. In the canine model injecting into the anterior or posterior portion of the gland gives the same distribution, whereas for human prostates there is no symmetry in this axis and therefore injecting in the anterior portion of the gland gives a different distribution than the posterior portion.

REALTIME HUMAN PROSTATE INJECTION IMAGES

Using the realtime MR sequence described in the methods section, a "movie" comprised of 1 second snapshots of the injection was captured. Figure 12 shows a T2 baseline image and several snapshots after the injection at varying time intervals. From this set of images, the contrast can be seen accumulating at the needle tip and then gradually flowing around the periphery of the central gland near the capsule towards the peripheral zone. The T2 weighted image shows good contrast between the central gland and peripheral zone as a guide to distinguishing these two different anatomical areas. Note that coverage in the central gland proper is poor, and that most of the enhancement is seen in the capsular area, progressing towards the peripheral zone. This was a consistent theme in our experiments; a central gland target only partially covers the central gland and most of the agent flows to the peripheral zone.

DIFFUSION WEIGHTED IMAGING AND INJECTION CORRELATION

Using the multiple spin echo T2 diffusion weighted sequence described in the methods section, we can acquire a diffusion weighted map of the axial plane of the prostate. Figure 12B shows the sum of the apparent diffusion coefficient (ADC) and the exponentially weighted ADC as a combination image. Note the striking similarity between the tissue structure shown in the baseline T2 image (Fig 12A) and the diffusion data seen in the diffusion image (Fig. 12B). As shown in the realtime data in Fig. 12, the injectant tends to distribute according to local tissue structure, and this tissue structure has a correlation with the diffusion weighted data.

DISTRIBUTION PLANES IN THE HUMAN PROSTATE

In contrast to the canine prostate, the human prostate is asymmetric with respect to the anterior/posterior and superior/inferior axes. To get a better understanding of how drug distribution may differ in these planes, we acquired images of all 3 major planes after each injection. In the first set of experiments in which both flow rate and total volume injected were held constant, the dispersion of contrast relative to the 3 major axes was measured and is shown in Fig 13. Note that for constant flow rate and volume, the dispersion amongst the axes showed little variation. For the second set of experiments in which volume was increased by 100% with a fixed flow rate, the average dispersion in the axial plane was relatively unchanged, however the dispersion along the longitudinal axis (superior to inferior direction) was increased substantially. This further demonstrates the lack of correlation between axial plane coverage and total volume injected (compare figures 6 and 7). In the third set of experiments with varying flow

rates and fixed total volume, the dispersion data were not statistically different (save for a slight statistically significant variance in the anterior/posterior distribution, see Fig. 14), although it is noteworthy that the coverage was actually reduced in the increased flow rate.

FIXED VS FRESH HUMAN PROSTATE INJECTIONS

All injections into the fixed prostate required significantly higher pressure to infuse the tissue, in fact the pressure required was so large that it fell outside the injector range of allowable fluid pressures. Therefore, we had to deliver the injections by hand. The flow rate was timed to be kept as close as possible to 0.1 mL/sec.

All 3 injections showed very poor tissue coverage compared to the fresh prostates. Contrast enhancement was limited to a vector-like pattern directly into the urethra. Chemical fixation causes greatly increased tissue pressure, which would explain the very limited tissue distribution and higher fluid pressures required to infiltrate the gland.

DISCUSSION

Intraprostatic injections, using dehydrated ethanol, are currently being investigated as a minimally invasive treatment for benign prostatic hypertrophy (BPH) ~~(17)~~ [21], which has a prevalence of 50% in men over fifty~~50~~ and greater than 80% in men over eighty~~80~~ [~~(18)~~22]. When injected into the prostate, ethanol induces cell lysis and coagulation necrosis of arteries and veins, resulting in tissue necrosis and subsequent shrinkage of the prostate (reducing the obstructive symptoms caused by BPH). Others have hypothesized that alcohol injections reduce BPH symptoms by abolishing prostate

constriction (due to destruction of α-adrenergic receptors in the tissue)~~(19)~~ [23]. However, side effects that have plagued this treatment are inadvertent damage to the external urethral sphincter, which is important for urinary continence, and stricture of the urethra~~(20)~~ [24]. This damage is caused by leakage of injected ethanol into the urethra and periurethral tissue, which then damages the endothelium and muscular sphincter, resulting in stricture and/or incontinence. In light of the results seen in this paper, the frequent side effects following intraprostatic ethanol injections are not surprising. When performing transrectal intraprostatic injections, we observed significant leakage of contrast solution in eight out of eleven cases in the canine model. A simplistic model in which the injected agent stays localized at the needle tip is insufficient.

MRI may be useful for improving the efficacy and safety of these injections. First, through the use of realtime projection imaging (Figures 2-5), it is possible to determine *during the injection* whether the agent is staying localized at the target or rather, if it is leaking into surrounding tissue. Therefore, failed injections could be stopped early, conserving drug and preventing damage to surrounding tissues. When a gadolinium preinjection is delivered before the drug, this approach allows for immediate determination of whether the injection site is safe and therefore, whether the therapeutic agent should be subsequently injected. Second, if more precise visualization of the injected agent is desired, T1-weighted images can be collected to visualize the three-dimensional distribution of the injected solution within the tissue (Figures 6-9).

Clearly, intraprostratic injections performed without direct imaging confirmation may not actually deliver the therapeutic agent to a desired target. Given the limited number of injections performed in this study, it is difficult to suggest a definitive solution

to this problem. Nevertheless, several important mechanisms can be hypothesized based on these preliminary results.

First, injection velocity may play an important role in determining the distribution of injected solutions. Fast injection through the 18 G needle (Figure 4) and the hypotubing needles (Figure 5 and 8) did not suffer from 'back-leakage' along the needle track. However, another fast injection through the 18G needle (0.3ml in 5 seconds) similar to Figure 5, did show some back-leakage along the needle (results not shown). In these cases, the velocity with which the solution exits the needle is high (velocity is higher when using the hypotubing needle because of its small cross-sectional area). The resulting forward momentum may help to force the solution into the tissue, resisting capillary forces which would draw the liquid out along the needle path. While this mechanism seems plausible, high injection rates in the liver have been shown to increase leakage rates ~~(14)~~ [25].

Second, while high injection velocity appears to reduce back-leakage, it is also correlated with increased leakage through the internal structures of the prostate (as in Figures 5 and 8B, where solution tracked along the urethra). If the solution is forced into the tissue, it will follow a low resistance path which, in the prostate, leads to the urethra (the ductal structure of the canine prostate and of the human central prostate is directed toward the intraprostatic urethra). This is concerning in that high concentrations of a drug, such as injected ethanol, may cause damage to the urethra and associated sphincters and therefore lead to either stricture or incontinence.

Third, as already alluded to, the underlying tissue structure has a very significant impact on the distribution of an injected liquid agent. This effect is evident in the canine

prostate, which has a septated wedge-like structure (similar to an orange cut in cross-section). In Figures 6 and 7, this structure is clear after contrast injection. Similarly, the injections performed in the excised cadaveric prostates follows the tissue structure of the human prostate. For example, in Figure 9, contrast tracks along the course of secretary ducts within the peripheral gland, which flow toward the midline of the gland and the urethra ~~(21)~~ [26].

Other factors which are likely to be important include the viscosity of the injected solution (highly viscous solutions flow, and therefore leak, less easily), the size of the injection needle (independent from injection velocity, smaller needles may reduce damage to the tissue structure and therefore reduce leakage), and the volume of injected solution (smaller volume injections will result in lower pressures and therefore, reduced leakage flow). Further work is warranted to clarify the relative important of each of these factors.

To help predict the tissue distribution of a therapeutic agent, a contrast pre-injection strategy has been proposed and demonstrated (Figure 8). While this technique appears attractive, it relies on important assumptions. First, the distribution pattern of the therapeutic agent must be similar to that of the pre-injection; otherwise, the pre-injection will not yield useful information. In the example using ethanol presented here, it appears that the injected ethanol has a more restricted tissue distribution than the 30 mM Gd-DTPA solution (compare Figures 8E and 8F). Therefore, just because the Gd-DTPA solution tracked to the urethra in the first injection (Figure 8B), we can not be sure that the ethanol would have gone there also. Unequal distribution will likely be a problem for many agents, unless the pre-injected agent can match the molecular size and chemical

characteristics of the therapeutic solution. However, as the initial distribution pattern appears to be determined largely by bulk fluid flow, matching characteristics such as viscosity may be sufficient.

A more comprehensive prostate injection protocol can be based upon the data in Fig. 14. Overall, bulk flow in the central gland is reduced compared to the peripheral zone, which has a good correlation with DWI data. This suggests that therapeutic targets in the central gland may require multiple injection sites and/or a larger total volume injected. Note that Fig. 11B, C shows that a peripheral zone injection to one side of the prostate can result in coverage of both peripheral zone lobes. For central gland injections this is rare. This suggests that bilateral coverage of peripheral zone targets may be achieved with a unilateral injection site, whereas bilateral CG coverage probably requires bilateral injection sites. This makes sense, considering the anatomy of the prostate. The central gland is composed of an array of widely divergent acini and small ducts that have a much more random structure than the peripheral zone. The PZ has a much more organized structure with large ducts that converge from the seminal vesicles and the CG to the urethra. It is noted that larger total volume injected has relatively little effect on axial plane dispersion but does have a sizable impact on longitudinal (coronal and sagittal plane) dispersion.

The leakage data in Fig. 10 show that peripheral zone injections have an extremely high probability of urethral leakage. In fact, every single injection in the peripheral zone showed some urethral leak. Depending on the particular clinical application this can be acceptable or not. For example, in ethanol ablation therapy, leakage in the urethra would be highly undesirable, due to possible damage at the urethral

sphincter. On the other hand, in the case of an adenovirus vector used for prostate cancer treatment, urethral leakage is not nearly as troublesome. The nerve plexus that controls erectile function is located outside the prostatic capsule, and some drug agents, such as certain chemotherapeutics, may harm these nerves; under this scenario minimizing capsular leakage may take precedence over urethral leakage. Capsular leakage was found to be not as common as urethral leakage, although the central gland targets do face a higher probability of capsular leak. These observations suggest that if avoiding urethral leak is a primary goal, then peripheral zone injections should be avoided, whereas if the clinician is more concerned with capsular leaks and can afford to risk urethral leakages, then the peripheral zone is an optimal injection target.

Another interesting observation regarding central zone ~~vs~~vs. peripheral zone injections is that a sufficiently large volume delivered to the central gland can in some cases penetrate a good portion of the ipsilateral peripheral zone, whereas larger volumes delivered to the peripheral zone rarely cover the central gland and the excess volume tends to either leak out the urethra or flow to the bilateral peripheral zone via the major ducts that converge with the urethra at the verumontanum and at distributed sites in the periurethral region. See Figures 9 and 11 for examples of peripheral zone and central gland distributions. Fig. 9 is a central gland injection, whereas Figure 11B shows a peripheral zone injection. More work needs to be done to have sufficient statistical certainty of this phenomenon, but if this holds up to further scrutiny it could be extremely valuable as an injection planning tool.

The present results showed only limited success in reliably covering large regions of tissue with a small number of injections. Our limited data suggest that total volume

injected has a poor correlation with tissue coverage. Indeed, the canine prostate experiments showed greater coverage when less total volume was injected and more total injection sites were used. Further work needs to be done to elucidate whether or not this is a consistent phenomenon. While global enhancement was achieved in Figure 7, it is important to note that this enhancement was limited to the 3mm-thick slice shown (some enhancement of the neighboring slices was also seen). To cover the entire prostate, better strategies – such as needles with multiple tips or side ports – may be necessary.

Finally, one key finding to future research methodology in this area is that human prostates fixed with formalin give profoundly different injection patterns than fresh prostates. Since fresh prostates stored in isosaline solution are assumed to be a better model of in-vivo prostate injections, it is important that all ex-vivo modeling be done on fresh, not fixed specimens. It is important to note that fresh ex-vivo prostate injections may differ from in-vivo experiments, due to many variables such as altered tissue compliance, perfusion due to active blood flow, and active physiological parameters. Despite the limitations of ex-vivo work, we believe this is a fundamental step on the road to in-vivo testing. More work is planned in the future with in-vivo studies to determine if injection patterns remain similar.

CONCLUSION

Although prostate injections are a desirable minimally invasive procedure for some pathologies, this modality is still under utilized due to failure modes that can lead to complications, as well as uncertainty regarding optimal injection techniques. This paper attempts to address some of these issues using the advantages of MR imaging that elude traditional TRUS (transrectal ultrasound) imaging, such as excellent soft tissue contrast. Leakage modes were demonstrated, including capsular back leakage along the needle path and urethral leakage for peripheral zone targets. Drug agent distribution was analyzed in 3 anatomical planes, and a preliminary guide to injection planning was developed based on that data. Dynamic imaging during the injection as well as T1-weighted imaging after the injection allows for monitoring of the solution's distribution within and around the prostate. Primarily, we have found that intraprostatic injections often follow a complex distribution within and around the prostate; leakage both within and around the prostate was common. MR visualization of injected agents may allow for prediction and monitoring of drug distributions, improving efficacy and reducing treatment side effects. One strategy for predicting drug distribution patterns, the use of a contrast pre-injection, was suggested and demonstrated. Taking into account the unique properties of the central gland and the peripheral zone, as well as the prostate structure as a whole, can serve as a preliminary guide to planning prostate injections. Further studies, taking advantage of the ability of MRI to reveal tissue micro- and super-structure, may allow for improved prediction of drug distribution and therefore, optimization of therapeutic agent delivery.

REFERENCES

1. Livraghi, T., Festi, D., Monti, F., Salmi, A. and Velotti, C.: Ultrasound-guided percutaneous alcohol injection of small hepatic and abdominal tumors. Radiology, 161: 309, 1986.
2. Fujimoto, T.: The experimental and clinical studies of percutaneous ethanol injection therapy (PEIT) under ultrasonography for small hepatocellular carcinoma. Acta Hepatolog. Jap., 29: 52, 1988.
3. Solbiati, L., Giangrande, A., De Pra, L., Belloti, E., Cantu, P. and Ravetto, C.: Percutaneous ethanol injection of parathyroid tumors under US guidance: treatment for secondary hyperparathyroidism. Radiology, 155: 607, 1985.
4. Takeda, S., Michigishi, T. and Takazakura, E.: Successful ultrasonically guided percutaneous ethanol injection for secondary hyperparathyroidism. Nephron, 62: 100, 1992.
5. Goya N, Ishikawa N, Ito F, Kobayashi C, Tomizawa Y, Toma H. Transurethral Ethanol Injection Therapy for Prostatic Hyperplasia: 3 Year Results. J Urol 2004; 172: 1017-1020.
6. Susil RC, Krieger A, Derbyshire JA, Tanacs A, Whitcomb LL, Fichtinger G, Atalar E. System for MR image-guided prostate interventions: canine study. Radiology 2003;228(3):886-894.
7. Plante MK, Gross AL, Kliment J, Kida M, Zvara, P. Intraprostatic ethanol chemoablation via transurethral and transperineal injection. British Journal of Urology 2003; 91: 94-8.
8. Nelson PS. Identifying immunotherapeutic targets for prostate carcinoma through the analysis of gene expression profiles. Ann N Y Acad Sci 2002;975:232-46.
9. DeWeese TL, van der Poel H, Li S, Mikhak B, Drew R, Goemann M, Hamper U, DeJong R, Detorie N, Rodriguez R ~~and others~~ et al. A phase I trial of CV706, a replication-competent, PSA selective oncolytic adenovirus, for the treatment of locally recurrent prostate cancer following radiation therapy. Cancer Res 2001;61(20):7464-72.
10. Nemunaitis J. Selective replicating viral vectors : potential for use in cancer gene therapy. BioDrugs 2003;17(4):251-62.
11. Mercatante DR, Mohler JL, Kole R. Cellular response to an antisense-mediated shift of Bcl-x pre-mRNA splicing and antineoplastic agents. J Biol Chem 2002;277(51):49374-82.
12. Trudel S, Trachtenberg J, Toi A, Sweet J, Hua Li Z, Jewett M, Tshilias J, Zhuang LH, Hitt M, Wan Y and others. A phase I trial of adenovector-mediated delivery of interleukin-2 (AdIL-2) in high-risk localized prostate cancer. Cancer Gene Ther 2003;10(10):755-63.
13. Li S, Simons J, Detorie N, O'Rourke B, Hamper U, DeWeese TL. Dosimetric and technical considerations for interstitial adenoviral gene therapy as applied to prostate cancer. Int J Radiat Oncol Biol Phys 2003;55(1):204-14.

14. Bhutani MS. Endoscopic ultrasound guided antitumor therapy. Endoscopy 2003;35(8):S54-6.
15. Dudouet P, Portalez D, Lhez JM, Elman B, Larroque JM, Bachaud JM, Redon A, Ribot JF. Trans-rectal ultrasonography (TRUS) with lipiodol injection for localization of the prostatic apex before radiotherapy planning. Radiother Oncol 2001;61(2):135-41.
16. Rauh G, Pieczek A, Irwin W, Schainfeld R, Isner JM. In vivo analysis of intramuscular gene transfer in human subjects studied by on-line ultrasound imaging. Hum Gene Ther 2001;12(12):1543-9.
17. Yu KK, Hricak H. Imaging prostate cancer. Radiol Clin North Am 2000;38(1):59-85, viii.
18. Savoca G, De Stefani S, Gattucio I, Paolinelli D, Stacul F, Belgrano, E. Percutaneous Ethanol Injection of the Prostate as Minimally Invasive Treatment for Benign Prostatic Hyperplasia: Preliminary Report. Eur Urol 201; 40:504-8.
19. Derbyshire JA, Wright GA, Henkelman RM, Hinks RS. Dynamic scan-plane tracking using MR position monitoring. J Magn Reson Imaging 1998;8(4):924-32.
20. Dumoulin CL, Souza SP, Darrow RD. Real-time position monitoring of invasive devices using magnetic resonance. Magn Reson Med 1993;29(3):411-5.
21. Ditrolio J, Patel P, Watson RA, Irwin RJ. Chemo-ablation of the prostate with dehydrated alcohol for the treatment of prostatic obstruction. J Urol 2002;167(5):2100-3; discussion 2103-4.
22. McConnell JD. Benign Prostatic Hyperplasia: Diagnosis and Treatment (Clinical Practice Guideline). Rockville, MD: Agency for Health Care Policy and Research, Public Health Service, U.S. Department of Health and Human Services; 1994. Report nr AHCPR 94–0582.
23. Zlotta AR, Raviv G, Peny MO, Noel JC, Haot J, Schulman CC. Possible mechanisms of action of transurethral needle ablation of the prostate on benign prostatic hyperplasia symptoms: a neurohistochemical study. J Urol 1997;157(3):894-9.
24. Littrup PJ, Lee F, Borlaza GS, Sacknoff EJ, Torp-Pedersen S, Gray JM. Percutaneous ablation of canine prostate using transrectal ultrasound guidance. Absolute ethanol and Nd:YAG laser. Invest Radiol 1988;23(10):734-9.
25. Alexander AL, Barrette TR, Unger EC. Magnetic resonance guidance of percutaneous ethanol injection in liver. Acad Radiol 1996;3(1):18-25.
26. Walsh PC, editor. Campbell's Urology. Philadelphia: W.B. Saunders; 2002.

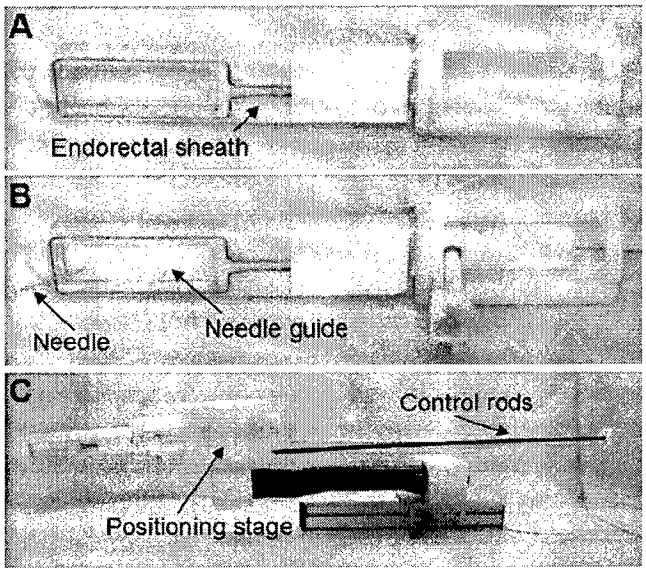

Figure 1 Transrectal needle placement device. **Panel A**: A stationary endorectal sheath, with an integrated imaging coil, provides a stable access route to the prostate. **Panel B**: A cylindrical needle guide, including a curved needle channel and 3 microcoil fiducials, allows for needle access to the prostate through the anterior wall of the rectum. **Panel C**: The sheath and needle guide are fixed to the positioning stage, which allows for rotation and translation of the needle guide (via two concentric control rods) from outside of the scanner bore.

254x190mm (96 x 96 DPI)

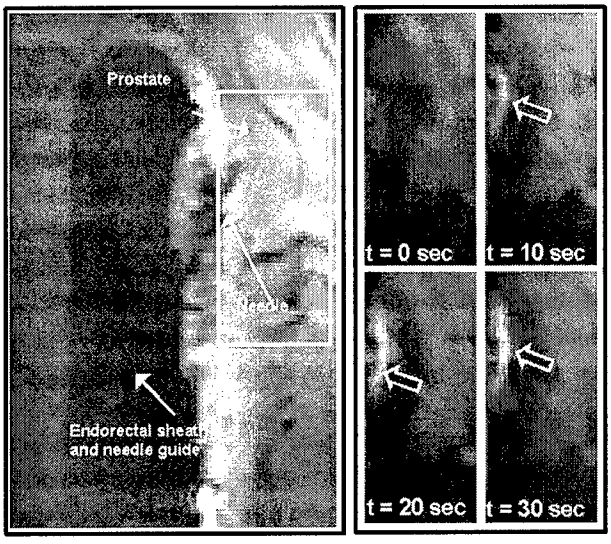

Figure 2 Injected contrast solution accumulating at the prostate-rectum interface. The white box in the sagittal scout image (left panel) shows the location of the time-series images (four right panels). 0.3 ml of 30 mM Gd-DTPA in normal saline was injected over 30 seconds through the 18G canula. The solution can be seen tracking superiorly along the prostate-rectum interface (open arrows).

254x190mm (96 x 96 DPI)

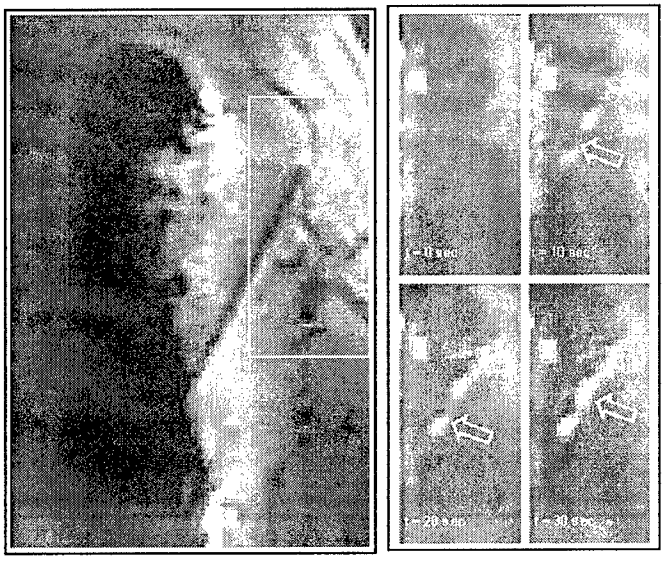

Figure 3 Injected contrast solution tracking along the needle path. 0.3 ml of 30 mM Gd-DTPA solution was injected over 30 seconds through the 18G canula. The majority of the solution is visible along the needle path (open arrows), rather than at the needle tip.

254x190mm (96 x 96 DPI)

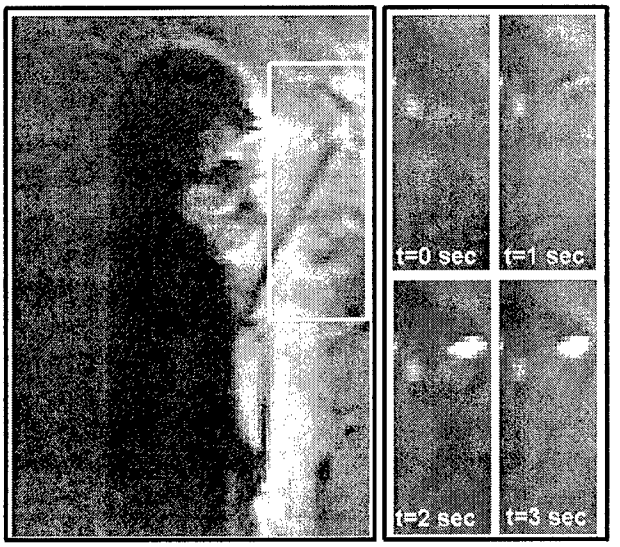

Figure 4 Injected contrast solution accumulating at the needle tip. 0.3 ml of 30 mM Gd-DTPA solution was injected over 5 seconds through the 18G canula. The solution is visible as a single bolus at the needle tip (open arrows).

254x190mm (96 x 96 DPI)

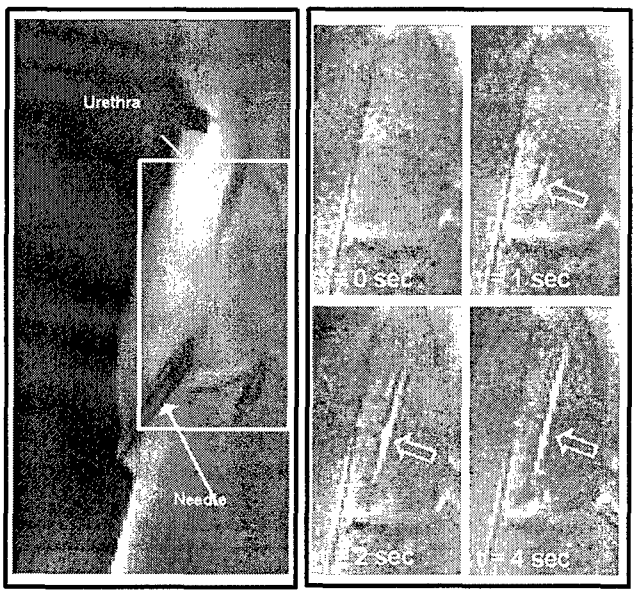

Figure 5 Injected contrast solution tracking along the intraprostatic urethra. 0.3 ml of the Gd-DTPA solution was injected over 5 seconds through the 0.018 inch diameter nitinol needle. Rather than accumulating at the needle tip, the solution tracks up the intraprostatic urethra (open arrows).

254x190mm (96 x 96 DPI)

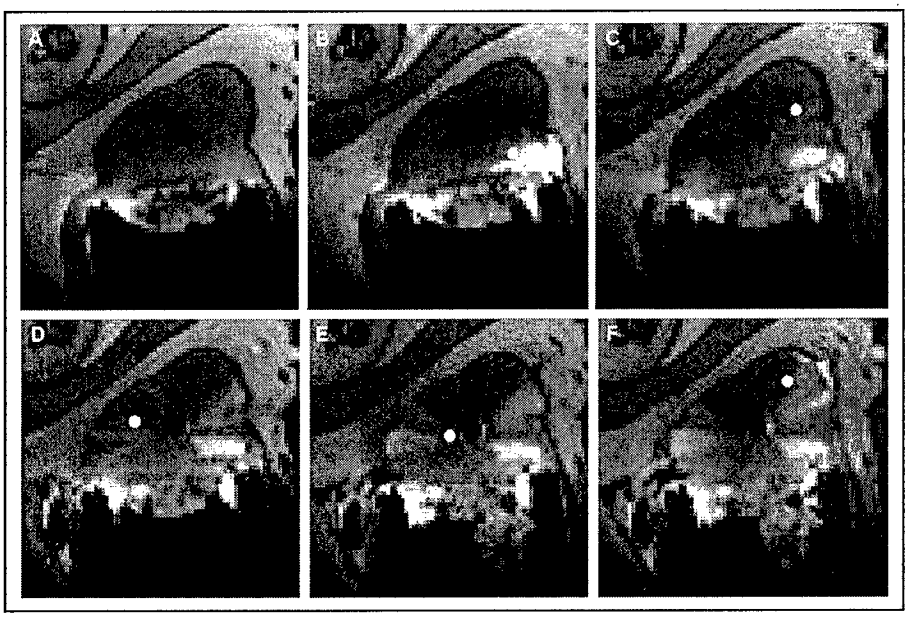

Figure 6 Incomplete tissue enhancement. Five contrast boluses (all 0.3 ml except for the fourth, which was 0.6 ml) were injected over 30 seconds (60 seconds for the fourth bolus). Injection sites are indicated by the white circles. Despite the large number of injections, a majority of the tissue in this image plane is not enhanced.

254x190mm (96 x 96 DPI)

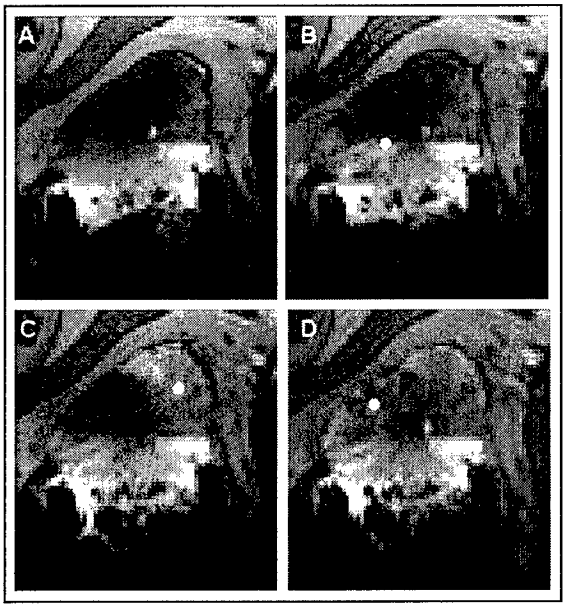

Figure 7 Complete tissue enhancement. Three boluses of Gd-DTPA solution (0.15, 0.3, and 0.3 ml respectively) were injected over 5 seconds each. Despite the low number of injections, strong enhancement of the whole tissue plane is achieved.

254x190mm (96 x 96 DPI)

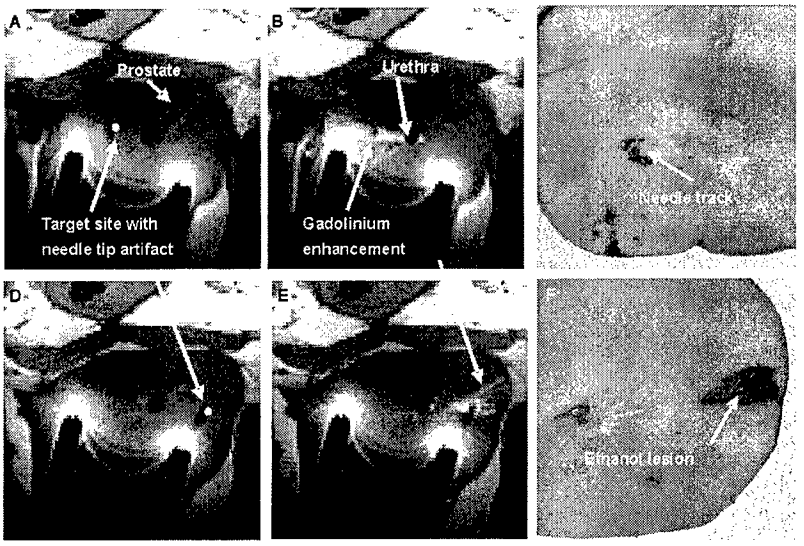

Figure 8 Gd-DTPA preinjections can be used to predict drug distribution patterns. Panel A: The injection needle was accurately placed at the first injection site. Panel B: Gadolinium solution injected at this site tracked to the urethra. Therefore, no ethanol was injected here. Panel C: No tissue necrosis is visible on gross pathology (only minor bleeding at the needle tip site). Panel D: The injection needle was accurately placed at the second injection site. Panel E: Gadolinium solution injected here stayed localized. Therefore, 0.2 ml of ethanol was injected. Panel F: Tissue necrosis is visible on gross pathology and correlates well with the gadolinium injection pattern.

254x190mm (96 x 96 DPI)

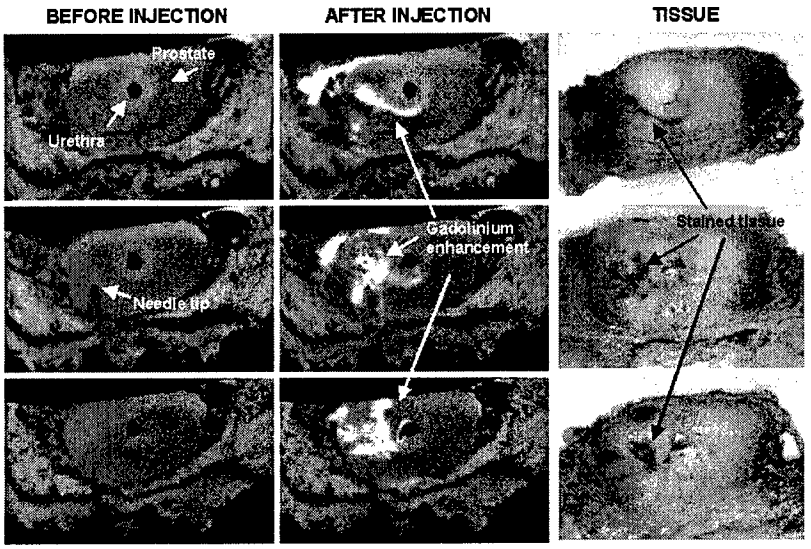

Figure 9 Intraprostatic injection in an excised cadaveric human prostate. **First column:** A 0.018 inch diameter nitinol injection needle was placed by hand in the peripheral zone of the prostate and T1-weighted gradient echo images acquired. **Second column:** Following injection of 0.3 ml of 30 mM Gd-DTPA mixed with Trypan blue tissue dye (over 30 seconds), a second set of T1-weighted gradient echo images were acquired. Enhancement due to the gadolinium solution is clearly visible. **Third column**: Blue stained tissue, seen in gross tissue sections of the prostate, corresponds well with the enhancement seen in MR-images.

254x190mm (96 x 96 DPI)

	PZ injections		
	Urethral Distance (mm)	*Capsule Distance (mm)*	*Leakage Type*
#1	8	8	Urethral
#2	10	8	Both
#3	14	8	Urethral
#4	11	5	Urethral
	CG injections		
#1	4	6	Urethral
#2	13	6	Capsule
#3	19	6	Capsule
	Average Distances (mm)		
PZ to urethra	10.75 +/- 1.5		
PZ to capsule	7.25 +/- 0.9		
CG to urethra	12 +/- 4,7		
CG to capsule	6 +/- 0		

Figure 10 Leakage Modes for Peripheral Zone (PZ) and Central Gland (CG) injection sites. Average distances are given with 95% confidence limits.

254x190mm (96 x 96 DPI)

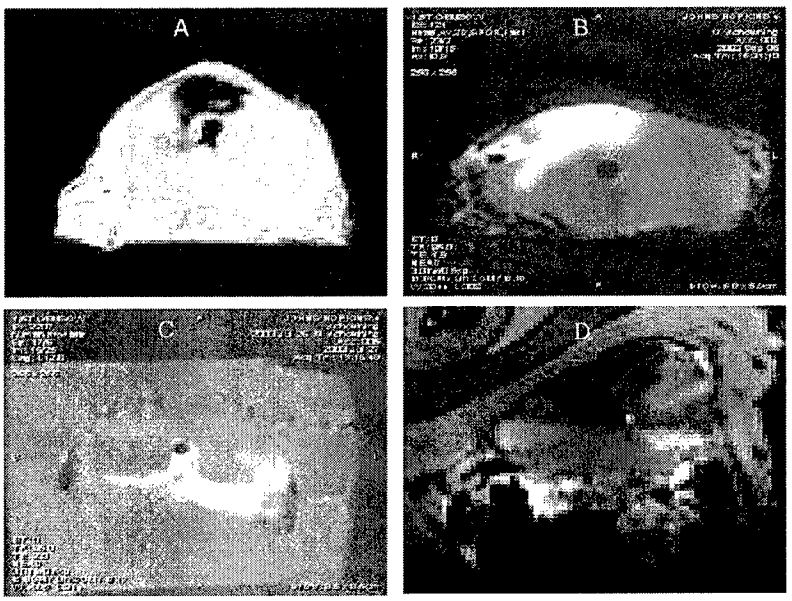

Figure 11 Axial views of human (A,B,C) and canine (D) prostate injections. Note that multiple prostate injections in the canine show the same pattern, whereas each human prostate injection has a different pattern. Panel A is a T2 weighted image (contrast is dark, whereas all other images are T1 weighted

254x190mm (96 x 96 DPI)

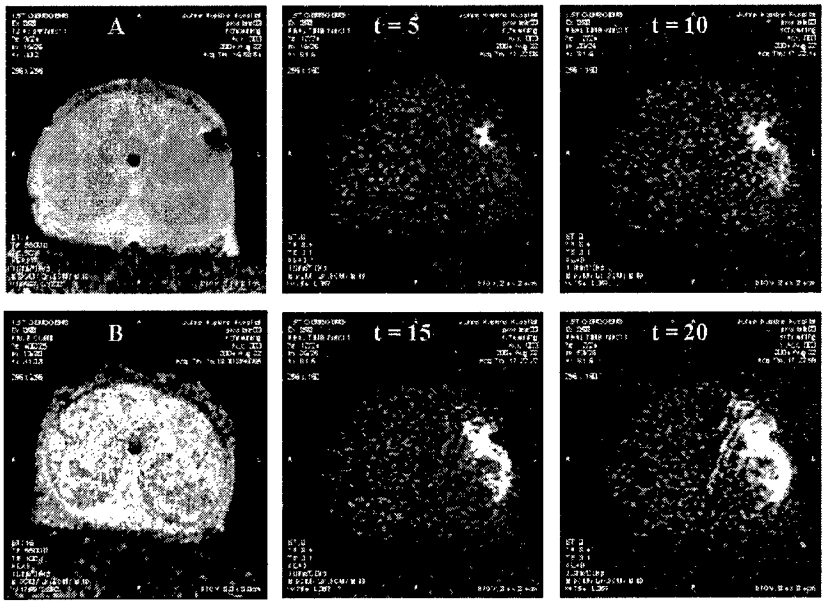

Figure 12 T2, DWI, and Realtime Injection Images for a Central Gland Target. T2 baseline image (A), T2 diffusion weighted image (B) and T1 realtime axial injection images (times are in seconds).

254x190mm (96 x 96 DPI)

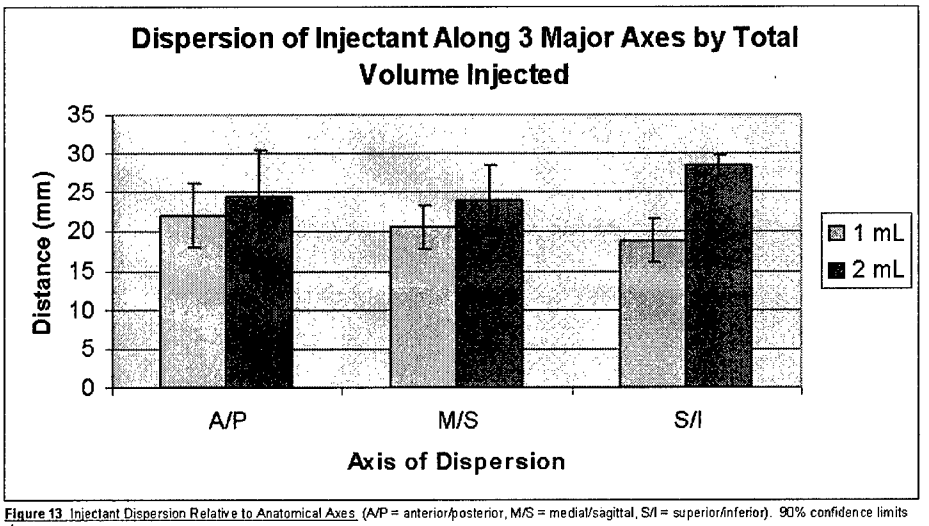

Figure 13 Injectant Dispersion Relative to Anatomical Axes. (A/P = anterior/posterior, M/S = medial/sagittal, S/I = superior/inferior). 90% confidence limits shown.

254x190mm (96 x 96 DPI)

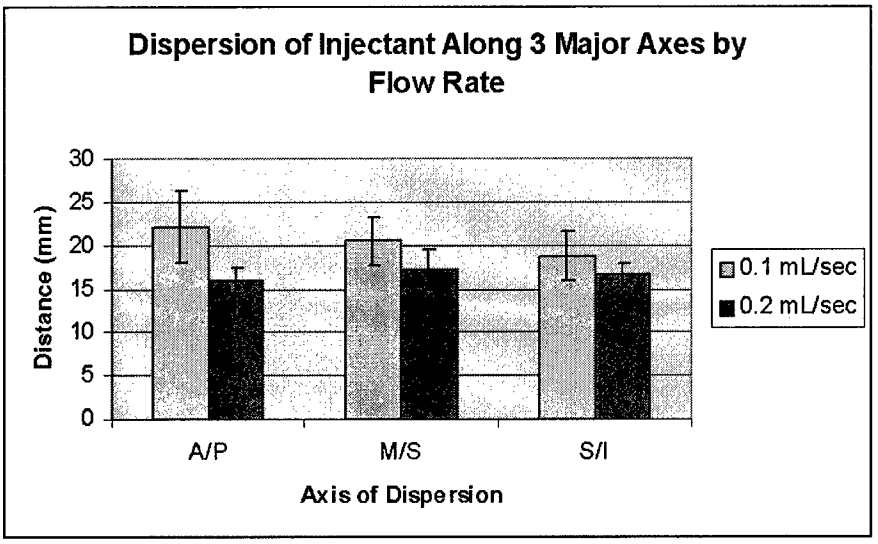

Figure 14 Injectant Dispersion Relative to Flow Rate. (A/P = anterior/posterior, M/S = medial sagittal, S/I = superior/inferior). 90% confidence limits shown

254x190mm (96 x 96 DPI)

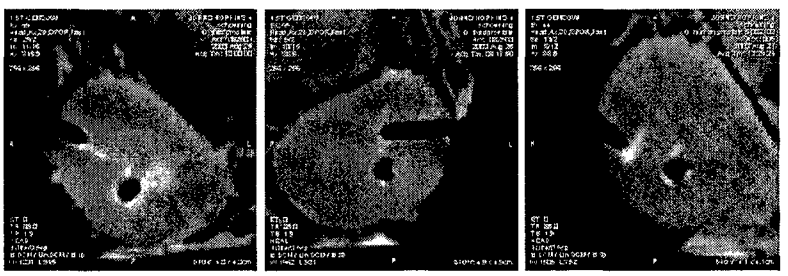

Figure 15 Poor injectant coverage in three formalin-fixed human prostate injections

254x190mm (96 x 96 DPI)

An Interventional MRI Technique for the Molecular Characterization of Heterogeneous Intra-Prostatic Dynamic Contrast Enhancement

Cynthia Ménard M.D. [1,2], Robert C. Susil Ph.D. [3], Peter Choyke M.D. [4], Jonathan Coleman MD[5], Robert Grubb M.D. [5] Ahmed Gharib M.D. [4] Axel Krieger M.S. [6] Peter Guion M.S.[1], David Thomasson Ph.D. [4] Karen Ullman R.T.T. [1], Sandeep Gupta [7] Virginia Espina M.S. [8]Lance Liotta M.D. [8] Emanuel Petricoin Ph.D. [9], Gabor Fitchtinger Ph.D. [6], Louis L. Whitcomb Ph.D. [6], Ergin Atalar Ph.D. [3], C. Norman Coleman M.D. [1], Kevin Camphausen M.D. [1]

[1]Radiation Oncology Branch, National Cancer Institute, NIH-DHHS
Bldg 10, Rm B3B69, 9000 Rockville Pike, Bethesda, MD, 20892

[2]Department of Radiation Oncology, Princess Margeret Hospital, University of Toronto, 610 University Ave, Toronto, ON, M5G 2M9, Canada

[3]Department of Biomedical Engineering, Johns Hopkins University School of Medicine, 720 Rutland Ave., Baltimore, Maryland, 21205

[4]Diagnostic Radiology Department, Clinical Center, NIH-DHHS
Bldg 10, Rm1C660, 9000 Rockville Pike, Bethesda, MD, 20892

[5]Urologic Oncology Branch, National Cancer Institute, NIH-DHHS
Bldg 10, Rm 2B47, 9000 Rockville Pike, Bethesda, MD, 20892

[6]Department of Mechanical Engineering, Johns Hopkins University School of Medicine, 123 Latrobe Hall, 3400 North Charles Street, Baltimore, MD, 21218-2681

[7]GE Medical Systems, USA

[8]FDA-NCI Clinical Proteomics Program, Laboratory of Pathology, Center for Cancer Research, National Cancer Institute, NIH-DHHS, Bldg 10, RmB1B53, 9000 Rockville Pike, Bethesda, MD, 20892

[9]FDA-NCI Clinical Proteomics Program, Office of Cellular and Gene Therapy Center for Biologics Evaluation and Research, Food and Drug Administration, 8800 Rockville Pike, Bldg 29A Room 2D12, Bethesda, MD, 20892

Submitted as a Brief Report to Molecular Imaging, October 13 2004

Corresponding author:
Cynthia Ménard
Department of Radiation Oncology, Princess Margaret Hospital
610 University Ave, Toronto, ON, M5G 2M9 Canada
Cynthia.Menard@rmp.uhn.on.ca
Phone: 416-946-2936 Fax: 416-946-2227

Key Words: angiogenesis, molecular imaging, interventional MRI, prostate cancer, microarray analysis

Sources of funding: Robert Susil was supported by an NIH MSTP fellowship. Supported in part by the following grants: NIH R01 EB002963, NSF EEC 9731478. U.S, Army Prostate Cancer Research Program Award DAMD17-01-1-0064, NSF ERC 9731478, and an NSF ERC PER grant.

Originality of the work: This work has not been previously published. It has been presented in part at the ISMRM annual meeting in Kyoto, Japan, May 2004, and at the Interventional MRI Symposium in Boston, MA October 2004.

Abstract

The biological characterization of an individual patient's tumor by non-invasive imaging will have an important role in cancer care and clinical research if the molecular processes that underlie the image data are known. Spatial heterogeneity in the dynamics of MRI contrast enhancement (DCE-MRI) is hypothesized to reflect variations in tumor angiogenesis. Here we demonstrate the feasibility of precisely co-localizing DCE-MRI data with the genomic and proteomic profiles of underlying biopsy tissue using a novel MRI-guided biopsy technique in a patient with prostate cancer.

Abbreviations:

DCE-MRI – Dynamic Contrast Enhanced Magnetic Resonance Imaging

GKM – General Kinetic Model

MR – Magnetic Resonance

MRI – Magnetic Resonance Imaging

ROI – Region of Interest

Introduction

Dynamic contrast-enhanced magnetic resonance imaging (DCE-MRI) provides a visual representation of both the anatomy and microvascular biology of cancer by measuring temporal changes in MR signal intensity associated with the intravascular injection of a contrast agent. (1) Spatial heterogeneity in the kinetics of contrast transit is thought to reflect variations in tissue perfusion and microvascular permeability.(2) Angiogenic microvessels, important for the growth and survival of cancer cells, are characterized in part by larger endothelial cell gaps resulting in greater permeability to small molecules.(3) Kinetic analysis of DCE-MRI is thus hypothesized to create an image reflecting the underlying malignant vasculature of an individual patient's tumor. There is mounting incentive to incorporate imaging surrogates, such as DCE-MRI, for patient selection and early measures of response in clinical trials of molecularly targeted anti-angiogenic therapies. (4) Imaging has the potential to provide more complete information on a tumor's microvascular biology, in contrast to information obtained from a biopsy, which may be subject to sampling error. In addition, imaging is non-invasive and spares the potential morbidities of biopsy, lending itself to serial measurements through a course of therapy.

However, data elucidating the molecular processes that underlie DCE-MRI and establishing its validity as a surrogate are lacking. Notable intraprostatic (5) and intratumoral (6) heterogeneity mandates millimeter co-localization accuracy between tissue samples and their corresponding image pixels. When prostate MR imaging and tissue acquisition procedures are performed in different settings and at different times, clinical co-registration is fraught with error. To address this key issue, we developed a technique for

MRI-guided needle biopsy of the prostate to be performed concurrently with a diagnostic MRI procedure inside a cylindrical 1.5T MRI scanner.

Methods

A patient with Stage I, intermediate-risk localized prostate cancer provided informed consent for enrollment on this IRB approved study. For the integrated procedure, the patient is positioned prone and a custom-designed interventional endorectal imaging coil is inserted and secured to the scanner table. A needle guide inside the stationary imaging coil contains MR tracking microcoils allowing for spatial registration of the device (R.C.S. et al, manuscript submitted, personal communication) (7). A continuous series of DCE-MR images of the prostate (3D spoiled GRE, scan time 5.1s, **Fig. IA**) are acquired before and during the injection of intravenous contrast (gadolinium chelate, 0.2mmol/kg, 3cc/s). The needle guide is translated and rotated within the endorectal coil until its trajectory, computed from the tracking coils, coincides with a biopsy target location defined on the diagnostic images. A 14G core biopsy needle is then inserted, its location is verified by MRI, and tissue is collected. **(Fig. IB and C)** This can be repeated for additional biopsy target sites within the prostate gland. The overall imaging and procedure time is approximately 90 minutes depending on the number of biopsies.

To analyze DCE-MRI data, a T1 map of the prostatic anatomy is first generated (8) to estimate the concentration of gadolinium chelate for a given signal intensity. Pixel data are submitted to a general kinetic model (GKM) fitting routine (9), which corrects the data for arterial input kinetics (measured over the external iliac artery) and implements a curve-

fitting solution to a GKM convolution integral. In this fashion, regions of interest (ROIs) encompassing those MR image pixels that correspond to the biopsy locations can be defined, and their corresponding time-intensity profiles and summary kinetic parameters computed. **(Fig. IE)** The transfer constant K^{trans} (corresponding to the magnitude of the enhancement curve, unit min^{-1}) and the rate constant k^{ep} (describing the rate of clearance, unit min^{-1}) are thought to reflect differences in tissue perfusion and microvascular permeability, respectively. The kinetic parameters are derived based on the following equation:

$$C_T(t) = K^{PS}\int C_P(\theta)e^{-k(t-0)}d\theta + f_{PV}C_P(t)$$

Where $C_T(t)$ = concentration of gadopentate in tumor tissue at any time t, K^{PS} = K_{TRANS}=endothelial transfer coefficient, C_P=concentration of gadopentate in the plasma space of the tumor tissue (assumed equal to that in the central venous blood plasma, i.e. input function), k= rate constant of reflux from interstitial water back to plasma, and $f_{PV=}$ fractional plasma volume of the tumor tissue.

To characterize the biological processes underlying the image data, needle biopsy specimens can be subjected to comprehensive histopathological, genomic, and proteomic analysis. Such analysis is chiefly enabled by microarray technology, which is distinguished by its comprehensive analytic capabilities using low sample volumes. In this case example, mRNA was isolated and amplified from snap frozen cores (10). The amplified mRNA was co-hybridized to a cDNA microarray with a reference standard. In turn, whole cell protein lysates from ethanol-fixed and paraffin-embedded tissue sections of

twin cores obtained at the same biopsy sites were analyzed using reverse phase protein arrays. (Ref 11 for detailed methods)

Early Results

We focused our initial analysis on signaling pathways known to be associated with angiogenesis. This case example shows differing levels of protein and gene expression at distinctive sites of contrast enhancement kinetics on DCE-MRI. **(Fig. 1I)** The level of hypoxia inducible factor (HIF-1α) mRNA and protein was lower at the site of higher contrast enhancement, while a number of other genes involved in angiogenesis signaling were upregulated. Some discordance observed at a single time point between protein and corresponding mRNA, for example AKT levels, supports the need for a comprehensive and serial analysis to evaluate mRNA/protein kinetics.

Conclusion

Our results show that the technical challenge of integrating needle-based prostate interventions with diagnostic MRI in a cylindrical clinical scanner can be overcome. Image subsites of interest can be precisely sampled, providing a research platform well suited to MRI and tissue correlation. The molecular profile prostate tissues underlying DCE-MRI will now be acquired in a larger series of patients in order to characterize the molecular biology of MR contrast enhancement. As we gain knowledge in the molecular biology underlying cancer and DCE-MRI, a more valid interpretation of an individual patients' tumor biology will ensue.

Acknowledgements: We thank A. Srikanchana for software support in DCE-MRI analysis, and Dr. M. Merino (Pathology).

References

1. Choyke PL, Dwyer AJ, Knopp MV (2003). Functional tumor imaging with dynamic contrast-enhanced magnetic resonance imaging. *J Magn Reson Imaging* 17:509-20.

2. Padhani AR, Dzik-Jurasz A (2004): Perfusion MR Imaging of Extracranial Tumor Angiogenesis. *Top Magn Reson Imaging* 15:41-57.

3. Dvorak HF, Nagy JA, Feng D, et al (1999). Vascular permeability factor/vascular endothelial growth factor and the significance of microvascular hyperpermeability in angiogenesis. *Curr Top Microbiol Immunol* 237:97-132.

4. Smith JJ, Sorensen AG, Thrall JH (2003). Biomarkers in imaging: realizing radiology's future. Radiology 227:633-8.

5. Aihara M, Wheeler TM, Ohori M, et al (1994). Heterogeneity of prostate cancer in radical prostatectomy specimens. *Urology* 43:60-6; discussion 66-7.

6. Evans SM, Hahn SM, Magarelli DP, et al (2001). Hypoxic heterogeneity in human tumors: EF5 binding, vasculature, necrosis, and proliferation. *Am J Clin Oncol* 24:467-72.

7. Krieger A, Susil RC, Ménard C, et al (2004). Design of a Novel MRI Compatible Manipulator for Image Guided Prostate Interventions. *IEEE Transactions on Biomedical Engineering,* In press.

8. Deoni SC, Rutt BK, Peters TM (2003). Rapid combined T1 and T2 mapping using gradient recalled acquisition in the steady state. *Magn Reson Med* 49:515-26.

9. Kety S (1960): Blood Tissue Exchange Methods; Theory of Blood Tissue Exchange and it's Application to Measurement of Blood Flow. *Meth. Med. Res.* 8:223-227.

10. Goley EM, Anderson S, Ménard C, et al (2004). Microarray analysis in clinical oncology: pre-clinical optimization using needle core biopsies from xenograft tumors. *BMC Cancer* 4:20.

11. Espina V, Mehta AI, Winters ME, et al (2003): Protein microarrays: molecular profiling technologies for clinical specimens. Proteomics 3:2091-100.

Figure Legends

Figure I: Prostate interventional MRI for the correlation of molecular biology and DCE-MRI. The stationary interventional endorectal coil (∗) is used for both diagnostic and interventional MR imaging. **(a)** DCE-MRI at 120s shows a small area of increased signal intensity in the left peripheral zone of the prostate. ROIs (red an blue) corresponding to the subsequent needle biopsy voids **(b,c)** are defined for image analysis. **(e)** Time-intensity curves (corrected for T1 heterogeneity) from each ROI are fit to a GKM convolution integral using an arterial input function measured from the external iliac artery. The transfer constant K^{trans} (corresponding to the magnitude of the enhancement curve, unit min^{-1}) and the rate constant k^{ep} (describing the rate of clearance, unit min^{-1}) are thought to reflect differences in the perfusion and microvascular permeability underlying each ROI, respectively.[2] H&E staining shows adenocarcinoma **(d)** corresponding to higher K^{trans} and k^{ep} than benign tissue **(f)**. cDNA microarray **(g,k)** and reverse phase protein array **(h,j-** array probed with STAT3 antibody shown) (11) results show differing trends of protein and gene expression levels **(i)** from benign (blue ROI) to malignant (red ROI) tissue obtained at distinctive sites of contrast enhancement kinetics on DCE-MRI.

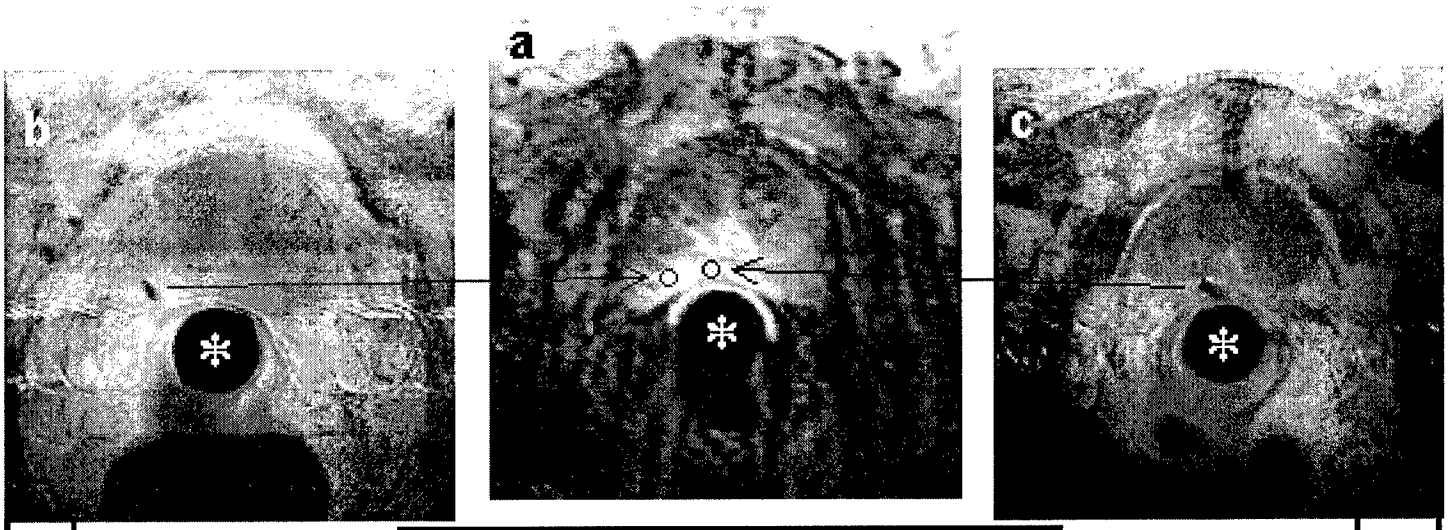

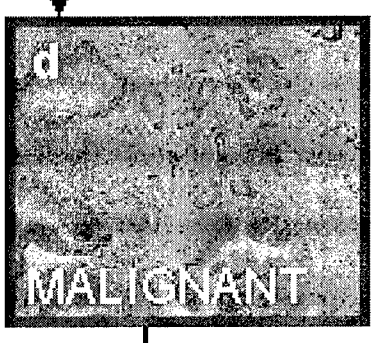

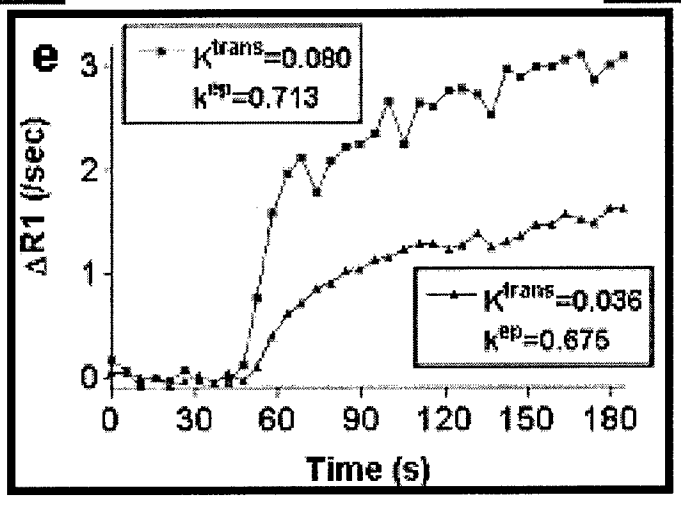

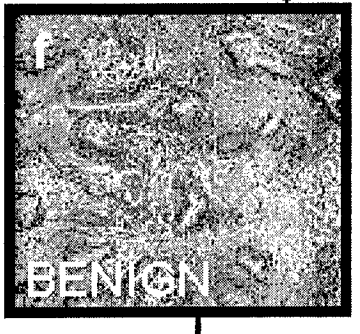

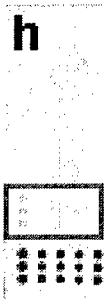

i Array	Pathway	↑	↓
cDNA Microarray	Hypoxia	NOS3, VHL	HIF1A
	PDGF	MAPK8, STAT3 PDGFRA	FOS, JUN, MAP2K1&4
	AKT	AKT1	EIF2S1&3
Protein Array	Hypoxia	-	HIF1a, eNOS
	PDGF	-	PDGFβ, pPDGFβ, STAT3
	AKT	-	AKT, pAKT, EIF4G

Transrectal Prostate Biopsy and Fiducial Marker Placement in a Standard 1.5T MRI Scanner

Robert C Susil PhD[1]*, Cynthia Ménard MD[2]*, Axel Krieger MS[3], Jonathan A Coleman MD[4], Kevin Camphausen MD[2], Peter Choyke MD[5], Gabor Fichtinger PhD[6], Louis L Whitcomb PhD[7], C Norman Coleman MD[2], Ergin Atalar PhD[1,3,8]

Departments of Biomedical Engineering[1], Radiology[3],
Computer Science[6], and Mechanical Engineering[7]
Johns Hopkins University School of Medicine
Baltimore, MD 21205

Radiation Oncology Branch – NCI[2], Urologic Oncology Branch – NCI[4],
Department of Radiology- Clinical Center[5]
National Institutes of Health, DHHS
Bethesda, MD 20892

Department of Electrical and Electronics Engineering[8]
Bilkent University
Ankara, Turkey 06533

*Co-first authors

Correspondence:
Ergin Atalar, Ph.D.
Johns Hopkins University
Traylor Building – Rm 330
720 Rutland Avenue
Baltimore, MD 21205
Phone: (410) 955-9617
FAX: (443) 287-6730
e-mail: eatalar@jhu.edu

Supported in part by Sup U.S. Army Prostate Cancer Research Program Award DAMD17-01-1-0064, NSF ERC 9731478, and an NSF ERC PER grant. RCS is supported by an NIH training grant and CM is supported in part by an ASTRO fellowship.

This paper was originally presented at the 2003 RSNA meeting (ID #108095).

Submission Type: Original Research

Transrectal Prostate Biopsy and Fiducial Marker Placement in a Standard 1.5T MRI Scanner

Submission Type: Original Research

Abstract

Purpose: To investigate the safety and accuracy of a system that provides transrectal needle access to the prostate while a patient is imaged inside of a standard 1.5T MRI scanner, which previously has not been possible.

Methods: Five patients with previously diagnosed localized prostate cancer were selected for MRI-guided intraprostatic placement of gold fiducial markers and/or prostate biopsy. Four fiducial marker placement procedures were performed; by depositing fiducial markers within the gland, it was possible to assess not only needle placement accuracy, but also the accuracy with which the tissue itself was targeted. Subsequently, three 1.5T MRI-guided prostate biopsy procedures were performed.

Results: The mean procedure duration was 76 minutes; all patients tolerated the intervention well and no unexpected adverse events occurred. Mean needle placement accuracy (targeted vs. actual needle placement) was 1.9 mm for the fiducial marker placement procedures and 1.8 mm for the biopsy procedures. The mean fiducial marker placement error transverse to the needle direction was 2.6 mm; this measurement is the most relevant predictor of accuracy in collecting core biopsies. The gold fiducial markers were subsequently used to assess daily alignment and prostate motion during a standard course of external beam radiation therapy for prostate cancer.

Conclusion: Transrectal, 1.5T MRI-guided prostate biopsy and fiducial marker placement appears feasible and safe using this 'APT-MRI' system (Access to Prostate Tissue under MRI guidance). Further studies involving larger patient cohorts are warranted to investigate the potential clinical benefits of MRI-guided tissue biopsy and minimally-invasive therapies in a standard 1.5T scanner architecture.

Keywords: MRI, prostate, prostatic neoplasms, biopsy, interventional MRI

Introduction

With an estimated annual incidence of 220,900 cases in 2003, prostate cancer is the most common non-cutaneous cancer in men in the United States (1). Currently, approximately one million trans-rectal ultrasound-guided (TRUS) biopsies are performed annually in the United States as part of the diagnostic workup for prostate cancer (2). While TRUS prostate biopsy is a specific test for prostate cancer, it has a low sensitivity, which often results in multiple biopsy procedures in patients with suspected prostate cancer. TRUS guided biopsy fails to correctly detect the presence of prostate cancer in approximately 20% of cases (3).

MR imaging has a potentially valuable role in the diagnosis of prostate cancer. MRI , using an endorectal receiver coil, has a higher sensitivity for detecting prostate tumors than transrectal ultrasound (4); however, due to its low specificity, the role of MRI in prostate cancer diagnosis and staging has been limited (5). One potential solution is to combine tissue biopsy with MR imaging (i.e. to directly biopsy tissue regions which have a suspicious MR appearance), thereby maintaining the sensitivity of MRI while gaining the specificity of tissue biopsy.

Prior work has been performed on low field strength (e.g. 0.2 or 0.5T) open scanner architectures (6-8). While these systems provide easier access to the patient, they do not produce the highest quality MR images, have limited potential for functional and spectroscopic imaging, and are less widely available. To improve image quality, some groups have investigated hybrid approaches in which priorly acquired 1.5T MR images are registered to images acquired with a lower field strength scanner, where the actual intervention is performed (9-11). Others have registered priorly acquired 1.5T MR

images with intraoperative ultrasound images (12, 13). While both of these image registration approaches simplify the intervention itself, registration between image sets, particularly in highly deformable organs such as the prostate, can introduce inaccuracies.

There are currently no systems that allow for transrectal needle placement concurrent with the acquisition of diagnostic quality MR images in a "closed" 1.5T MR scanner architecture. An obvious application of such a system is MR-guided diagnostic prostate biopsy. However, performing MRI-guided minimally-invasive therapeutic interventions is also of interest (14). In the research setting, such a system could provide for direct histologic validation of various prostate MR imaging techniques. By collecting tissue samples co-localized with MR data, such as proton spectroscopy (15) or dynamic contrast enhancement (16), radiologic-pathologic correlations could be established. Such a system could also provide for serial tissue acquisition (over a period of months or years) from the same site within the prostate, a valuable tool for therapeutic monitoring and assessment (17).

In this pilot study, we investigate the safety and accuracy of a novel 'APT-MRI' system (Access to Prostate Tissue under MRI guidance) that allows transrectal needle access to the prostate while a patient is imaged inside of a "closed" 1.5T MRI scanner. In five patients with localized prostate cancer, this device was used for four fiducial marker placement procedures and three MRI-guided prostate biopsy procedures.

Methods

Interventional device

The design principle and mechanics of the interventional device employed in this study are similar to those of a previous, non-clinical device, which was used in a series of experimental canine studies (14). The clinical-grade device used here is smaller and is designed for easy sterilization. Other changes include an increase in the needle exit angle (from 30 to 36 degrees) because of differences between canine and human pelvic anatomy, the addition of flexible control rods that allow for positioning of the needle guide from the edge of the scanner bore, and a redesign of the immobilization arm (18). An investigational-device-exemption was obtained through our Institutional Review Board (IRB) and the study was performed with IRB approval.

A 23 mm-diameter hollow endorectal sheath, placed at the beginning of the procedure, remains immobile throughout the intervention (Figure 1A). The sheath includes an integrated 20 mm-diameter single-turn imaging coil surrounding an anterior window that allows for needle access to the prostate. The entire sheath, including the window, is covered with medical grade heat-shrink plastic (Crosslinked Fluoropolymer, Tyco Elec. Corp., Menlo Park, CA) and an elastic probe cover (Civco Medical Instruments, Kalona, IA), both of which are easily punctured as the interventional needle emerges from the sheath window. An 18 mm-diameter cylindrical needle guide fits inside the stationary rectal sheath, contains MR tracking microcoils (allowing for device registration), and has a curved needle channel (allowing the needle, inserted axially, to exit at a 36 degree angle, passing through the rectal wall and into the prostate) (Figure 1B). The cylindrical needle guide is mounted on a positioning stage (length = 4.5 cm,

diameter = 7.0 cm, weight = 250 g) (Figure 1C), which contains the mechanism that converts the rotation of two flexible phosphor-bronze control rods (S.S. White Technologies Inc., Piscataway, NJ) (Figure 1D) - each extending to the edge of the scanner bore - into rotation and translation of the needle guide. Finally, the positioning stage is attached to an immobilization arm mounted on a linear rail (Figure 1D). Unless otherwise noted, all parts of the device were fabricated from Ultam plastic (GE Plastics, Brea, CA).

Because the device has a coaxial design, the central axis provides an open channel for needle passage. The needles are inserted from the back of the device, pass through its central axis, are curved within the needle guide, and emerge from the lateral wall of the needle guide. The marker-placement needles consist of three components, all custom made from nitinol metal: an 18 G hollow canula with a beveled tip, an inner stylus with a three-faced beveled tip (used during insertion of the canula), and a flat tipped inner stylus (used to push the gold fiducial markers through the canula and into the tissue) (MRI-Devices Daum, Schwerin, Germany). Nitinol was chosen because of its excellent biocompatibility and superelastic properties, which prevent plastic deformation of the needle when it is curved inside the needle guide (i.e. permanent bending).

To accommodate standard 14-gauge spring-loaded MRI-compatible biopsy guns (MRI-Devices Daum, Schwerin, Germany), a straight needle path was needed. Therefore, for the biopsy procedures, a needle guide with 20 and 30 degree straight needle channels and a modified endorectal sheath were used (Figure 2A). In all three prostate biopsy procedures, it was possible to access all sites within the prostate using

one of the two needle channels (Figure 2B). The 30 degree channel is used for apical targets while the 20 degree channel is employed for targets closer to the prostate base.

Patient enrollment and preparation

After providing informed consent, five patients were enrolled in an investigational protocol reviewed and approved by our IRB. All patients were previously diagnosed with clinically localized prostate cancer and were scheduled to receive a standard course of conformal external beam radiation therapy. Four of the patients were consented for MRI-guided intra-prostatic placement of four gold fiducial markers (4 mm long; 0.8 mm diameter; 24K gold; Northwest Medical Physics Equipment, Lynnwood, WA); the fiducial markers were subsequently used for daily assessment and adjustment of external radiation beam targeting. Three of the patients were consented for MRI-guided prostate biopsy.

Two days before and on the morning of the procedure, patients received prophylactic antibiotics (Levofloxacin, 500mg po qd). Also, a rectal enema was self administered on the morning of the intervention. Immediately before the procedure, local anesthesia was administered via ultrasound guided transrectal injection of 10 ml of 0.25% Marcaine along the periprostatic neurovascular bundles bilaterally. One patient was given 2 mg of Lorazepam orally as an anxiolytic. The patients were then brought to the MR suite and positioned prone on the scanner table. Foam supports were used to elevate the pelvis, abdomen, and chest by 10 cm to increase patient stability and comfort. Following a digital rectal exam, the rectal sheath - including the local imaging coil - was placed. The rest of the system, including the cylindrical needle guide and the positioning stage, were then docked with the endorectal sheath. Subsequently, the entire system was

immobilized, via the two ball joints and the linear rail, to prevent motion of the setup. The patients were advanced into the scanner where scout images were collected to verify the positioning of the device relative to the patient's anatomy (typically, zero or one positional adjustments were necessary to achieve the proper sheath depth).

Fiducial marker placement procedure

All interventions were performed on a GE Signa Excite 1.5 T MR scanner (GE Medical Systems). Four pulse sequences were used during these studies: three for anatomical imaging and a fourth for device tracking. After the patients were positioned in the scanner and scout images acquired, T2-weighted fast spin-echo images were acquired in the axial and sagittal planes for visualization of the intraprostatic and periprostatic anatomy (FSE-XL, TE 102 msec, TR 6.0 sec, BW +/-20.83 KHz, ETL 16, FOV 16 cm, slice thickness 3mm, interslice spacing 0 mm, 256x192, NEX 3, scan time 3:36). After acquisition, these images were automatically loaded into the visualization and targeting program, which was displayed on a screen (Da-Mat, Da-Lite Inc., Warsaw, IN) in the scanner room using an LCD projector (LP340b LCD Projector, Infocus Corp., Wilsonville, OR) (Figure 3B). A target for needle placement was selected and graphically marked on these images (Figure 4).

Next, a device-tracking pulse sequence was run to determine the current position of the endorectal needle guide (via localization of the three tracking microcoils inside of the device) (14, 19). This 60 msec pulse sequence consists of 12, dodecahedrally spaced 1D gradient-echo projections (no slice selection is used) (TE 2.3 msec, TR 5.0 msec, BW +/-64 KHz, FA 1^{o}, FOV 40cm, 256 readout points). By knowing (1) the position of the target, (2) the position of the needle guide, and (3) the needle path relative to the needle

guide (determined via a prior device calibration), the amount of rotation and translation necessary to place the target on the needle trajectory could be calculated by the targeting program and displayed for the operator (Figure 4). The depth of needle insertion necessary to reach the target was also calculated and displayed as part of the user interface.

As the operator moved the needle guide via the two control knobs (Figure 3A), the tracking pulse sequence was run continuously and the remaining rotation and translation required were displayed. When the needle guide was correctly positioned, the tracking pulse sequence was stopped and the patient table withdrawn from the scanner to provide access to the device. To control the depth of needle insertion, a needle stop was set, placed at the back of the device, and the nitinol needle and canula were introduced together.

Needle position was confirmed using a T1-weighted fast spin-echo acquisition (FSE-XL, TE 9.5 msec, TR 1.25 sec, BW +/- 31.25 KHz, ETL 4, FOV 16 cm, slice thickness 3 mm, interslice spacing 0 mm, 256x256, NEX 1, scan time 1:20). A fiducial marker was then placed using the nitinol stylus and a canula withdrawal technique, as described previously (14), and the prostate was imaged using a T2*-weighted gradient-echo pulse sequence (GE, TE 15 msec, TR 467 msec, BW +/- 15.6 KHz, FA 30 deg, FOV 16 cm, slice thickness 3 mm, interslice spacing 0 mm, 256x256, NEX 1, scan time 2:00). Because pure gold fiducial markers produce little susceptibility artifact and therefore little signal void (20), it was necessary to use T2*-weighting to robustly visualize the fiducial markers. Following imaging of the fiducial marker, another target was selected

(using the T2-weighted fast spin-echo images), and the needle/marker placement procedure repeated.

After placement of the four gold markers, patients were removed from the scanner suite and observed in the hospital until they successfully voided without difficulty. One week following the procedure, all patients were interviewed concerning any adverse events.

Biopsy procedure

Patient preparation and scan room setup for the three MRI-guided prostate biopsy procedures was identical to that described for the fiducial marker procedures. Targets were selected using axial T2-weighted fast spin echo images and needle location was confirmed using axial T1-weighted fast spin echo images (as described). Five biopsies were performed in each of three procedures.

Results

Five patients were enrolled in the study, all of whom completed the protocol. With these patients, four fiducial marker placement procedures and three biopsy procedures were performed. The average patient weight and height were 88kg and 173 cm; maximum weight and height were 132 kg and 183 cm. All patients tolerated the procedure well and reported minimal discomfort. The major patient complaint during the procedure was shoulder pain due to hyperextension of the joint when lying prone on the scanner table (this was relieved in later studies by using extra foam supports for the chest, which reduce the shoulder angle).

The average total duration for the MR procedure was 76 minutes (maximum 93 minutes, minimum 60 minutes); the average time required for each of the four fiducial marker placements was 13 minutes, including time for target selection, needle placement, fiducial marker deposition, and all confirmatory imaging. Before each procedure, an additional 15 minutes was required for administration of local anesthesia and 15 minutes for patient positioning. Following the intervention, patients were observed for an average of 2 hours until successfully voiding without difficulty. No unexpected toxicities and no Common Toxicity Criteria (CTC) grade II or higher urinary complications were reported.

Intra-procedure imaging

In Figure 5, Column 1, typical T2-weighted fast spin-echo images acquired for target selection are shown. To improve visualization in and around the prostate, all images were intensity corrected, producing uniform signal images, as described previously (21). With the needle in place, the prostate was imaged again using a T1-weighted fast spin-echo sequence, allowing for confirmation of needle placement accuracy (Figure 5,

Column 2). After each gold fiducial marker was deposited, T2*-weighted axial images were acquired to confirm marker location (Figure 5, Column 3). Because there is no motion of the endorectal sheath during the procedure, excellent registration is maintained throughout (i.e. there is little soft tissue movement between image acquisitions).

Needle and fiducial marker placement accuracy

Needle and fiducial marker placement accuracy were measured using the axial images acquired during the procedure. Needle accuracy was the absolute distance between the target location and the center of the needle tip bloom. Fiducial marker placement accuracy was the absolute distance between the target point and the center of the marker void. The mean needle placement error was 1.9 mm (maximum error 2.3 mm) (Figure 6, Panel A). The mean fiducial marker placement error was 4.8 mm (maximum error 8.3 mm) (Figure 6, Panel B). The mean fiducial marker placement error transverse to the needle direction was 2.6 mm (maximum error 4.6 mm) (Figure 6, Panel C). Because tissue biopsy cores are typically 1.5 cm long, transverse error measurements are more relevant for assessing the accuracy of the system for collecting tissue samples.

Biopsy needle placement accuracy

Three MR-guided prostate biopsy procedures were performed. Biopsy locations were selected using T2-weighted fast spin-echo images (Figure 7A). Subsequently, after inserting the biopsy needle but before collecting the tissue core biopsy, T1-weighted fast spin-echo images were acquired to confirm biopsy needle placement accuracy (Figure 7B and 7C). A total of 15 tissue biopsies were collected; mean biopsy needle placement accuracy was 1.8 mm.

Discussion

This pilot study demonstrates the feasibility and safety of performing transrectal MRI-guided prostate biopsies and fiducial marker placements. Minor errors were observed in placing the needles with this device. Needle placement accuracy is measured by comparing the location of the target, defined by an scanner-based 3D coordinate, with the center of the needle tip bloom artifact. However, just because the needle has been placed at the proper coordinate relative to the MR scanner does not imply that the needle is at the correct location in the tissue. In evaluating the needle and fiducial marker placement accuracy, it is evident that needle placement is notably more accurate than fiducial marker placement. This is the result of tissue deformation which occurs upon insertion of the needle.

Tissue targeting accuracy was assessed by comparing the location of the gold fiducial markers, deposited in the tissue, *after* the needle had been removed. Assuming that the tissue returns to its original shape after the needle is withdrawn, the location of the deposited fiducial marker relative to the target point gives an accurate measure of tissue targeting accuracy. This assumption was confirmed by comparing images of the prostate acquired both before and following needle placements (Figure 8).

As expected, the prostate was elastically deformed while the needle was within the tissue. The majority of markers were deposited in the tissue proximal to the target location (as measured along the needle insertion axis). To reduce the impact of deformation on tissue targeting accuracy, needles in the last two procedures were inserted 5 mm past the target site and then withdrawn back to the intended target depth before depositing the fiducial marker. As deformation was most pronounced at the base of the

prostate, needles targeted in this area were inserted 8 mm past the target and then withdrawn back to the prescribed depth. This technique notably improved fiducial marker placement accuracy; average marker placement accuracy for the four procedures were, respectively: 5.9 mm, 5.1 mm, 4.7 mm, and 3.5 mm. Improvements in patient positioning, which helped to immobilize the prostate, also contributed to this accuracy improvement. In particular, downward pressure was applied to the device before locking it into place, which immobilized the prostate against the pubic symphysis.

An alternative explanation for the fiducial marker placement errors is that the markers were not accurately deposited at the tip of the cannula or that they were 'suctioned back' as the cannula and stylus were withdrawn from the tissue. Both prior experience with this deposition technique (14) and experiments performed in clear polyacrylamide-gel phantoms (results not shown) do not support this explanation.

As we are ultimately interested in the accuracy with which tissue samples can be acquired from the prostate, the transverse component of fiducial marker placement error was also examined (i.e. perpendicular to the needle insertion axis). Commonly, core tissue biopsies are 15 mm long and approximately 1.5 mm in diameter. Therefore, because the tissue core is so long, small errors in the insertion depth of the biopsy needle are not of great consequence. However, because the core is narrow, transverse errors in needle placement are of greater concern. The transverse tissue targeting accuracy obtained with this system, 2.6 mm, is adequate for MR-guided biopsy (as image pixels are rarely smaller than 0.5mm, lesions which are less than 2-3 mm in size are unlikely to be MR visible).

In addition to allowing for assessment of prostate tissue targeting accuracy, the fiducial markers used in this study have additional research and clinical value. As part of this study's protocol, the markers are being used to help assess daily setup errors and prostate motion during external beam radiation therapy (which is delivered in daily fractions over the course of several weeks). As the gold fiducial markers are visible using planar x-ray imaging, the markers can be imaged when the patient is positioned for radiation treatment on a daily basis, allowing for fine adjustment of radiation beam targeting (22). In addition to this use, fiducial markers have also shown value by improving multimodality image fusion (i.e. between CT and MR images) for radiation treatment planning (20). Finally, for patients who are scheduled for subsequent radical prostatectomy, implantation of fiducial markers allows for close correlation of MR images with histological analysis of the whole-mount prostate specimens (i.e. by placing a fiducial marker within a suspicious MR-visible lesion, the corresponding tissue can easily be located in the prostate specimen).

In summary, we emphasize four key features of the APT-MRI system investigated in this study. First, the entire device is very compact and therefore, can be used in a standard 1.5 T cylindrical scanner architecture, even with larger patients (the largest patient treated was 132 kg, 4 kg less the manufacturer limit for the scanner table). As standard scanner architectures are much more widely available than open models, this system will be applicable at many centers and moreover, can immediately take advantage of mainstream MRI hardware and pulse-sequence development (such as the introduction of 3.0T whole body scanners). Second, the needle placement procedure is uncomplicated; 4 targeted needle placements can be performed with an overall MR

procedure time of approximately one hour (including time for confirmatory imaging after every needle and fiducial marker placement). Third, the endorectal sheath, which includes the local imaging coil and entirely contains the needle guide, remains stationary throughout the procedure. This design helps to prevent deformation of the prostate and surrounding tissues during the procedure, maintaining accurate registration of all image data sets and reducing the need for deformable registration techniques (23, 24). Also, it prevents distension of the rectal wall during needle guide positioning, improving patient comfort. Finally, we do not rely heavily on 'realtime' imaging techniques. Other than the device-tracking pulse sequence, no specialized pulse sequences are required when using this device. Therefore, we maintain the flexibility to use virtually any imaging technique, including MR spectroscopy and dynamic contrast enhancement, both of which have shown promise in the diagnosis and delineation of tumors within the prostate. Currently, we have focused on anatomic imaging techniques; subsequent work will investigate the application of the device with pulse sequences that provide information about the functional and metabolic state of the tissue.

Conclusion

A system for accurate transrectal intraprostatic needle placement concurrent with MR imaging using a standard 1.5T scanner architecture is described (termed the APT-MRI system). In five patients with localized prostate cancer, a total of 16 gold fiducial markers were placed and 15 prostate biopsies were collected using MR image guidance. The mean needle placement accuracy was 1.9 mm for the fiducial marker placement studies and 1.8 mm for the biopsy procedures. The mean fiducial marker placement accuracy was 4.8 mm and the mean transverse fiducial marker placement accuracy was 2.6 mm (which is the best predictor of tissue biopsy acquisition accuracy). By combining accurate needle guidance with high-quality imaging, the APT-MRI system provides new opportunities for image-guided diagnostic and therapeutic prostate interventions.

References

1. Jemal A, Murray T, Samuels A, Ghafoor A, Ward E, Thun MJ. Cancer statistics, 2003. CA Cancer J Clin. 2003; 53:5-26.
2. Reyes AO, Humphrey PA. Diagnostic effect of complete histologic sampling of prostate needle biopsy specimens. Am J Clin Pathol. 1998; 109:416-422.
3. Rabbani F, Stroumbakis N, Kava BR, Cookson MS, Fair WR. Incidence and clinical significance of false-negative sextant prostate biopsies. J Urol. 1998; 159:1247-1250.
4. Yu KK, Hricak H. Imaging prostate cancer. Radiol Clin North Am. 2000; 38:59-85, viii.
5. Wefer AE, Hricak H, Vigneron DB, et al. Sextant localization of prostate cancer: comparison of sextant biopsy, magnetic resonance imaging and magnetic resonance spectroscopic imaging with step section histology. J Urol. 2000; 164:400-404.
6. Cormack RA, Kooy H, Tempany CM, D'Amico AV. A clinical method for real-time dosimetric guidance of transperineal 125I prostate implants using interventional magnetic resonance imaging. Int J Radiat Oncol Biol Phys. 2000; 46:207-214.
7. D'Amico AV, Tempany CM, Cormack R, et al. Transperineal magnetic resonance image guided prostate biopsy. J Urol. 2000; 164:385-387.
8. D'Amico AV, Cormack R, Tempany CM, et al. Real-time magnetic resonance image-guided interstitial brachytherapy in the treatment of select patients with clinically localized prostate cancer. Int J Radiat Oncol Biol Phys. 1998; 42:507-515.
9. Cormack RA, D'Amico AV, Hata N, Silverman S, Weinstein M, Tempany CM. Feasibility of transperineal prostate biopsy under interventional magnetic resonance guidance. Urology. 2000; 56:663-664.
10. Fei B, Duerk JL, Boll DT, Lewin JS, Wilson DL. Slice-to-volume registration and its potential application to interventional MRI-guided radio-frequency thermal ablation of prostate cancer. IEEE Trans Med Imaging. 2003; 22:515-525.

11. Hata N, Jinzaki M, Kacher D, et al. MR imaging-guided prostate biopsy with surgical navigation software: device validation and feasibility. Radiology. 2001; 220:263-268.
12. DiBiase SJ, Hosseinzadeh K, Gullapalli RP, et al. Magnetic resonance spectroscopic imaging-guided brachytherapy for localized prostate cancer. Int J Radiat Oncol Biol Phys. 2002; 52:429-438.
13. Kaplan I, Oldenburg NE, Meskell P, Blake M, Church P, Holupka EJ. Real time MRI-ultrasound image guided stereotactic prostate biopsy. Magn Reson Imaging. 2002; 20:295-299.
14. Susil RC, Krieger A, Derbyshire JA, et al. System for MR image-guided prostate interventions: canine study. Radiology. 2003; 228:886-894.
15. Kurhanewicz J, Swanson MG, Nelson SJ, Vigneron DB. Combined magnetic resonance imaging and spectroscopic imaging approach to molecular imaging of prostate cancer. J Magn Reson Imaging. 2002; 16:451-463.
16. Jager GJ, Ruijter ET, van de Kaa CA, et al. Dynamic TurboFLASH subtraction technique for contrast-enhanced MR imaging of the prostate: correlation with histopathologic results. Radiology. 1997; 203:645-652.
17. Crawford ED, Fair WR, Kelloff GJ, et al. Chemoprevention of prostate cancer: guidelines for possible intervention strategies. J Cell Biochem Suppl. 1992; 16H:140-145.
18. Krieger A, Susil RC, Menard C, et al. Design of A Novel MRI Compatible Manipulator for Image Guided Prostate Interventions. IEEE Trans on Biomed Eng. 2004:In Submission.
19. Dumoulin CL, Souza SP, Darrow RD. Real-time position monitoring of invasive devices using magnetic resonance. Magn Reson Med. 1993; 29:411-415.
20. Parker CC, Damyanovich A, Haycocks T, Haider M, Bayley A, Catton CN. Magnetic resonance imaging in the radiation treatment planning of localized prostate cancer using intra-prostatic fiducial markers for computed tomography co-registration. Radiother Oncol. 2003; 66:217-224.
21. Susil RC, Camphausen K, Choyke P, et al. MRI-Guided Transperineal Prostate Interventions in a Standard 1.5T Magnet. in submission.

22. Pang G, Beachey DJ, O'Brien PF, Rowlands JA. Imaging of 1.0-mm-diameter radiopaque markers with megavoltage X-rays: an improved online imaging system. Int J Radiat Oncol Biol Phys. 2002; 52:532-537.

23. Fei B, Duerk JL, Wilson DL. Automatic 3D registration for interventional MRI-guided treatment of prostate cancer. Comput Aided Surg. 2002; 7:257-267.

24. Mizowaki T, Cohen GN, Fung AY, Zaider M. Towards integrating functional imaging in the treatment of prostate cancer with radiation: the registration of the MR spectroscopy imaging to ultrasound/CT images and its implementation in treatment planning. Int J Radiat Oncol Biol Phys. 2002; 54:1558-1564.

Figure Legends

Figure 1: The APT-MRI system. **Panel A**: The stationary endorectal sheath, with an integrated 20 mm diameter single-turn imaging coil, minimizes tissue deformation during the interventional procedure. **Panel B**: The cylindrical needle guide contains MR-tracking microcoils and a curved needle channel. **Panel C**: The positioning stage houses the mechanism that converts rotation of the two control rods into rotation and translation of the needle guide, which fits inside of the endorectal sheath. **Panel D**: The positioning arm, with two lockable aluminum ball-joints and a linear rail, allows for easy device positioning and subsequently, rigid immobilization.

Figure 2: Prostate biopsy needle guide and sheath. **Panel A**: To accommodate 14-gauge spring-loaded biopsy guns, a modified needle guide with two, straight needle channels (30 degrees and 20 degrees) and a modified endorectal sheath were used. **Panel B**: A sagittal T1-weighted fast spin-echo image was acquired with the biopsy needle in place. Using one of the two needle channels, all sites within the prostate could be accessed.

Figure 3: MR scanner room setup. **Panel A**: The two flexible control rods extend to the edge of the scanner bore, allowing for rotation and translation of the needle guide while the prostate is located at the scanner isocenter. **Panel B**: The image display and targeting application is projected onto a screen in the scanner room.

Figure 4: Image display and targeting application. A target (white circle) is graphically selected within a diffuse, low intensity region (suspicious for prostate cancer) in the left posterior lobe of the prostate. The intersection of the image plane and the projected needle path (white cross) as well as the axis of the needle guide (white square) are also shown. As the device is moved, the targeting commands and the projected needle path are updated in realtime.

Figure 5: Targeting, needle, and fiducial-marker visualization images. Images from two patients (**Rows A and B,** respectively), show images acquired during the fiducial-marker placement procedure. **Column 1**: Targets are selected on axial, T2-weighted fast spin-echo images. **Column 2**: The needle tip void is visualized in axial, T1-weighted fast spin-echo images. **Column 3**: The marker void is visualized on axial, T2*-weighted gradient-echo images. Note that there is minimal tissue motion throughout each procedure.

Figure 6: Needle and fiducial-marker placement accuracy. Error histograms show needle tip location errors (**Panel A**), fiducial marker location errors (**Panel B**), and fiducial marker in-plane location errors (**Panel C**) for all 16 gold fiducial markers placed. Mean placement errors for each are 1.9 mm, 4.8 mm, and 2.6 mm, respectively. Because tissue core biopsies are typically 1.5 cm long, the last measure, fiducial marker in-plane placement error, is the best predictor of tissue biopsy acquisition accuracy.

Figure 7: Biopsy target and needle visualization images. Biopsy locations were selected on axial, T2-weighted fast spin-echo images (**Panel A**). The 14-gauge biopsy needle void is visualized in axial, T1-weighted fast spin-echo images (**Panel B & C**).

Figure 8: T1-weighted axial fast-spin-echo images of the prostate acquired 20 minutes (**Panel A**), 40 minutes (**Panel B**), and 50 minutes (**Panel C**) after the start of the procedure. Throughout the intervention, including 4 needle placements, the prostate and surrounding tissues remain stable. Importantly, the stationary endorectal sheath prevents movement of the needle guide from causing tissue deformation.

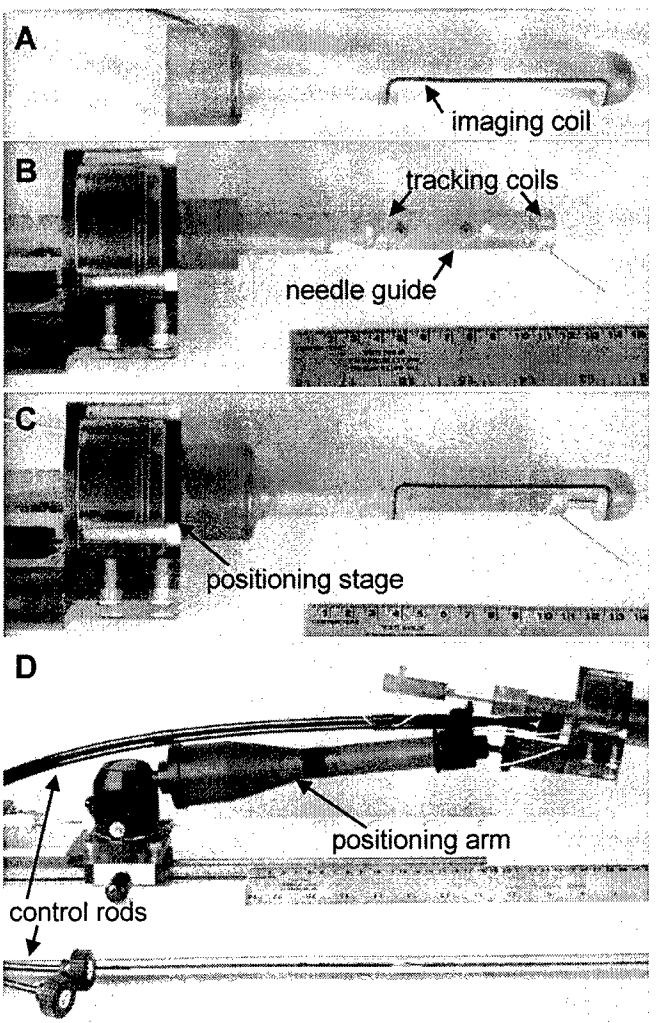

Figure 1: The APT-MRI system. **Panel A**: The stationary endorectal sheath, with an integrated 20 mm diameter single-turn imaging coil, minimizes tissue deformation during the interventional procedure. **Panel B**: The cylindrical needle guide contains MR-tracking microcoils and a curved needle channel. **Panel C**: The positioning stage houses the mechanism that converts rotation of the two control rods into rotation and translation of the needle guide, which fits inside of the endorectal sheath. **Panel D**: The positioning arm, with two lockable aluminum ball-joints and a linear rail, allows for easy device positioning and subsequently, rigid immobilization.

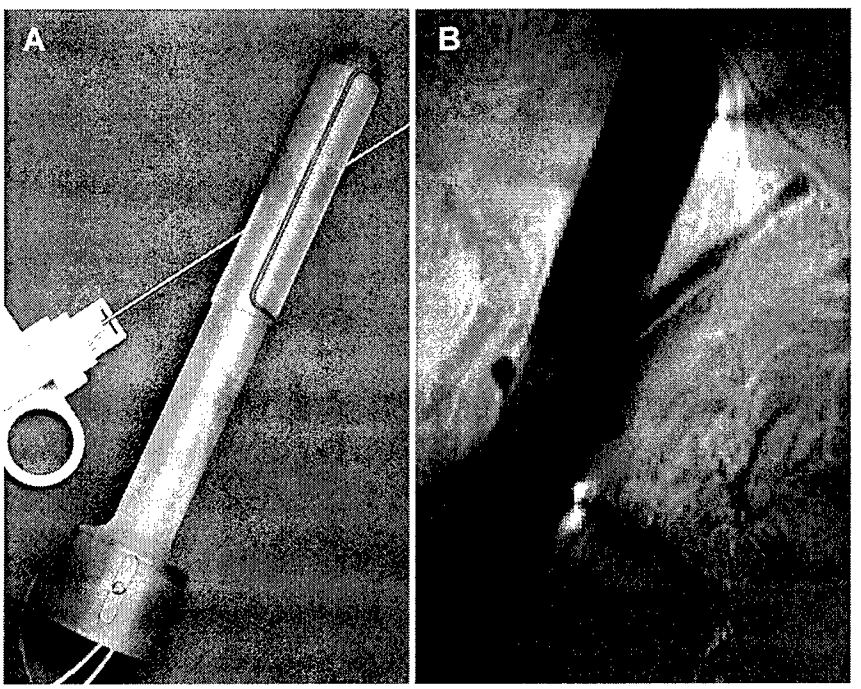

Figure 2: Prostate biopsy needle guide and sheath. **Panel A**: To accommodate 14-gauge spring-loaded biopsy guns, a modified needle guide with two, straight needle channels (30 degrees and 20 degrees) and a modified endorectal sheath were used. **Panel B**: A sagittal T1-weighted fast spin-echo image was acquired with the biopsy needle in place. Using one of the two needle channels, all sites within the prostate could be accessed.

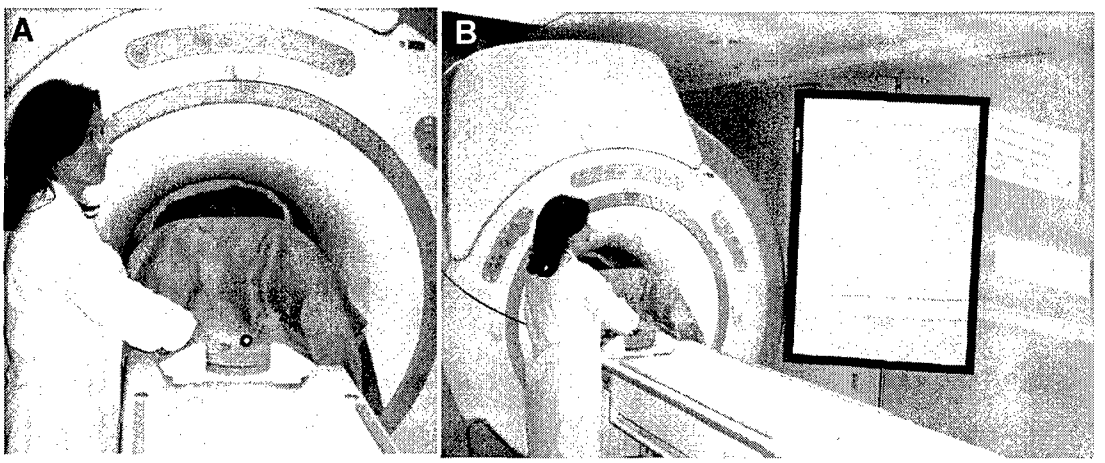

Figure 3: MR scanner room setup. **Panel A**: The two flexible control rods extend to the edge of the scanner bore, allowing for rotation and translation of the needle guide while the prostate is located at the scanner isocenter. **Panel B**: The image display and targeting application is projected onto a screen in the scanner room.

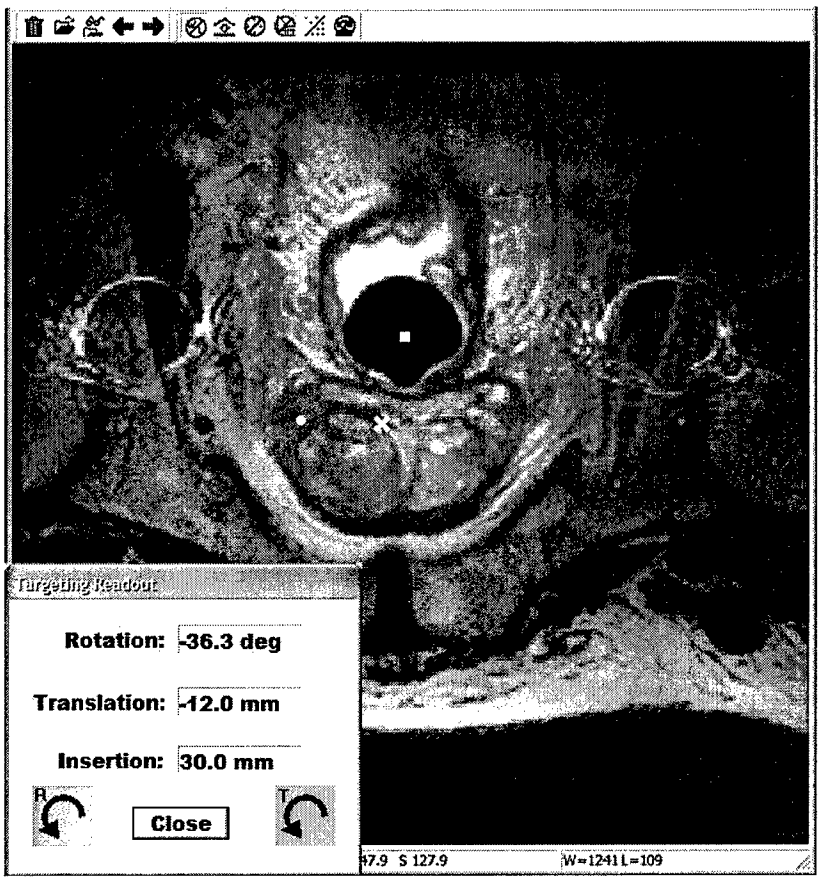

Figure 4: Image display and targeting application. A target (white circle) is graphically selected within a diffuse, low intensity region (suspicious for prostate cancer) in the left posterior lobe of the prostate. The intersection of the image plane and the projected needle path (white cross) as well as the axis of the needle guide (white square) are also shown. As the device is moved, the targeting commands and the projected needle path are updated in realtime.

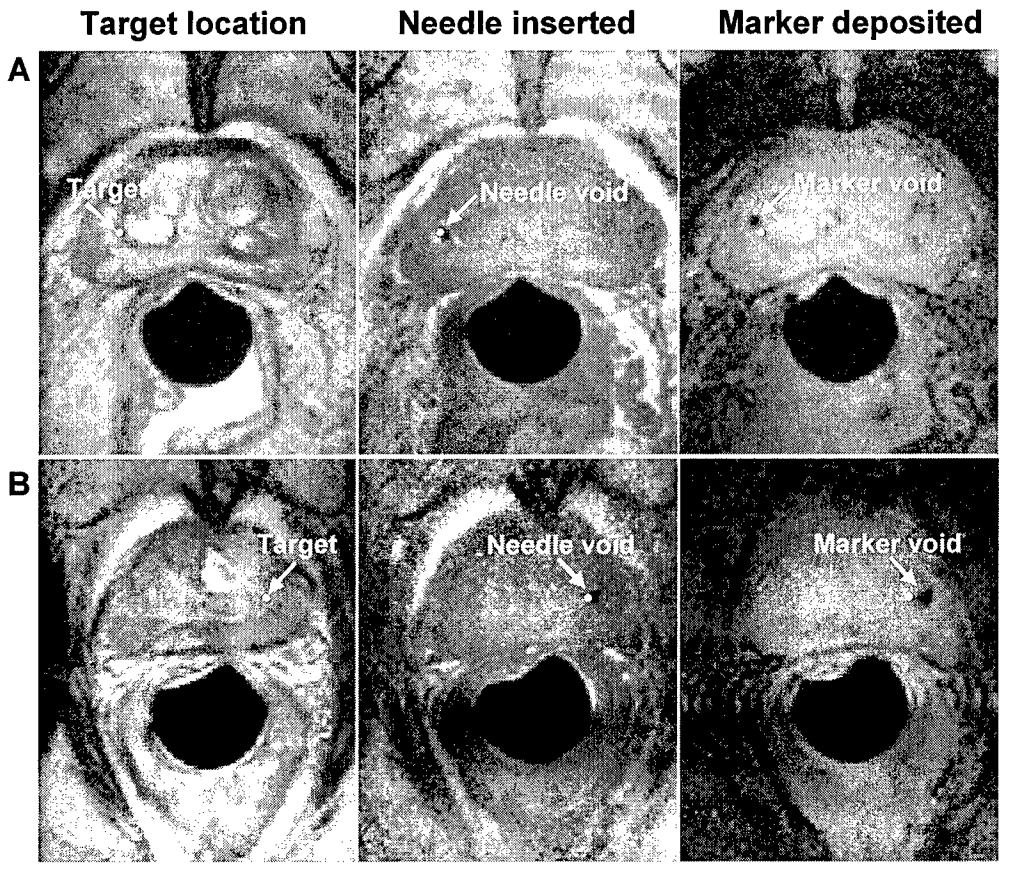

Figure 5: Targeting, needle, and fiducial-marker visualization images. Images from two patients (**Rows A and B,** respectively), show images acquired during the fiducial-marker placement procedure. **Column 1**: Targets are selected on axial, T2-weighted fast spin-echo images. **Column 2**: The needle tip void is visualized in axial, T1-weighted fast spin-echo images. **Column 3**: The marker void is visualized on axial, T2*-weighted gradient-echo images. Note that there is minimal tissue motion throughout each procedure.

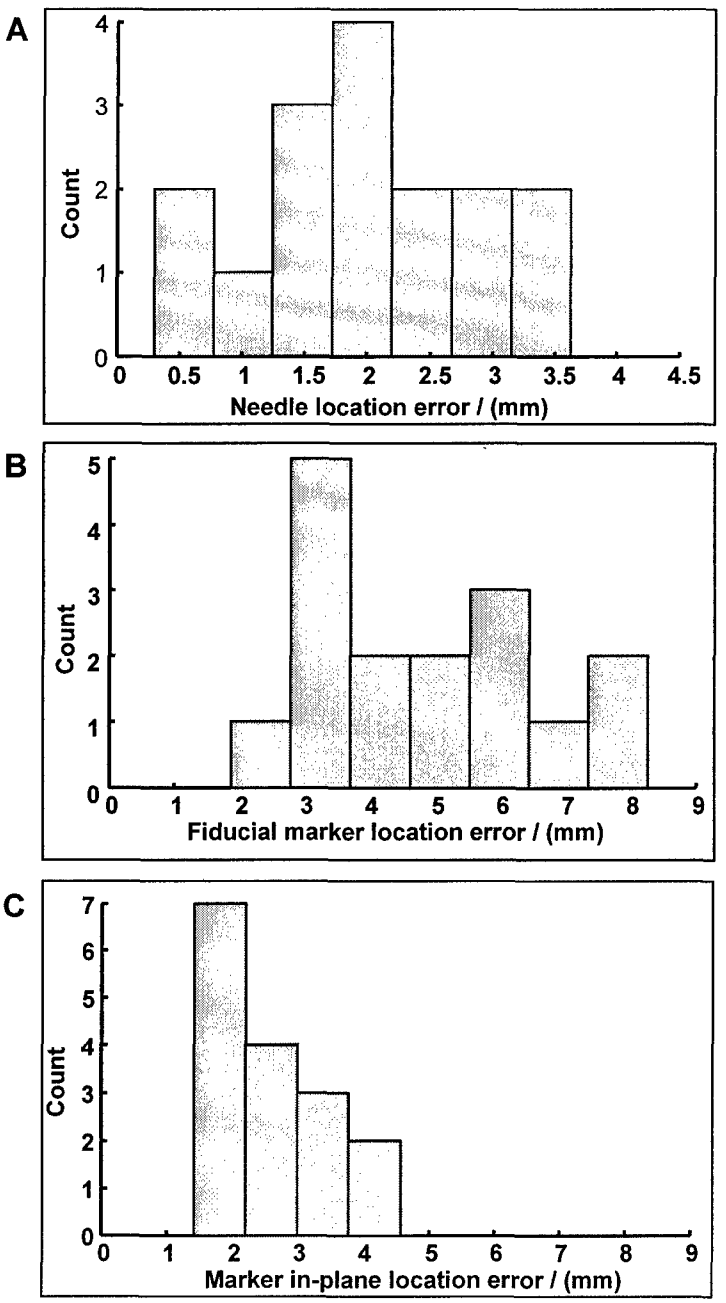

Figure 6: Needle and fiducial-marker placement accuracy. Error histograms show needle tip location errors (**Panel A**), fiducial marker location errors (**Panel B**), and fiducial marker in-plane location errors (**Panel C**) for all 16 gold fiducial markers placed. Mean placement errors for each are 1.9 mm, 4.8 mm, and 2.6 mm, respectively. Because tissue core biopsies are typically 1.5 cm long, the last measure, fiducial marker in-plane placement error, is the best predictor of tissue biopsy acquisition accuracy.

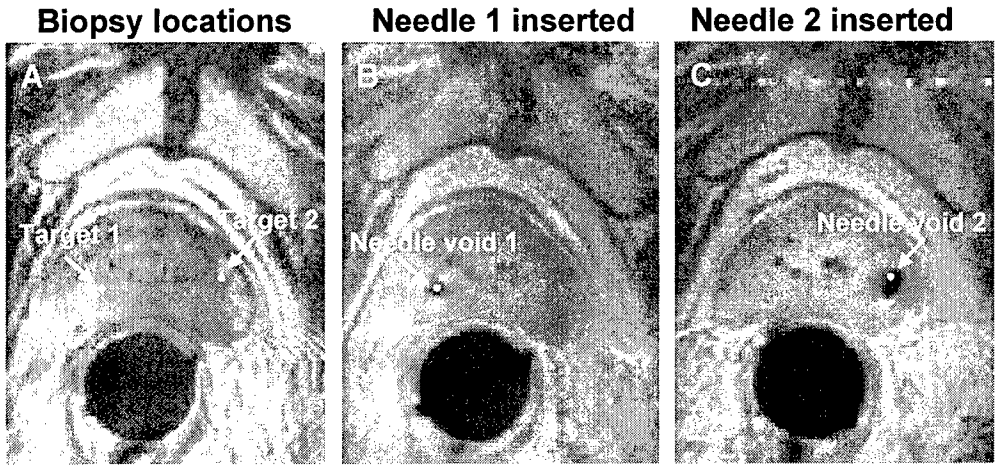

Figure 7: Biopsy target and needle visualization images. Biopsy locations were selected on axial, T2-weighted fast spin-echo images (**Panel A**). The 14-gauge biopsy needle void is visualized in axial, T1-weighted fast spin-echo images (**Panel B & C**).

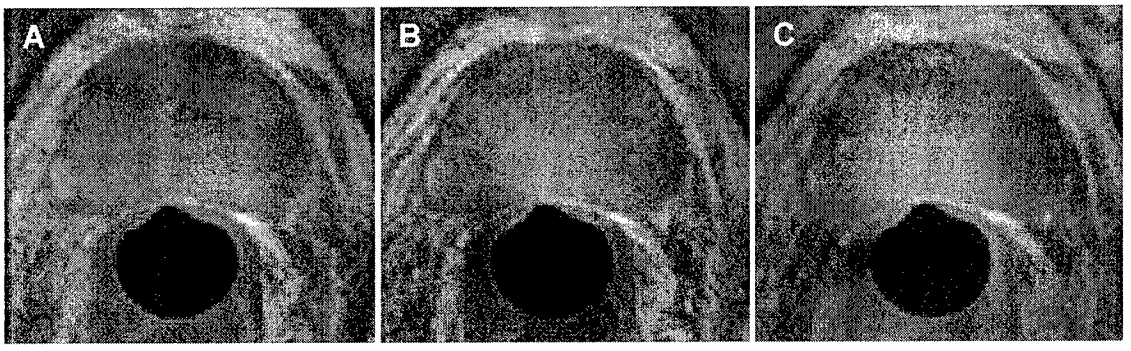

Figure 8: T1-weighted axial fast-spin-echo images of the prostate acquired 20 minutes (**Panel A**), 40 minutes (**Panel B**), and 50 minutes (**Panel C**) after the start of the procedure. Throughout the intervention, including 4 needle placements, the prostate and surrounding tissues remain stable. Importantly, the stationary endorectal sheath prevents movement of the needle guide from causing tissue deformation.

Acknowledgements

Sharon Smith for administrative support; Scott Chesnick for advice on imaging and tracking coil design; Elliot McVeigh and Jeff Duyn for providing scanner resources; Anton Deguet and Anand Viswanathan for providing support software; Karen Ullman for assistance with developing the patient positioning system.